

PREPARING AND MEASURING SINGLE SPINS IN DIAMOND  
AT ROOM TEMPERATURE

David Allen Hopper

A DISSERTATION

in

Physics and Astronomy

Presented to the Faculties of the University of Pennsylvania

in

Partial Fulfillment of the Requirements for the

Degree of Doctor of Philosophy

2019

Supervisor of Dissertation

---

Lee C. Bassett, Assistant Professor of Electrical and Systems Engineering

Graduate Group Chairperson

---

Joshua Klein, Professor of Physics and Astronomy

Dissertation Committee

Jay Kikkawa, Professor of Physics and Astronomy

Nader Engheta, Professor of Electrical and Systems Engineering

A. T. Charlie Johnson, Professor of Physics and Astronomy

Elliot Lipeles, Associate Professor of Physics and Astronomy

PREPARING AND MEASURING SINGLE SPINS IN DIAMOND  
AT ROOM TEMPERATURE

© COPYRIGHT

2019

David Allen Hopper

This work is licensed under the  
Creative Commons Attribution  
NonCommercial-ShareAlike 3.0  
License

To view a copy of this license, visit

<http://creativecommons.org/licenses/by-nc-sa/3.0/>

## ACKNOWLEDGEMENTS

Lee, thank you for everything. You've taught me so much these past few years and have been a great mentor. I remember having conversations about what to expect being the first PhD student in a group, and I have to say that I experienced all of the best things. You created a space with room to grow, learn, build, investigate, and develop. I've learned an immense amount from you in experimental science, communication, writing, and how to always be searching for that next level of complexity, be it in science or my career.

Richard, I wouldn't be where I am without your help. You were always there for a quick question, discussion of an off-the-wall idea, or working through future career plans. You taught me that a good scientist is creative, that matlab can invariably do it, to always bring ear plugs to a metal concert, and to never be afraid to try something new.

Annemarie, I appreciate the time and patience you showed in teaching me early on in my PhD. Most of my optical tricks can be traced back to you, and I try to mimic your outstanding teaching and mentoring techniques in my own work. I admire your ability to tackle any problem and dive into something completely new. I strive to recreate that mindset as I believe it makes for an outstanding scientist.

To all of the quantum engineering laboratory members, it has been a pleasure working with you. I especially want to mention Becca, Sam P., and Raj. The conversations, coffee runs, and collaborations are something that I cherish and will (and already do) look back on fondly. Here's to many more! Yung, you are also included in this list but I wanted to mention on top of this how great it has been to work with you throughout our time at Penn and that I will always remember our Flagstaff trip fondly. I look forward to all of the outstanding success in your future and continuing our friendship.

Joseph, it was a privilege to have worked so closely with you. It was my first experience in a truly interdisciplinary effort and I am grateful for how much you taught me about the

engineering side of life. Your drive and eye for design are something I try to emulate.

To the undergraduate researchers I was lucky enough to mentor, Sam T., Ben, and Sadhana, I want to thank you for the opportunity to have been involved in your careers and I look forward to seeing the things you'll accomplish.

To my Physics PhD cohort, I couldn't have asked for a better group of people to go through this portion of my life. I especially want to mention Shannon, Eric, Paul, Ashley, and Saul for being supportive, caring, and all-around awesome people.

Bijan, Khilesh, and Saul – it was interesting, challenging, but most importantly fun to work with you all on our white-knight quest to improve publishing. I learned so much from you all in those few months that I will take with me the rest of my career. I'm glad to have gotten to know you all better through this.

To Brendan, you've been an unwavering source of support and I can't thank you enough.

To the Davis family, thank you for welcoming me into your family. I'm looking forward to our future adventures.

Becky and Paul, you have been an outstanding pair of people to grow up with. Your support, guidance and love have kept me going when I needed it most. I love you both.

Kim and Jerry, I wouldn't be here without you. I'll always remember your advice that it isn't where you are, but what you are doing. That advice has motivated me to do my best work no matter the surroundings. Mom – I try to channel your capacity to empathize and help people when I'm working with others. Dad – your early advice on mastering the fundamentals has brought me to where I am today. Thank you so much to you both, I love you.

To my fiancée Amy, you are an inspiration to me. As a scientist, a doctor, and most importantly a caring person, I admire your drive, passion, and ability to bring people

together. I wouldn't be here without your support and love. Your propensity to push me out of my bubble has lead to a life I never thought possible. I love you and I couldn't have asked for a better partner to share my life with.

# ABSTRACT

## PREPARING AND MEASURING SINGLE SPINS IN DIAMOND AT ROOM TEMPERATURE

David Allen Hopper

Lee C. Bassett

A functioning qubit must be able to be initialized and measured. The fidelity of these operations is essential for all quantum applications, including quantum sensing, communication, and computation. The diamond nitrogen-vacancy (NV) center is a point defect in the lattice with an optical interface to a coherent ground-state spin, which makes the NV center one of the few spin qubits operable at room temperature. While the NV center spin state can be initialized and read out optically, the fidelity of these operations are far from perfect due to the charge and orbital dynamics. In typical conditions, the NV center is in the proper charge state 75% of the time, and measuring the spin state results in a non-zero signal only 1% of the time. These inefficient mechanisms make many measurements practically intractable. This thesis focuses on improving the preparation and measurement fidelities of NV centers through precise all-optical control of the charge, orbital, and spin dynamics. I first discuss an improved spin readout mechanism which relies on spin-to-charge conversion (SCC) and discuss the potential for single-shot spin readout. Following, I present how charge readout and SCC can be implemented in ensembles of NV centers within nanodiamonds and demonstrate that it provides improvements for spin-relaxometry studies. Finally, I develop a method for initializing a single NV center's charge state with real-time control and show that this capability improves spin readout performance for sensing. To conclude, I discuss how these improved initialization and readout capabilities can be applied to detecting and controlling coupled nuclear spins in the diamond lattice and consider other applications of real-time control.

# TABLE OF CONTENTS

ACKNOWLEDGEMENTS . . . . .	iii
ABSTRACT . . . . .	vi
LIST OF TABLES . . . . .	x
LIST OF ILLUSTRATIONS . . . . .	xii
CHAPTER 1 : Introduction . . . . .	1
1.1 This Thesis . . . . .	3
CHAPTER 2 : The Diamond Nitrogen-Vacancy Center . . . . .	5
2.1 Electronic Structure . . . . .	5
2.2 Charge: Dynamics and Readout . . . . .	9
2.3 Ground State Spin: Properties and Control . . . . .	15
2.4 Charge and Spin Initialization . . . . .	20
2.5 The NV Center as a Qubit . . . . .	21
CHAPTER 3 : Spin Readout: Theory and Implementation . . . . .	23
3.1 Introduction . . . . .	23
3.2 Quantifying Readout Performance . . . . .	23
3.3 Traditional Photoluminescence Spin Readout . . . . .	31
3.4 Spin-to-Charge Conversion . . . . .	36
CHAPTER 4 : Experimental Methods . . . . .	39
4.1 Alignment of NV Centers to Photonic Devices . . . . .	39
4.2 Photolithography on Small Diamond Substrates . . . . .	43
4.3 Multi-Color Imaging and Control of NV Centers . . . . .	45

4.4 Data Acquisition . . . . .	51
CHAPTER 5 : Singlet Based Spin-to-Charge Conversion . . . . .	54
5.1 Introduction . . . . .	54
5.2 Results . . . . .	56
5.3 Discussion . . . . .	62
5.4 Conclusion . . . . .	64
CHAPTER 6 : Spin-to-Charge Conversion in Nanodiamonds . . . . .	65
6.1 Introduction . . . . .	65
6.2 Results . . . . .	68
6.3 Discussion . . . . .	79
6.4 Conclusion . . . . .	81
6.5 Methods . . . . .	82
CHAPTER 7 : Real-Time Charge Initialization . . . . .	84
7.1 Introduction . . . . .	84
7.2 Experimental Setup . . . . .	85
7.3 Results . . . . .	87
7.4 Discussion . . . . .	96
7.5 Conclusion . . . . .	97
CHAPTER 8 : Conclusion and Future Directions . . . . .	98
APPENDICES . . . . .	100
APPENDIX A : Charge Dynamics Calibration . . . . .	101
APPENDIX B : Measuring Spin Properties of a Single NV . . . . .	103
APPENDIX C : Estimating Spin Polarization with Pulsed Excitation . . . . .	105
APPENDIX D : Spin Readout Noise Calculations . . . . .	107

D.1 Photon Summation . . . . . 107

D.2 Thresholding . . . . . 108

APPENDIX E : Steady-State Charge Under Multi-Color Illumination . . . . . 109

APPENDIX F : Population Transfer Matrix Model for Spin-to-Charge Conversion . 113

APPENDIX G : Real-Time Control Hardware . . . . . 117

BIBLIOGRAPHY . . . . . 117

## LIST OF TABLES

TABLE 1 :	Compilation of spin-readout metrics, their formal relation to differential SNR, and common use cases. . . . .	30
TABLE 2 :	Electromagnetic sources used throughout this thesis. . . . .	50
TABLE 3 :	Dichroic beam splitters depicted in Figure 11. . . . .	50
TABLE 4 :	Fit results for the charge dynamics calibration. . . . .	102
TABLE 5 :	Best-fit parameters corresponding to the multi-SCC measurements in Fig. 16(c) of the main text. . . . .	116

## LIST OF ILLUSTRATIONS

FIGURE 1 : NV Center Charge States . . . . .	6
FIGURE 2 : Low Temperature NV <sup>-</sup> Electronic Structure . . . . .	7
FIGURE 3 : NV Center Charge Dynamics . . . . .	10
FIGURE 4 : <sup>14</sup> N Hyperfine Interaction and Single-Gate Errors . . . . .	18
FIGURE 5 : Traditional PL Spin Readout . . . . .	32
FIGURE 6 : Calibrating PL Spin Readout . . . . .	34
FIGURE 7 : Spin-to-Charge Conversion . . . . .	35
FIGURE 8 : SIL Fabrication Process . . . . .	42
FIGURE 9 : Photolithography and Liftoff on Diamond Substrates . . . . .	46
FIGURE 10 : Fabrication of Lithographic Wires on Diamond . . . . .	47
FIGURE 11 : Multi-Color Confocal Microscopy of NV Centers . . . . .	48
FIGURE 12 : Clock Sources for Data Acquisition . . . . .	51
FIGURE 13 : Deterministic Charge State Readout of the NV Center . . . . .	56
FIGURE 14 : Multi-Color Modulation of Steady-State PL and Charge . . . . .	57
FIGURE 15 : Charge Dynamics Driven by Multiphoton Absorption . . . . .	59
FIGURE 16 : Spin-to-Charge Conversion <i>via</i> Singlet Ionization . . . . .	63
FIGURE 17 : Charge and Spin Control of Individual Nanodiamonds . . . . .	66
FIGURE 18 : Optical Charge Dynamics . . . . .	70
FIGURE 19 : High-Contrast Optical Charge Readout . . . . .	72
FIGURE 20 : Spin-to-Charge Conversion in Nanodiamonds . . . . .	75
FIGURE 21 : Performance of the SCC Protocol . . . . .	77
FIGURE 22 : Real-Time Charge Initialization . . . . .	86
FIGURE 23 : Modeling Real-Time Control . . . . .	88

FIGURE 24 : Charge Initialization Fidelity and Spin Readout . . . . .	93
FIGURE 25 : Readout Improvements Through Real-Time Initialization . . . . .	94
FIGURE 26 : Charge Dynamics Calibration . . . . .	102
FIGURE 27 : Measurements of Spin Properties . . . . .	104
FIGURE 28 : Lifetime Measurement of Spin Polarization . . . . .	106
FIGURE 29 : Phenomenological Two-Level Model . . . . .	110
FIGURE 30 : Results of the Phenomenological Model Fit . . . . .	111
FIGURE 31 : Population Transfer Matrix Model for Singlet-SCC . . . . .	114

## CHAPTER 1 : Introduction

Recent, rapid advances in creating, detecting, and controlling quantum-mechanical states in engineered systems heralds the beginning of the quantum-information era. A diverse set of physical platforms, including superconducting circuits [58], cold ions [24], integrated photonics [151], and spins in semiconductors [10] have enabled progress toward fault-tolerant quantum computation, quantum-secure communication systems, and unparalleled sensing technologies. Nevertheless, most platforms remain in the early engineering stages and face substantial technical challenges that are intricately tied to the underlying physics of the qubit.

Of all of the current quantum information processing platforms, point defects in semiconductors arguably have the longest history in human civilization. Gemstones are the most well-known example of this class of material in daily life. Most of the different colors of gemstones are due to trace impurities within the crystal. For example, rubies and sapphires both come from the corundum mineral with different, small additions of chromium, iron, titanium, copper, or magnesium; aquamarines and emeralds come from the the beryl mineral with varying trace amounts of iron, chromium, and vanadium. Similarly, diamonds have long been known to come in different colors such as yellow, blue, pink, green, grey, red and many other shades. These colors are the result of many different elements polluting the diamond crystal. In fact, there are hundreds of distinct impurities, commonly referred to as “color centers”, that give rise to different colors of diamond [176].

Diamonds in particular have captured human interest for millennia and have long been associated with the power of nature. In the ancient Indian Sanskrit text *Rigveda*, dated to 1500-1200 B.C., the god Indra is said to have wielded a thunderbolt-like scepter containing a diamond at its focal point, which could focus immense amounts of energy [102]. In fact, the Sanskrit word for diamond, *vajra*, is the same that describes Indra’s thunderbolt [140]. Throughout the ages, diamonds have continued to not only symbolize power, but

also wealth, status, and more recently romance. Certain large and colorful diamonds, such as the Hope Diamond and Sancy diamond, have their histories traced back centuries and are now symbols for modern day nationalism, class rivalry, and colonialism [102, 140].

This enduring cultural interest likely played a role in the scientific study of diamond as a material in the twentieth century. Diamond is currently recognized in the scientific and engineering community primarily for its mechanical [52], electronic [175], and optical properties [176]. These discoveries and advancements are largely due to the technological development of laboratory-grown diamonds via the high-pressure high-temperature synthesis method by Bundy et al. [26] at General Electric in 1955, followed by the invention of chemical-vapor-deposition synthesis of diamond by the National Institute for Research in Inorganic Materials in Japan by Kamo et al. [93], which allowed for the preparation of ultra-high purity diamond. It appears as though early human's perceptions of the power of diamond were well warranted; diamond is one of the hardest known materials, offers some of the best thermal conductivity, and exhibits one of the largest optical transparency windows.

Modern research on the optical properties of diamond has focused on understanding the microscopic origin of the various colors of diamond. As of the year 2000, there were a reported 650 unique vibronic and electronic optical centers in diamond contributing to the various observed macroscopic colors, with more being reported annually [176]. These optical centers are analogous to molecules trapped within the diamond crystal, absorbing visible light and fluorescing in characteristic wavelength ranges. Many of these optical centers consist of a dopant atom in the diamond lattice which takes the place of a carbon atom, referred to as a substitutional defect. Nitrogen is the most common dopant in diamond and produces yellow and brown colors. In addition to a substitutional defect, nitrogen can exist next to other missing carbon atoms in the lattice, forming vacancy complexes. The most widely studied of these is the negatively charged nitrogen-vacancy (NV) center, consisting of a substitutional nitrogen atom situated directly next to a carbon vacancy.

Initially postulated to exist in 1965 [48], the NV center has been intensely studied for over five decades, with an explosion of interest in the past two decades [44].

The recent surge of research into the NV center stems from the fact that this particular defect has a quantum-mechanical spin state that can be initialized, controlled, and measured all at room temperature [64, 89]. A truly versatile platform, the NV center has been utilized for designing quantum memories [49, 116, 133]; addressing individual nuclear spins [30, 107, 124]; engineering nanoscale sensors of magnetism [27], proteins [111] and chemicals [7]; exploring hybrid quantum mechanical systems [5]; and testing the fundamental principles of quantum mechanics through loophole-free violations of Bell’s inequality [77]. While most quantum systems require some form of an extreme lab-created environment – such as low temperatures, ultra-high vacuum, or both – to manifest, diamond naturally provides this environment for its point defects. The purported mythical power of diamonds has in another sense been physically realized; diamond is one of the few materials that allows us to study and harness quantum physics in ordinary conditions.

### 1.1. This Thesis

A common challenge, and critical criterion for scalable quantum information processing, is reliably preparing and measuring a quantum state [41]. The fortuitous electronic structure of the diamond NV center results in “built-in” mechanisms for satisfying these criteria [44]. However, as more sophisticated experiments and applications were developed using the NV center, the shortcomings of these preparation and readout protocols began to surface as they limited the sensing precision and prevented particular experiments. These problems were solvable using quantum optical techniques at cryogenic temperatures [16, 138] and they are enabling the construction of a quantum-capable communication network [83, 174]. At room temperature, where sensing applications are the focus, there have been strategies for overcoming the errors associated with readout [91, 125, 150] and initialization [46, 172].

Nonetheless, previous strategies for improving readout and initialization have been in-

compatible with sensing schemes or require stringent experimental requirements. In the case of readout, techniques that require quantum logic require magnetic fields in excess of 10 mT with  $< 1^\circ$  alignment accuracy and simultaneous microwave and radio-frequency control [67, 125]. This technical requirement constrains the operating magnetic-field regime and imposes challenging system engineering considerations. Prior to this work, there were no known methods for deterministic initialization into the desired negative charge state that did not detrimentally affect the spin-coherence time. Overcoming these issues with regards to preparation and measurement while maintaining sensitivity would allow for improved experimental throughput and the ability to resolve higher frequency environmental dynamics.

This thesis is centered on developing sensing-compatible protocols for improving the preparation and measurement fidelity of NV centers at room temperature. The remaining chapters are outlined as follows: Chapter 2 discusses the theoretical and experimental understanding of the diamond NV center; Chapter 3 presents quantitative tools for characterizing spin readout and discusses two types of readout techniques; Chapter 4 presents experimental methods that were developed during the course of this thesis; Chapter 5 overviews how near-infrared excitation can improve the initial charge-state fidelity and enable spin-to-charge conversion through the singlet manifold; Chapter 6 discusses the adaptation of spin-to-charge conversion to ensembles of NV centers within nanodiamonds; Chapter 7 covers a method for the deterministic initialization of the NV center's charge state through real-time feedback and discusses the impact for sensing performance; and Chapter 8 concludes this thesis and discusses future directions.

## CHAPTER 2 : The Diamond Nitrogen-Vacancy Center

The diamond NV center is one of the most widely studied defects in diamond due to its visible photoluminescence and controllable spin state [44]. Critical to these properties are the defect’s electronic structure, charge dynamics, and spin properties. This chapter covers the most relevant physical concepts of the NV center central to this thesis; for a more detailed treatment I direct the reader to the review by Doherty et al. [44]. This Chapter is structured as follows: Section 2.1 describes the electronic structure of the diamond NV center; Section 2.2 discusses the charge structure, dynamics, and readout mechanism; Section 2.3 overviews the spin properties and control protocols; Section 2.4 discusses the charge and spin initialization mechanisms and limiting factors; and Section 2.5 summarizes the NV center’s use as a qubit.

### 2.1. Electronic Structure

The NV center is physically analogous to a molecule in free space with lowered symmetry. Accordingly, a NV center can be theoretically modeled by accounting for the dangling bonds present at the defect either in the single-particle picture or multi-particle picture. The following discussion draws largely from the works of Doherty et al. [43] and Maze et al. [117], which were attempts to theoretically derive the  $NV^-$  electronic structure starting from symmetry considerations. This section will detail the theoretical understanding of NV centers in diamond and highlight when it is illuminating to use one model over the other.

The NV center is a point defect of the  $C_{3v}$  symmetry group, with a symmetry axis pointing along the [111] crystallographic axis. The symmetry axis connects the substitutional nitrogen and adjacent vacancy [31, 37, 48]. This results in four dangling  $sp^3$  orbitals localized at the defect: three due to the carbon atoms surrounding the vacancy and one due to the substitutional nitrogen. Group theory allows for the previous orbitals to be combined into 4 symmetry-adapted bases comprised of  $a'_1, a_1, e_x, e_y$  [43, 117]. These bases are written in ascending energy, and the two  $e$  orbitals are degenerate. The set of single-

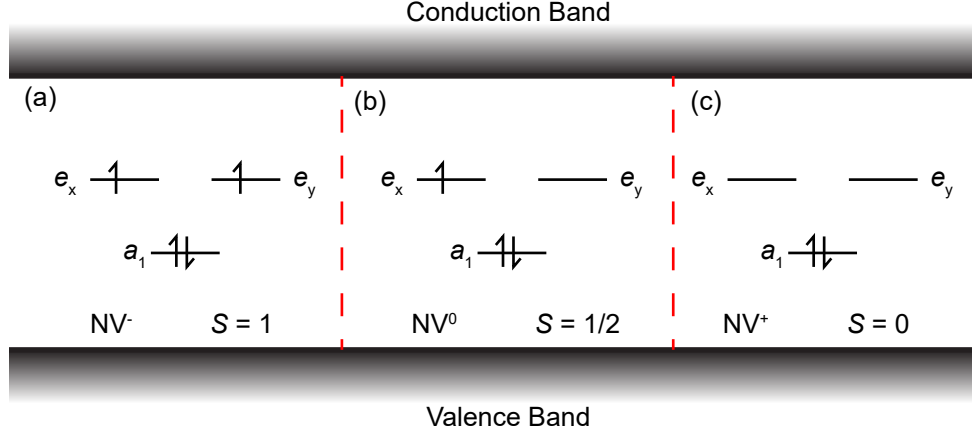


Figure 1: NV Center Charge States. Allowed defect levels and their electron occupation for  $NV^-$  (a),  $NV^0$  (b), and  $NV^+$  (c). Note: for all three charge states there is a filled  $a'_1$  level residing within the valence band which is not shown.

particle orbitals provide a useful tool for visualizing and analyzing the electronic structure of different defect charge states. The ground state electronic configuration of the orbitals for the three most commonly discussed charge states – the negative ( $NV^-$ ), neutral ( $NV^0$ ), and positive ( $NV^+$ ) – of the NV center are presented in Fig. 1. In contrast to traditional semiconductors, the concept of a Fermi level in diamond is undefined and multiple charge states can exist in the same bulk diamond [88].

I will discuss the electronic structure of the negative charge state due to its importance in quantum information processing applications. Similar procedures outlined here have also been applied to the neutral charge state [57], while there is limited work other than indirect photoluminescence [94] and nuclear magnetic resonance [133] measurements of the positive charge state. The NV center’s chemical structure was confirmed through the spin and optical band signatures associated with  $NV^-$  ( $S = 1$ ) [108, 109]. The  $NV^-$  charge state consists of 6 electrons filling the single-particle orbitals with a ground state of  $a_1'^2 a_1^2 e^2$ , while the first excited state is given by  $a_1'^1 a_1 e^3$  [Fig. 1(a)]. Additional excited states are not expected to contribute to the defect’s behavior under typical conditions [43]. A transformation from the single-particle to multi-particle picture elucidates the allowed energy states and transitions between them. This is performed by finding the configuration states of the ground and first

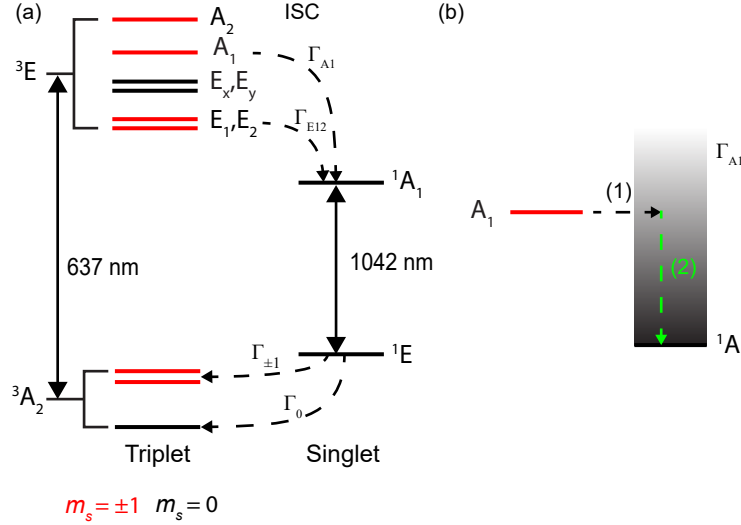


Figure 2: Low Temperature  $NV^-$  Electronic Structure. (a) The relevant electronic states for the triplet and singlet spin manifolds along with their zero phonon lines (solid double arrow) and non-radiative decay channels that arise from the inter-system crossing (ISC). Red horizontal lines signify  $|m_s| = 1$ , whereas black lines signify  $m_s = 0$ . (b) Detailed look at the  $\Gamma_{A_1}$  upper ISC rate and the two stages. The first stage consists of an energy-conserving spin-orbit and electron-phonon interaction, the second stage is a phonon-phonon vibrational relaxation. The shaded region signifies the phonon sideband of the singlet manifold.

excited orbital configurations that transform as the irreducible representations of the  $C_{3v}$  group and are represented by  ${}^3A_2$ ,  ${}^1E$ ,  ${}^1A_1$ ,  ${}^3E$ , and  ${}^1E'$ . These configuration states are broken down into two spin manifolds, where the superscript of 3 signifies states that have triplet spin character ( $S = 1$ ) and a superscript of 1 signifies states that have singlet spin character ( $S = 0$ ).

The energetic ordering of the configuration states has been a topic of discussion since the discovery of the NV center, however it has largely been agreed upon in recent years [44] and is shown in Figure 2(a). The triplet manifold consists of the ground state  ${}^3A_2$  and excited state  ${}^3E$ , which are optically coupled and separated by the  $NV^-$  zero phonon line (ZPL) of 1.945 eV (637 nm). The fine structure of the ground and excited states is included. For the ground state, the  $|m_s| = 0, 1$  spin projections are split by 2.87 GHz due to spin-spin interactions. The excited state is more complicated, due to the fact that there are contributions to the level ordering from fixed values, such as spin-spin interaction and spin-

orbit coupling, as well as inhomogeneous quantities, such as strain, electric, and magnetic fields [14, 43, 117]. The  ${}^3E$  fine structure is only resolvable for  $\text{NV}^-$  within pristine diamond and at temperatures  $< 20\text{ K}$  [14, 159]. The singlet manifold has a metastable ground state of  ${}^1E$  and an excited state of  ${}^1A$ , which are optically coupled by a ZPL of 1.19 eV (1042 nm). The  ${}^1E$  and  ${}^1E'$  states undergo Coulomb repulsion, where  ${}^1E$  is lowered and  ${}^1E'$  is increased in energy. This is partly the reason for the  ${}^1E$  ground state in the singlet manifold. To date, the  ${}^1E'$  state has not been directly observed in experiments and can be excluded from the model of the electronic structure for all intents and purposes.

A critical feature of  $\text{NV}^-$  is the inter-system crossing (ISC) between the triplet and singlet manifolds, which allows for spin initialization and readout. There are two ISCs, the upper ISC ( ${}^3E$  to  ${}^1A_1$ ) and lower ISC ( ${}^1E$  to  ${}^3A_2$ ). Both the upper [60, 61] and lower ISC branches [92, 165] have recently been theoretically and experimentally investigated in the low temperature limit. Both ISC mechanisms are similar in nature and are comprised of two stages [60, 114, 165]; I will briefly discuss the details of the upper branch, which is also presented in Figure 2(b). The first stage is an energy-conserving transition between a subset of  ${}^3E$  ( ${}^3E_{1,2}$  and  $A_1$ ) states and an excited vibrational mode of the singlet excited state  ${}^1A_1$ . This stage requires both a spin and orbital change and is possible through a spin-orbit and electron-phonon interaction [60]. The second stage is energy non-conserving and is mediated by a phonon-phonon interaction. The ISC rate is dominated by the first electronic stage since the vibrational relaxation occurs within picoseconds [84]. The orbital averaged rate for the  $|m_s| = 1$  states is  $\Gamma_{\text{ISC}} = 2\pi \times 8\text{ MHz}$  [60]. For comparison, the optical decay rate is  $2\pi \times 13\text{ MHz}$ .

At room temperature, the orbital averaging of the  ${}^3E$  manifold must be taken into account. This process, mediated by phonon-phonon interactions averages the spin states together resulting in an orbital singlet [139]. The ISC rate is thus an average over all of the  $|m_s| = 1$  states [60]. There is some discrepancy in the literature in regards to the  $m_s = 0$  state. The theoretical considerations laid out in the prior paragraph identified

no known coupling between the excited triplet  $m_s = 0$  states and the singlet manifold. Furthermore, orbital averaging is expected to only average similar spin states together, and low temperature measurements resolving the  ${}^3E$  fine structure place a small upper bound on the coupling between the  ${}^3E$ ,  $m_s = 0$  states to the singlet  ${}^1A_1$ . Nonetheless, many experimentally-motivated models of the  $NV^-$  electronic structure invoke an upper ISC rate for  $m_s = 0$  which is within an order of magnitude of the  $|m_s| = 1$  rate to satisfactorily fit their observations [15, 44, 66, 126, 137]. While this discrepancy remains unresolved, in later chapters I will default to the commonly utilized model incorporating an upper ISC rate for  $m_s = 0$ . The room temperature electronic structure and dynamics will be explained in more detail when discussing the photoluminescence spin readout mechanism in Chapter 3.

## 2.2. Charge: Dynamics and Readout

The two most commonly observed NV center charge states are the visibly fluorescent  $NV^-$  and  $NV^0$ . Signatures of  $NV^+$  have been observed indirectly through nuclear magnetic resonance [133] and electrochemical gating [94]; however, I will focus on the two optically active charge states. This section will cover the optically-induced charge dynamics of the NV center, overview a model of photon histograms undergoing charge transitions, and discuss how the charge state can be measured to very high precision.

### 2.2.1. Charge Dynamics

The NV center's optical charge dynamics can be modeled by a two state system with each state emitting photons at a different rate [Fig. 3(a)]. Both  $NV^-$  and  $NV^0$  charge states are observed during optical illumination with a wavelength of 532 nm in type Ib diamond [55, 113]. However, in higher-purity type IIa diamond there are no definitive reports of  $NV^0$  fluorescence, yet there are observations of a long-lived dark state [71]. This was remedied by the observation that the long-lived dark state was consistent with an electronic spin  $S = 1/2$ , which was attributed to the  $NV^0$  charge state [172]. In single NV studies, the  $NV^0$  emission rate is considered to be at the background level of the measurement apparatus.

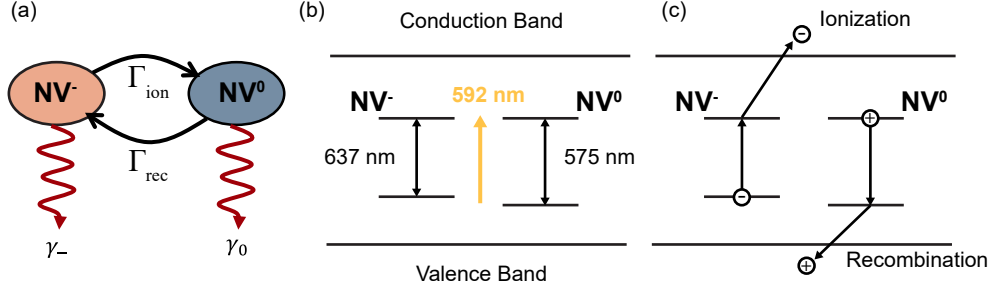


Figure 3: NV Center Charge Dynamics. (a) Model describing the optically induced charge dynamics. (b) Location of charge state ZPLs within the band gap. The 592 nm line is representative of a commonly chosen charge-selective excitation wavelength. (c) Electron and hole picture for ionization and recombination. Solid lines with an arrow represent the absorption of a photon.

The emission rates of the two charge states increase linearly at low power, but the emission from  $NV^-$  saturates due to the optical dynamics. The  $NV^-$  emission rate is given by

$$\gamma_- = C_{\text{sat}} \times \frac{P}{1 + \frac{P}{P_{\text{sat}}}} + D, \quad (2.1)$$

where  $P$  is the optical power,  $C_{\text{sat}}$  is the saturation fluorescence rate (measured at the detector which includes the collection efficiency of the measurement apparatus),  $P_{\text{sat}}$  is the empirically determined saturation power, and  $D$  is the detector-limited dark counts. The  $NV^0$  emission rate is given by

$$\gamma_0 = C_0 \times P + D, \quad (2.2)$$

where  $C_0$  is the power-scaling rate of the background fluorescence.

There are two rates to consider in the charge conversion process [Fig. 3]: the ionization rate ( $\Gamma_{\text{Ion}}$ ) and the recombination rate ( $\Gamma_{\text{Rec}}$ ).  $\Gamma_{\text{Ion}}$  quantifies the rate at which an electron is ejected from  $NV^-$ , leaving the defect in  $NV^0$ .  $\Gamma_{\text{Rec}}$  quantifies the rate at which a hole is ejected from  $NV^0$ , leaving the defect in  $NV^-$ . The rates depend on the wavelength and power of the illumination [8, 172]. The physical mechanism for the two processes was proposed by Siyushev et al. [152] and is shown in Figure 3(c). Ionization consists of a single photon absorption promoting  $NV^-$  to the excited state, followed by the subsequent

absorption of a second photon promoting an electron to the conduction band. Density functional theory calculations predict that the radiative recombination lifetime ( $\sim 0.5 \mu\text{s}$ ) is much longer than the Auger recombination timescale ( $\sim 800 \text{ps}$ ), which allows for the conduction band electron to escape the defect. Recombination consists of a single photon absorption promoting  $\text{NV}^0$  to the excited state, followed by another photon absorption which excites one of the deep-lying  $a'_1$  electrons to fill the now empty  $a_1$  level. The hole in the valence band then undergoes a similar Auger process and an additional electron from the valence band re-populates the  $a'_1$  state.

The charge dynamics depend both on optical wavelength and power [8, 172]. The wavelength dependence arises from the substantial difference between the charge state ZPLs of  $\sim 210 \text{meV}$ . This means that an ionization rate and  $\text{NV}^-$  photoluminescence will only be present for wavelengths  $< 637 \text{nm}$  and a recombination rate will only be present for wavelengths  $< 575 \text{nm}$  [Fig. 2.2(b)]. At higher optical energies ( $2.4 \text{eV}$ ,  $475 \text{nm}$ ) an electron from the ground state of  $\text{NV}^-$  can be promoted directly to the conduction band, and the center largely remains in  $\text{NV}^0$  [8]. The trap-assisted nature of these processes, where the trap is the excited state of either charge state, leads to a power saturating effect. An empirical model for the ionization and recombination rates is given by [152, 172]

$$\Gamma_{\text{Ion/Rec}} = A_{\text{Ion/Rec}} \frac{I^2}{1 + \frac{\beta I}{P_{\text{sat}}}}, \quad (2.3)$$

where  $A_{\text{Ion/Rec}}$  is the effective cross-section for the ionization/recombination process, and  $P_{\text{sat}}$  is the saturating power, related to the fluorescence saturation power. Thus, low intensities relative to the optical decay rate result in quadratically scaling dynamics, while high intensities result in a linear scaling of the dynamics. The measured charge dynamics rates for a single NV center are included in Appendix A.

The ionization and recombination rates determine the steady state charge population

under optical pumping. The  $NV^-$  population is given by

$$P_- = \frac{\Gamma_{\text{Rec}}}{\Gamma_{\text{Rec}} + \Gamma_{\text{Ion}}}. \quad (2.4)$$

Thus, for wavelengths that only excite  $NV^-$ ,  $\Gamma_{\text{Rec}} \sim 0$  and  $P_- \approx 0$ . However, the most common pumping wavelength for NV center experiments (532 nm) excites both charge states. It was initially found that  $P_- = 75\%$  for 532 nm illumination [171, 172]. Aslam et al. [8] studied the dependence of  $P_-$  on excitation wavelength and found that  $P_- \leq 75\%$  for all visible wavelengths. Almost all NV experiments ignore this initial state infidelity and overcome the associated noise by increasing the number of repetitions.

### *2.2.2. Photon Number Probability Distribution Model*

In the absence (or negligible contribution) of ionization and recombination, the observed photon number probability distribution would be explained by two weighted Poisson distributions with means equal to the rates in Equations 2.1 and 2.2 multiplied by the observation time. However, the ionization and recombination rates for typical experimental settings are non-negligible [8] and must be taken into account when attempting to model the observed photon number probability distribution. The influence of ionization and recombination can be intuitively thought as modifying the Poisson distribution due to the charge state with a time-varying mean during the observation. Shields et al. [150] presented an analytical solution to this problem which agrees with experimental observations over a wide range of physical conditions and has been confirmed independently [35, 68].

The photon probability distribution model includes all four charge dynamics rates in addition to the readout time and the initial  $NV^-$  population. Given the NV is initially in  $NV^-$ , the photon probability distribution depends on whether there were an odd or even

number of charge transitions, and is given by [150]

$$p(n|-, \text{odd}) = \int_0^{t_R} d\tau e^{(\Gamma_{\text{Rec}} - \Gamma_{\text{Ion}})\tau - \Gamma_{\text{Rec}}t_R} \times \Gamma_{\text{Ion}} \times \text{BesselI}\left(0, 2\sqrt{\Gamma_{\text{Ion}}\Gamma_{\text{Rec}}\tau(t_R - \tau)}\right) \times \text{PoissPDF}(\gamma_- \tau + \gamma_0(t_R - \tau), n) \quad (2.5)$$

$$p(n|-, \text{even}) = \int_0^{t_R} d\tau e^{(\Gamma_{\text{Rec}} - \Gamma_{\text{Ion}})\tau - \Gamma_{\text{Rec}}t_R} \times \sqrt{\frac{\Gamma_{\text{Ion}}\Gamma_{\text{Rec}}\tau}{t_R - \tau}} \times \text{BesselI}\left(1, 2\sqrt{\Gamma_{\text{Ion}}\Gamma_{\text{Rec}}\tau(t_R - \tau)}\right) \times \text{PoissPDF}(\gamma_- \tau + \gamma_0(t_R - \tau), n) + e^{-\Gamma_{\text{Ion}}t_R} \text{PoissPDF}(\gamma_- t_R, n), \quad (2.6)$$

where  $\gamma_-$  ( $\gamma_0$ ) is the photon detection rate due to  $\text{NV}^-$  ( $\text{NV}^0$ ),  $\Gamma_{\text{Ion}}$  ( $\Gamma_{\text{Rec}}$ ) is the ionization (recombination) rate,  $t_R$  is the total readout duration, and BesselI is a modified Bessel function of the first kind. The full photon distribution given starting in  $\text{NV}^-$  is

$$p(n|-) = \frac{1}{2}(p(n|-, \text{odd}) + p(n|-, \text{even})). \quad (2.7)$$

To get the equivalent expression for  $\text{NV}^0$ , simply swap the ionization and recombination rates as well as the photon rates ( $\Gamma_{\text{Ion}} \leftrightarrow \Gamma_{\text{Rec}}$  and  $\gamma_- \leftrightarrow \gamma_0$ ) in Eqs. 2.5 and 2.6. A general mixture of the two charge states is given by

$$p(n) = P_- p(n|-) + (1 - P_-) p(n|0), \quad (2.8)$$

where  $P_-$  is the initial population of  $\text{NV}^-$  prior to the start of readout.

The photon probability distribution model is useful for calibrating the charge dynamics as well as allowing for accurate determination of the initial  $\text{NV}^-$  population prior to the measurement by fitting observed photon detecton histograms to Eq. 2.8.

### 2.2.3. High Fidelity Charge Readout

Through an appropriate choice of excitation wavelength, power, and readout duration, the charge state of a single NV center can be determined by a single measurement with high fidelity [172]. High fidelity charge readout of NV centers is possible when the following criteria are met:

1. Optimal excitation wavelength,  $575 \text{ nm} < \lambda < 637 \text{ nm}$
2. Large signal-to-background,  $\gamma_- \gg \gamma_0$
3. Minimized ionization during readout,  $\Gamma_{\text{Ion}} t_R \ll 1$

A common wavelength used is 592 nm [Fig. 2.2(b)] due to the availability of off-the-shelf lasers. The other criteria concerning the power and readout duration are empirically determined. A simple method for bootstrapping the ideal power and readout duration for charge readout is to look for signatures of blinking in the observed fluorescence at low powers with a variable bin size [8, 172].

Critical to high fidelity charge readout is the state-assignment step, in which the number of photons observed is mapped to a binary  $\text{NV}^-$  or  $\text{NV}^0$  classification. For most cases, the simplest classification scheme is to compare the number of detected photons ( $n$ ) to a previously selected photon threshold ( $\nu$ ), formally given by

$$\text{Charge} = \begin{cases} \text{NV}^-, & \nu \geq n \\ \text{NV}^0, & \nu < n. \end{cases} \quad (2.9)$$

There are two sources of error in this classification:  $\text{NV}^0$  emission leading to false positives and  $\text{NV}^-$  emission leading to false negatives. This assumes that there is only a single NV center in the collected confocal volume. The photon probability distribution outlined in the previous section can be used to quantify these errors, while accounting for ionization and

recombination. The errors are

$$\epsilon_0 = \sum_{i=\nu}^{\infty} p(i|0), \quad (2.10)$$

and

$$\epsilon_- = \sum_{i=0}^{\nu-1} p(i|-). \quad (2.11)$$

The charge readout fidelity is then given by [35]

$$\mathcal{F}_C = 1 - \frac{1}{2}(\epsilon_0 + \epsilon_-), \quad (2.12)$$

and takes on values from 50% (random state assignment) to 100% (perfect state assignment). The optimal threshold  $\nu$  is found by maximizing  $\mathcal{F}_C$  from a calibration. It should be noted that this state assignment is *prior* to measurement. The charge readout process is destructive and leaves the NV center in a charge mixture, however, this effect can be minimized by using a low power and long readout duration [68].

Charge readout techniques have also been extended to ensembles of NV centers in bulk diamond [40, 88] and nanodiamonds [79, 94]. The procedure relies on the same criteria outlined above, however, due to the ensemble of NV centers a state assignment cannot be made and the raw photon signal is the quantity utilized.

### 2.3. Ground State Spin: Properties and Control

One of the most important aspects of the negatively-charged NV center is the coherent ground state spin. In this section, I will discuss the Hamiltonian governing the  $\text{NV}^-$  spin state, how spin control is implemented, and finally discuss spin dynamics.

#### 2.3.1. Ground State Spin Hamiltonian

Due to the broken inversion symmetry of  $C_{3v}$ , there is a zero-field energy splitting between the ground state's  $m_s = 0$  and  $m_s = \pm 1$  electronic spin sublevels of  $D_{gs} = 2.87$  GHz [64]. In addition, the intrinsic Hamiltonian of  $\text{NV}^-$  must include contributions from the the nuclear

spin of the host nitrogen atom. The two most common isotopes, in decreasing abundance, are  $^{14}\text{N}$  ( $S = 1$ ) and  $^{15}\text{N}$  ( $S = 1/2$ ). Combining the electronic and nuclear spins leads to a ground state spin Hamiltonian (in units of frequency) of [42]

$$\hat{H}_{gs} = D_{gs}S_z^2 + A_{\parallel}S_zI_z + A_{\perp}(S_xI_x + S_yI_y) + PI_z^2, \quad (2.13)$$

where  $S_i$  are the Pauli spin operators for the electron spin,  $I_i$  are the Pauli spin operators for the nuclear spin,  $A_{\perp}, A_{\parallel}$  are the perpendicular and parallel hyperfine components, respectively, and  $P$  is the quadrupolar splitting of the nuclear spin (non-zero for  $^{14}\text{N}$ ). The hyperfine components are typically on the order of  $\sim 2$  MHz, or 3 orders of magnitude less than the electronic splitting and are thus treated as a perturbation.

There are other perturbations to the Hamiltonian, namely due to DC magnetic and electric fields, strain fields, and other strongly coupled spins in the diamond such as other NV centers [55],  $^{13}\text{C}$  nuclei [30], and substitutional nitrogen [72]. In this thesis, many of the experiments utilize a DC magnetic field to break the degeneracy of the  $m_s = \pm 1$  states through the Zeeman effect. The Zeeman Hamiltonian is given by

$$\hat{H}_z = \vec{\mu} \cdot \vec{B}, \quad (2.14)$$

where  $\vec{\mu}$  is the magnetic moment of the  $\text{NV}^-$  ground-state spin and  $\vec{B}$  is the external magnetic field. The magnetic moment is given by

$$\vec{\mu} = \frac{\mu_B g}{\hbar} \vec{S}, \quad (2.15)$$

where  $\mu_B$  is the Bohr magneton,  $g$  is the Landé g-factor, and  $\vec{S}$  are the spin-1 Pauli matrices. When the magnetic field is aligned along the NV's quantization axis, the “good” electronic spin eigenstates are  $|0\rangle, |-1\rangle, |+1\rangle$ . The frequency difference as a function of field strength between the non-zero spin projection states is given by  $5.6 \text{ MHz G}^{-1}$ . A field of 20-100 G is typically used in this thesis to isolate the two spin-levels.

### 2.3.2. Spin control

The first demonstration of coherent control of the  $\text{NV}^-$  ground-state spin by Jelezko et al. [89] precipitated the surge of interest in this particular defect. The zero-field splitting magnitude and gyromagnetic ratio helped accelerate the pace and scale of research due to the ease of acquiring off-the-shelf microwave and radio frequency components capable of sourcing the necessary electromagnetic fields. An  $\text{NV}^-$  electron spin interacting with a classical oscillating magnetic field is well described theoretically by the semi-classical Rabi problem. To simplify the discussion and align with experiments, I restrict the analysis to a sub-space of the total  $S = 1$  Hilbert space ( $m_s = 0, -1$ ). This reduces the problem to a two-level system, where the energies are governed by the static Hamiltonian and DC magnetic field and is given by

$$\hat{H}_o = \omega_0 S_z, \quad (2.16)$$

where  $\omega_0$  is the frequency difference between the two spin states. The full control Hamiltonian is given by

$$\hat{H}_{\text{control}} = \frac{\mu_B g}{\hbar} S_x B_x \cos(\omega t + \phi) \quad (2.17)$$

where we have assumed that the control field is applied along the x-axis of the defect. In the low driving limit, the rotating wave approximation leads to an analytical expression for the probability of residing in the  $m_s = -1$  projection as a function of time, given an initial state of  $m_s = 0$ , given by

$$P_1(t, \Omega_0, \delta) = \frac{\Omega_0}{\sqrt{\Omega_0^2 + \delta^2}} \sin^2 \left( \frac{\sqrt{\Omega_0^2 + \delta^2}}{2} t \right), \quad (2.18)$$

where  $\Omega_0 = \mu_B g B_x / \hbar$  characterizes the on-resonance driving strength, and  $\delta = \omega - \omega_0$  is the detuning. The characteristic oscillation between the two eigenstates is a hallmark of a Rabi oscillation and represents coherent control over the quantum system with a classical electromagnetic field.

Most NV center experiments implement spin control with square amplitude-modulated

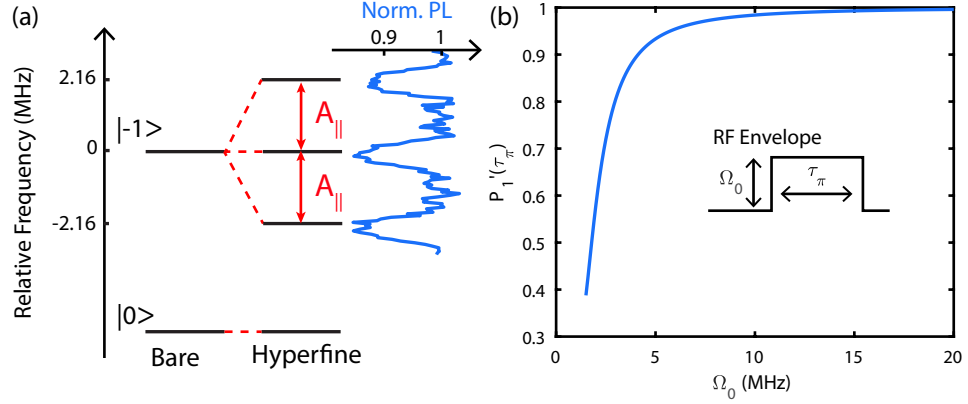


Figure 4:  $^{14}\text{N}$  Hyperfine Interaction and Single-Gate Errors. (a) schematic of how the hyperfine interaction splits the  $|0\rangle \leftrightarrow |-1\rangle$  transition into a triplet. Measured optically detected magnetic resonance for an NV center depicting the hyperfine splitting. (b) Calculated probability of residing in the  $m_s = -1$  spin state following a  $\pi$ -pulse for different resonant driving strengths.

RF pulses with a duration and amplitude calibrated to rotate the quantum state on the Bloch sphere by  $\pi/2$  or  $\pi$  radians, which we refer to as a  $\pi/2$ -pulse and  $\pi$ -pulse. This is largely due to experimental and theoretical convenience. Generating a square pulse with varying durations is easily achieved with off-the-shelf RF modulators and this scenario can be analytically solved, resulting in Eq. 2.18. However, there exist complications due to the always-present nitrogen hyperfine coupling. For the following discussion, we will consider the most common nitrogen isotope,  $^{14}\text{N}$ , with  $A_{\parallel} = 2.16\text{ MHz}$  [153]. Due to the  $S = 1$  character, the  $m_s = 0 \leftrightarrow m_s = -1$  transition splits into a triplet, with the splitting given by  $A_{\parallel}$  [Fig. 4(a)]. Thus, if the central frequency is chosen for a  $\pi$ -pulse, two-thirds of all experimental trials will be using a control pulse with  $|\delta| = A_{\parallel}$ . This amounts to a correlated single-gate error due to the fact that the nitrogen nuclear spin lifetime is longer than most trials [124]; however, it can vary between repeated trials. This can be quantified using the expression

$$P_1'(t, \Omega_0) = \frac{1}{3} (P_1(t, \Omega_0, 0) + 2P_1(t, \Omega_0, A_{\parallel})), \quad (2.19)$$

where the off-resonant contribution is doubled due to the two satellite resonances induced by the nuclear  $m_I = \pm 1$  projections.

There are two pulse regimes that are typically used for these types of transitions, which using nuclear magnetic resonance terminology [168] are the “hard” and “soft” pulses. Hard pulses are high-power, short duration pulses that attempt to overcome the detuning introduced by the perturbation. Figure 4(b) depicts how the quality of a hard pulse increases with increasing Rabi driving strength. To achieve at least 90% population inversion, a driving strength of  $2 \times A_{\parallel}$  is required. Hard pulses are heavily used in NV experiments that aren’t exerting control over the nitrogen nuclear spin. Soft pulses are low-power, long duration pulses that attempt to drive a single hyperfine split transition. These pulses have enabled the demonstration of a  $C_n\text{NOT}_e$  gate [30] and enabled single-shot readout of the nitrogen nuclear spin at room temperature [67, 124].

### 2.3.3. Ground State Spin Dynamics

There are two types of characteristic time scales that describe the behavior of any multi-level spin system: the longitudinal relaxation time,  $T_1$ , and dephasing time,  $T_2$  [1].  $T_1$  can be intuitively thought of as the time scale at which a “bit-flip” occurs, whereas  $T_2$  is the time scale at which a “phase-flip” between a superposition of spin states occurs. In a perfect environment, the dephasing time is limited by the relaxation time scale, although this regime is often not achieved in experimental settings. For a single NV center in bulk diamond,  $T_1 \approx 5$  ms and is limited by interactions with phonons [44].  $T_2$ , in contrast, is affected through a spin-spin interaction and thus depends on the specifics of the diamond’s spin bath [167]. For high-purity type IIa diamond, the dominant spin bath is due to the  $^{13}\text{C}$  ( $I = 1/2$ ) concentration [120]. For natural  $^{13}\text{C}$  abundance (1.1%),  $T_2 \approx 200$   $\mu\text{s}$ , although this value can change depending on the local environment. In  $^{12}\text{C}$  ( $I = 0$ ) isotopically enriched diamond,  $T_2 \approx 1.8$  ms. Examples of these measurements are included in Appendix B. These relatively long  $T_2$  times have lead to the abundance of NV center equipped sensors of both classical and quantum magnetic fields [142], where the inverse of the dephasing time is proportional to the minimum resolvable field (see § 3.2.5 for more detail). Recently, open-loop quantum feedback, achieved through dynamical decoupling, has been applied to

NV centers [38, 144]. These noise-suppressing protocols can extend the dephasing time in non-isotopically purified diamond to greater than 1 ms [12].

## 2.4. Charge and Spin Initialization

The charge and spin initialization fidelity of a single NV center has important consequences for all experiments and applications. Improved charge initialization fidelity results in higher contrast signals for rare-event detection [172] and improves the gate fidelity when using the NV center as an ancilla [124]. While less studied, improved spin initialization fidelity results in similar benefits. This section overviews the current understanding of NV center charge and spin initialization fidelity.

### 2.4.1. Charge Initialization

As stated in Section 2.2, during and after optical illumination the NV center resides in a mixed population of  $NV^-$  and  $NV^0$ . Waldherr et al. [171] demonstrated that under 532 nm illumination the center is in  $\sim 75\%$   $NV^-$ . Aslam et al. [8] confirmed that this initialization fidelity is the maximum attainable for a single visible wavelength. The limitation to this 75%  $NV^-$  population is not well understood on a microscopic level as there are many factors to consider such as the  $NV^-$  singlet-shelving state and the exact cross sections for the two two-photon conversion processes. Strategies for improving the initial charge fidelity have relied on doping, both chemically and electronically, and post-selecting data. For electrical doping, near-unity initialization fidelity into  $NV^0$  can be achieved but the  $NV^-$  fidelity cannot be increased above 75% [47, 133]. Chemical doping offers a more promising route. Adding significant amounts of phosphorous donors in the diamond increases the  $NV^-$  fidelity to over 99% [46]. However, this comes at the expense of incorporating significant electronic spins into the diamond which reduces the coherence properties, negating any benefits of improved charge purity. By incorporating a short charge state check prior to experiments, trials in which the center was likely in  $NV^-$  can be selected out after the experiment [172]. This results in drastically reduced trials with improved contrast. Post-selection works well for

removing charge-induced artifacts and detecting rare events; however, it is not compatible with sensing protocols where averaging is often favored over maximizing single-shot SNR.

#### 2.4.2. Spin Initialization

Spin initialization into the  $m_s = 0$  projection results from the highly spin-selective ISC [44]. The upper and lower branches work together to polarize the spin state: the upper branch is much more likely to shelve the  $m_s = |1\rangle$  states into the singlet [61], whereas the lower branch is more likely to populate the ground state  $m_s = 0$  projection [92, 165]. While qualitatively it is known there is spin polarization, quantitatively determining the exact value has proven challenging. There are four strategies for measuring the spin polarization: Ramsey interferometry on an electron or nuclear spin coupled to the NV under question [127], fitting to a weighted bi-exponential fluorescence decay under pulsed excitation [53, 137], optical master equation modeling [66], and single-shot determination [138]. At room temperature, there does not exist a single-shot readout and thus the other three strategies are employed. The spin state initialization reported in the literature from these techniques is quite vast, ranging from 46% to 90% [53, 89, 127, 137, 172, 173]. One source of discrepancy in these measurements is the dependence of spin polarization on pumping rate [29]. Spin polarization can be reduced by up to 14% by pumping above optical saturation. As it currently stands, the best way to initialize the spin state is to pump at or below the optical saturation power for  $\sim 1 - 2 \mu\text{s}$ . In this thesis, I determine a spin polarization of  $\approx 90\%$  using the pulsed excitation technique while controlling for pulse errors (see Appendix C).

### 2.5. The NV Center as a Qubit

The DiVincenzo criteria outline the required traits a system must exhibit in order to build a quantum computer [41]. These criteria generally hold for a quantum sensor as well. A quantum sensor must have the following properties:

1. A well-characterized qubit with resolvable states

2. Long decoherence times
3. Universal control of the qubit state
4. An initialization mechanism into a known state
5. A qubit state readout mechanism

As has been discussed in the previous sections, the negatively charged NV center satisfies these criteria. The qubit states consists of the ground-state triplet spin manifold, where the two levels are  $|0\rangle$  and one of the  $|\pm 1\rangle$  states. The ground-state spin exhibits coherence times approaching milliseconds at room temperature, and the state can be controlled on the order of tens of nanoseconds. Optical pumping through the intersystem crossing leads to spin initialization, and the same dynamics can be used to infer the relative spin population. These properties have lead to the many demonstrations of the NV center as a quantum sensor, but as mentioned in Chapter 1, there are limitations associated with the initialization and readout mechanisms. These will be addressed in the remainder of this thesis.

While the NV center is an outstanding single qubit for sensing purposes, it can also be used for quantum computation. NV centers can act as an ancilla to entangle nuclear spins, leading to a 10-qubit system with all-to-all connectivity [22]. Furthermore, the NV center is an ideal spin-photon interface [25], and is one of the leading contenders for building a quantum repeater [83], a necessary component for distributing entanglement across long distances. Thus, the NV center plays a large role in a host of different pursuits in quantum information science.

## CHAPTER 3 : Spin Readout: Theory and Implementation

Portions of this chapter have been adapted from D. A. Hopper et al. “Spin Readout Techniques of the Nitrogen-Vacancy Center in Diamond” *Micromachines* 9, 437 2018 [80], published under a Creative Commons Attribution License (CC BY 4.0). Portions of this chapter were completed in collaboration with Henry Shulevitz.

### 3.1. Introduction

The ability to measure the state of a qubit is one of the necessary requirements for quantum information processing [41]. The issue of precision measurement is one of the oldest and most subtle aspects of quantum theory — and arguably the most essential for many practical applications. Several authors have reviewed general considerations for quantum measurements [32, 128]. In this thesis, I will consider projective measurements of the NV<sup>-</sup> electron spin; however, the NV center can be used as an ancilla qubit for other spin systems where quantum nondemolition [107, 124] and weak [134] measurements are possible. This chapter is outlined as follows: Section 3.2 describes the formal methods for quantifying the performance of spin readout of NV centers; Section 3.3 describes traditional photoluminescence (PL) based spin readout; and Section 3.4 overviews Spin-to-Charge Conversion (SCC) spin readout, the technique that this thesis is largely centered around.

### 3.2. Quantifying Readout Performance

Various metrics are used by the NV community to quantify readout performance, each with intuitive advantages for specific applications. As we show in this section, the common metrics all relate to the signal-to-noise ratio (SNR) of the measurement, which provides a useful basis to compare different readout techniques. We consider projective measurements where the goal is to distinguish between two quantum states,  $|0\rangle$  and  $|1\rangle$ . Therefore, we

define the SNR for a differential measurement,

$$\text{SNR} = \frac{\langle S_0 \rangle - \langle S_1 \rangle}{\sqrt{\sigma_0^2 + \sigma_1^2}}, \quad (3.1)$$

where  $\langle S_i \rangle$  is the mean signal for a single measurement of spin state  $|i\rangle$ , and  $\sigma_i$  is the associated noise. Classical signal processing [118] and superconducting qubits [169] both employ an analogous definition of differential SNR. In the following subsections, we discuss common optical-detection signals and their associated SNR, relate the SNR to other spin-readout metrics, and discuss how to include averaging over multiple experimental cycles.

### 3.2.1. Photon summation

In many situations, the signal is simply the number of photons detected in a fixed readout cycle. In this case, Eqn. 3.1 takes the form

$$\text{SNR} = \frac{\alpha_0 - \alpha_1}{\sqrt{\alpha_0 + \alpha_1}}, \quad (3.2)$$

where  $\alpha_i$  is the mean number of detected photons for a single measurement of spin state  $|i\rangle$ . Here we assume  $\alpha_0 > \alpha_1$  and that the noise in each signal is dominated by photon shot noise, with variance  $\sigma_i^2 = \alpha_i$ . The SNR is related to the dimensionless contrast between the two signals,

$$C = \left(1 - \frac{\alpha_1}{\alpha_0}\right), \quad (3.3)$$

such that the photon-summation SNR can be recast as

$$\text{SNR} = \sqrt{\alpha_0} \times \frac{C}{\sqrt{2 - C}}. \quad (3.4)$$

This formulation clearly separates the SNR's dependence on photon collection efficiency and spin contrast. Note that our definition of  $C$  differs from the related metric used by some authors,<sup>1</sup> which we term the visibility,  $V = (\alpha_0 - \alpha_1)/(\alpha_1 + \alpha_0)$ . For the case

---

<sup>1</sup>Adding to potential confusion, the dimensionless parameter  $C$  defined in the seminal work by Taylor et al. [161] is neither the contrast nor the visibility, but is rather the inverse of the spin-readout noise,

of NV centers, it is natural to define the contrast as in Eqn. (3.3) since  $\alpha_0$  is related to the optically pumped initial spin state and often appears in defining the normalized PL,  $S/\alpha_0$ . For an NV center in bulk diamond, typically  $C \approx 0.3$  using the traditional PL-based readout approach. In the limit of perfect contrast ( $C = 1$ ), the photon-summation SNR is limited by shot noise alone.

### 3.2.2. Thresholding

If many photons are detected during a single measurement cycle, the photon summation technique becomes less efficient than assigning a discrete outcome based on a threshold condition [34]. In this scenario, the signal is modeled by the sum of two photon probability distributions (typically Poissonian or Gaussian) with different means. A threshold value is selected to distinguish between the two distributions, resulting in a binomial random variable specifying the outcome 0 or 1. For example, suppose the  $|0\rangle$  state generates a detected number of photons that exceeds the threshold (yielding binary  $S = 1$ ) with probability  $p_{0|0}$ , whereas  $|1\rangle$  generates a detection event that exceeds the threshold with probability  $p_{0|1}$ . Here  $p_{0|0}$  is the true positive rate, implying a false negative rate  $\epsilon_0 = 1 - p_{0|0}$ , whereas  $\epsilon_1 = p_{0|1}$  is the false positive rate. The readout fidelity, a measure of the confidence in a given measurement outcome, is defined in terms of these two error rates as [34, 35]

$$\mathcal{F} = 1 - \frac{1}{2}(\epsilon_0 + \epsilon_1). \quad (3.5)$$

The fidelity takes values between 50% and 100%, assuming an optimal threshold condition has been selected.

The binomial nature of thresholded readout facilitates the direct evaluation of the signal mean and variance for an initial spin state  $|i\rangle$ ,

$$\langle S_i \rangle = p_{0|i} \quad (3.6)$$

---

discussed in §3.2.3.

$$\sigma_i^2 = p_{0|i}(1 - p_{0|i}), \quad (3.7)$$

from which we can calculate the corresponding differential SNR directly from Eqn. (3.1):

$$\text{SNR} = \frac{p_{0|0} - p_{0|1}}{\sqrt{p_{0|0}(1 - p_{0|0}) + p_{0|1}(1 - p_{0|1})}}. \quad (3.8)$$

Assuming symmetric error probabilities,  $\epsilon_0 = \epsilon_1$ , Eqn. (3.8) takes the simplified form

$$\text{SNR} = \frac{2\mathcal{F} - 1}{\sqrt{2\mathcal{F}(1 - \mathcal{F})}}. \quad (3.9)$$

This formulation provides a standard criterion, sometimes quoted in the literature, for determining whether a quantum state readout is single-shot; a readout fidelity  $\mathcal{F} > 79\%$  corresponds to an  $\text{SNR} > 1$ .

Often times, the measured value of  $\mathcal{F}$  is less than would be predicted from the ideal signal SNR [73, 112, 138]. This discrepancy stems from backaction — unwanted state changes during the measurement — and also potentially from improper state initialization. We will discuss these issues below in the context of different readout techniques.

### 3.2.3. Spin-Readout Noise

In a quantum sensor, the environmental state is mapped onto the qubit state such that the information is contained in a population difference, resulting in a stochastic signal whose mean is given by

$$\langle S \rangle = \cos^2\left(\frac{\theta}{2}\right) \langle S_0 \rangle + \sin^2\left(\frac{\theta}{2}\right) \langle S_1 \rangle. \quad (3.10)$$

Here, the angle  $\theta$  depends on some external field (resulting, for example, from free evolution under an external magnetic field,  $B$ , such that  $\theta \propto B$ ). The minimum resolvable angular shift,  $\delta\theta$ , corresponds to the situation when the change in signal exceeds the noise,  $\sigma_S$ . Mathematically,

$$\delta\theta = \frac{\sigma_S}{\left| \frac{\partial \langle S \rangle}{\partial \theta} \right|}. \quad (3.11)$$

For an ideal measurement,  $\langle S_0 \rangle = 0$ ,  $\langle S_1 \rangle = 1$  and  $\sigma_0 = \sigma_1 = 0$ . However, the ideal measurement still exhibits noise due to the stochastic projection of qubit states. This projection noise is the basis for the standard quantum limit (SQL) for detecting angular shifts in a single measurement. Since projection is a binomial process, the variance of the signal depends on  $\theta$  similarly to the case of Eqn. (3.7) for thresholded measurements:

$$\sigma_{\text{SQL}} = \sqrt{p_0(\theta)[1 - p_0(\theta)]} = \frac{1}{2} \sin(\theta). \quad (3.12)$$

Since the change in signal varies identically,

$$\frac{\partial \langle S_{\text{SQL}} \rangle}{\partial \theta} = \frac{1}{2} \sin(\theta), \quad (3.13)$$

the SQL for a single-shot measurement is a constant angle given by  $\delta\theta_{\text{SQL}} \equiv \theta_0 = 1$  radian.

Given this fundamental limit, it is illustrative to define a parameter that quantifies the effect of realistic, imperfect measurements. The *spin-readout noise*,

$$\sigma_R \equiv \frac{\sigma_S}{\left| \frac{\partial \langle S \rangle}{\partial \theta} \right|_{\theta_0}}, \quad (3.14)$$

is a dimensionless quantity  $\geq 1$ , where a value  $\sigma_R = 1$  signifies a measurement at the SQL [150, 161]. The minimum experimentally resolvable angular shift is then given by

$$\delta\theta = \theta_0 \sigma_R. \quad (3.15)$$

This formulation explicitly separates the resolution limit into two categories: the quantum mechanical noise ( $\theta_0$ ) and experimental noise ( $\sigma_R$ ). A related metric, also called the readout fidelity by some authors [111, 161], is simply the inverse,  $\sigma_R^{-1}$ . This definition of readout fidelity spans the range  $(0, 1]$ , where unity indicates an ideal measurement, and it differs fundamentally from the traditional definition of quantum readout fidelity (Eqn. 3.5). We use the traditional definition for  $\mathcal{F}$  in the remainder of this thesis.

### 3.2.4. Averaging

The preceding discussion concerns single-shot readout of individual qubits. In many cases, it is advantageous to repeat the measurement (including, usually, a full experimental cycle of initialization and coherent evolution) many times in order to identify small signals. This is especially true when the single-shot SNR is well-below unity. Assuming independent trials, the SNR formulation provides a simple means for calculating the time-averaged SNR, namely,

$$\langle \text{SNR} \rangle = \sqrt{N} \times \text{SNR}, \quad (3.16)$$

where  $\langle \rangle$  signifies the time-average and  $N$  is the number of measurements. The parameter  $N$  can account for measurements averaged in space (for ensembles of identical qubits) or time (for repeated measurements). In the remainder of this thesis, we consider especially the case of time-averaging, where  $N$  is related to the total integration time, and Eqn. (3.16) allows for the direct comparison of different measurement techniques while accounting for the overhead from varying measurement durations. Especially for sensing applications, it bears remembering that qubit ensembles offer an additional improvement that scales with the square root of the ensemble size.

### 3.2.5. Sensitivity

Sensors generally aim to acquire as much information as possible about an environmental state before it changes. Accordingly, we must quantify the tradeoff between signal amplitude and measurement bandwidth. Usually, signals are averaged over many experimental cycles, and it is useful to define the field sensitivity,

$$\eta = f(\theta_0) \sigma_R \sqrt{\tau}, \quad (3.17)$$

where the function  $f(\theta_0)$  relates the SQL to a particular field amplitude, and  $\tau$  is the time it takes to perform a single measurement cycle, including initialization, operation and readout. The sensitivity has dimensions of [field amplitude]  $\cdot \text{Hz}^{-1/2}$ , and the minimum

resolvable field can be estimated by dividing  $\eta$  by the square root of total integration time. Barring additional noise sources or instability in the field to be measured, arbitrarily low fields can be resolved by integrating for longer times.

Two common sensing applications are the detection of dc and ac magnetic fields [39, 161]. For the case of dc magnetic fields, the field amplitude is mapped onto a quantum phase difference using a Ramsey sequence, with a corresponding SQL given by

$$f_{B_{\text{dc}}}(\theta_0) = \frac{\hbar}{g\mu_B T_2^*} \theta_0, \quad (3.18)$$

where  $g$  is the gyromagnetic ratio,  $\mu_B$  is the Bohr magneton, and  $T_2^*$  is the inhomogeneous spin dephasing time. Dropping the factor  $\theta_0 = 1$ , the corresponding sensitivity is

$$\eta_{B_{\text{dc}}} = \frac{\hbar}{g\mu_B} \sqrt{\frac{T_2^* + t_I + t_R}{(T_2^*)^2}} \sigma_R, \quad (3.19)$$

where  $t_I + t_R$  is the time required to initialize and read out the spin state, which will be referred to as measurement overhead in this review. Similarly, oscillating magnetic fields are detected by implementing a Hahn echo or dynamical decoupling sequence to accumulate phase. In this case, the ac field resolution is

$$f_{B_{\text{ac}}}(\theta_0) = \frac{\pi\hbar}{2g\mu_B T_2} \theta_0, \quad (3.20)$$

where  $T_2$  is the homogeneous spin dephasing time, and the corresponding sensitivity is

$$\eta_{B_{\text{ac}}} = \frac{\pi\hbar}{2g\mu_B} \sqrt{\frac{T_2 + t_I + t_R}{(T_2)^2}} \sigma_R. \quad (3.21)$$

In general, both  $\sigma_R$  and  $\eta$  depend on the average value of  $\theta$  at which the measurement is performed. In most cases, however, the optimum conditions for sensing is very close to  $\theta = \pi/2$ . Making this assumption, we derive the following analytic expressions for the

Metric	Relation to SNR	Use Case
Contrast, $C$ , & Count rate, $\alpha_0$	$\text{SNR} = \sqrt{\alpha_0} \frac{C}{\sqrt{2-C}}$	traditional PL readout
Spin-readout noise, $\sigma_R$	$\text{SNR} = \sqrt{\frac{2}{\sigma_R^2 - 1}}$	magnetometry
Fidelity, $\mathcal{F}$	$\text{SNR} = \frac{p_{0 0} - p_{0 1}}{\sqrt{p_{0 0}(1-p_{0 0}) + p_{0 1}(1-p_{0 1})}}$	algorithms, large signals
Repeats for $\langle \text{SNR} \rangle = 1$	$N = \left(\frac{1}{\text{SNR}}\right)^2$	general use

Table 1: Compilation of spin-readout metrics, their formal relation to differential SNR, and common use cases.

spin-readout noise for the cases of photon summation,

$$\sigma_R^{\text{Photon}} = \sqrt{1 + 2 \frac{\alpha_0 + \alpha_1}{(\alpha_0 - \alpha_1)^2}}, \quad (3.22)$$

and for thresholding,

$$\sigma_R^{\text{Threshold}} = \sqrt{1 + 2 \frac{p_{0|0}(1-p_{0|0}) + p_{0|1}(1-p_{0|1})}{(p_{0|0} - p_{0|1})^2}}. \quad (3.23)$$

Derivations are included in Appendix D. In both cases, the spin-readout noise is directly related to the differential SNR, following the general expression

$$\sigma_R = \sqrt{1 + \frac{2}{\text{SNR}^2}}. \quad (3.24)$$

For  $\text{SNR} < 1$ , which is often the case for NV centers, the spin readout noise is approximately the inverse of the SNR. This can be seen by expanding Eqn. 3.24

$$\sigma_R = \frac{\sqrt{2}}{\text{SNR}} + \frac{\text{SNR}}{2\sqrt{2}} - \frac{\text{SNR}^3}{8 \times 2^{3/2}} + \dots \quad (3.25)$$

Thus, the figure of merit of  $\text{SNR} = 1$  can also be interpreted as the measurement efficiency at which spin projection noise must be taken into account.

### 3.2.6. Summary

Particular applications benefit from different aspects of the spin-readout metrics described in the previous subsections. For example, quantum algorithms generally demand single-shot readout with small error probabilities. Therefore, readout fidelity is the most informative choice. Magnetometry and sensing applications, on the other hand, usually rely on time-averaging and are inherently subject to the standard quantum limit; in this case spin-readout noise is the most illuminating metric. Each of these metrics can be related to the SNR, which serves as a useful basis of comparison across multiple techniques. Table 1 summarizes the three metrics discussed in this section and their relation to SNR.

In some experimental situations, a critical experimental design consideration is whether to use photon summation or thresholding. To decide, we can compare the thresholding SNR (Eqn. 3.8) to the photon summation SNR (Eqn. 3.2) and choose the higher value. Typically, thresholding becomes more efficient when one of the spin states produces  $> 1$  photon in a measurement and the contrast exceeds 50%. We hope that the connections between these metrics and various measurement techniques described in the following sections will aid in selecting the optimal approach for future applications.

## 3.3. Traditional Photoluminescence Spin Readout

The most common spin readout technique for NV centers leverages the spin-dependent photoluminescence under 532 nm illumination. This relatively simple to implement technique has the added benefit that it also re-initializes the charge and spin state (see Section 2.4). However, this re-initialization time scale is fast, limited by the ground-state ISC lifetime of  $\sim 200$  ns, and thus very few photons are detected in a single measurement. This hurdle is overcome by repeating the experiment many times (as discussed in Section 3.2) and has enabled many experiments to date. This section discusses a physical picture of the NV center's electronic structure that explains PL-based readout and overviews how to calibrate the experimental settings for optimal SNR.

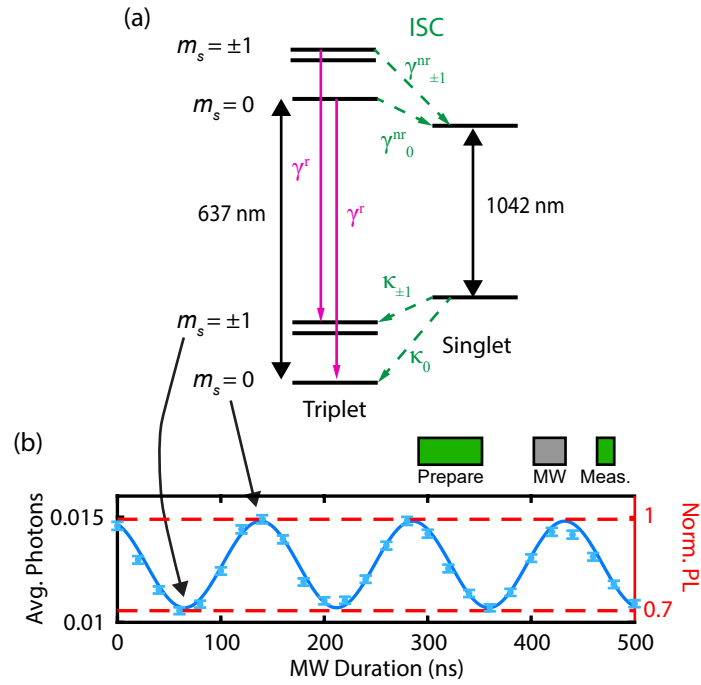


Figure 5: Traditional PL Spin Readout. (a) Room temperature electronic structure of the NV<sup>-</sup> center. Radiative transitions are solid magenta lines, nonradiative transitions are dashed green lines. ZPLs are black double arrows. (b) Rabi mutations of the ground-state spin. The y-axis is the average number of detected photons for an NV in a planar diamond substrate.

Under visible illumination (typically 532 nm), the NV center emits PL in its  $\approx 650$ –750 nm phonon sideband (PSB) whose intensity depends on the ground-state spin projection. Physically, spin-dependent PL arises from spin-orbit interactions within the inter-system crossing (ISC) that couples the triplet and singlet manifolds [60, 167]. As shown in Figure 5(a), the excited state triplet levels can undergo radiative transitions back to the ground state or nonradiatively decay into the meta-stable singlet manifold. The total decay rate of the excited state spin projection  $|i\rangle$  is given by the sum of these two rates, namely

$$\gamma_i = \gamma^r + \gamma_i^{\text{nr}}. \quad (3.26)$$

The radiative rate,  $\gamma^r$ , is essentially spin independent, whereas the nonradiative rates,  $\gamma_i^{\text{nr}}$ , depend strongly on the spin projection due to the spin-dependent ISC. Recent studies conclude that  $\gamma_{\pm 1}^{\text{nr}} \approx 10\gamma_0^{\text{nr}}$  [60, 66, 78]. This difference produces a transient response to illumination that is drastically different depending on the initial projection of the ground-state spin.

Assuming the NV center is illuminated with an optical excitation rate similar to  $\gamma^r$  (*i.e.*, close to optical saturation, which is generally ideal for traditional PL readout), a spin population initially in  $m_s = \pm 1$  is shelved into the singlet manifold within only a few optical cycles of the triplet states, whereas a population in  $m_s = 0$  continues to cycle and produce PL. This spin-dependent PL contrast is the essence of traditional readout. The contrast is short-lived, however; it vanishes after about 300 ns as the singlet population decays back to the triplet ground-state [2], and the system reaches a steady state [Fig. 6(a)]. Taking into account the spin selectivity of both the triplet-to-singlet and singlet-to-triplet ISC (the latter is less spin selective than the former), the resulting ground-state spin population after the illumination is switched off is  $\approx 80\%$  polarized into the  $m_s = 0$  sublevel [44, 137, 171], although work reported in this thesis constrains this value closer to  $\approx 90\%$  [see Appendix C]. This optically pumped pseudopure state generally serves as the initialized  $|0\rangle$  state for subsequent quantum experiments while one of the  $m_s = \pm 1$  state serves as the  $|1\rangle$  state.

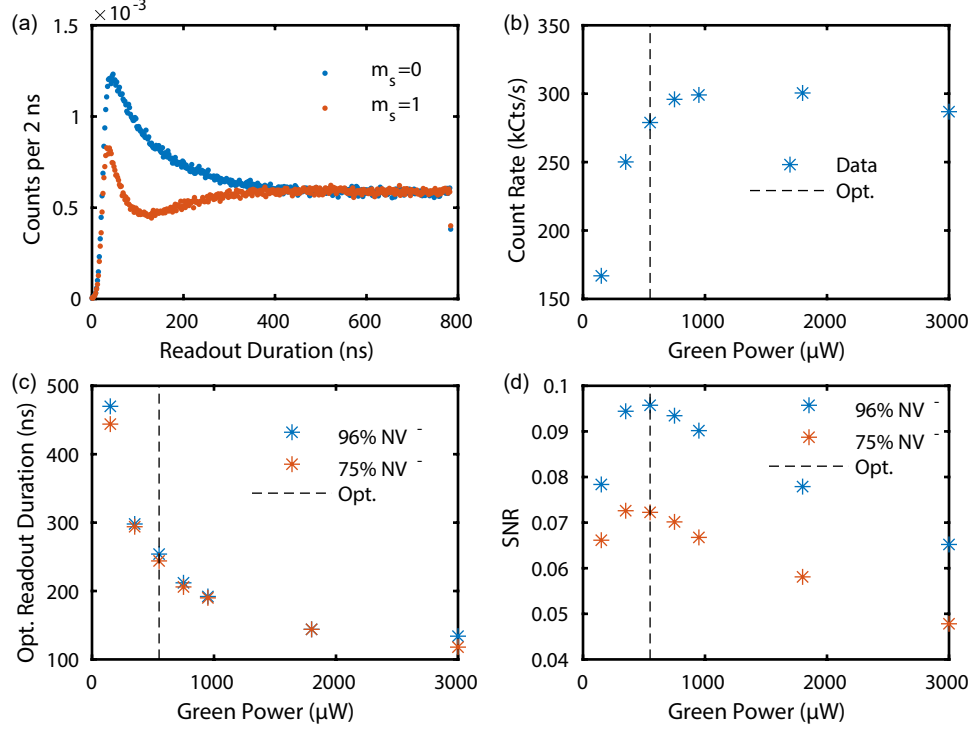


Figure 6: Calibrating PL Spin Readout. (a) Example transient response due to the two spin states with 532 nm illumination. (b) The steady state count rate for different 532 nm powers depicting saturation. (c,d) The optimum spin readout SNR and the corresponding power and readout duration as well as how they vary for different powers and initial  $\text{NV}^-$  populations. Data was taken with a single NV center within a solid immersion lens.

Two experimental parameters control the PL spin SNR: power and readout duration. The optimal settings can be found by repeating the transient PL response measurement, as seen in Fig. 6(a), for different powers below, at, and above optical saturation [Fig. 6(b)]. By calculating the total accumulated photons for both spin states and calculating the SNR (Eqn. 3.2), the optimum settings can be found empirically [Figs. 6(c,d)]. The optimum SNR is quite sensitive to power, as can be seen in Fig. 6(d), and care should be taken to ensure the correct parameters are used. If a high-resolution transient measurement cannot be performed, a lower-resolution version can suffice. This is achieved by changing the width of the readout duration for the chosen powers, and counting the average detected photons in the various readout duration bins. A rule-of-thumb for selecting the settings for PL readout is to use a power near optical saturation [Fig. 6(b)] and a readout duration of 250 ns.

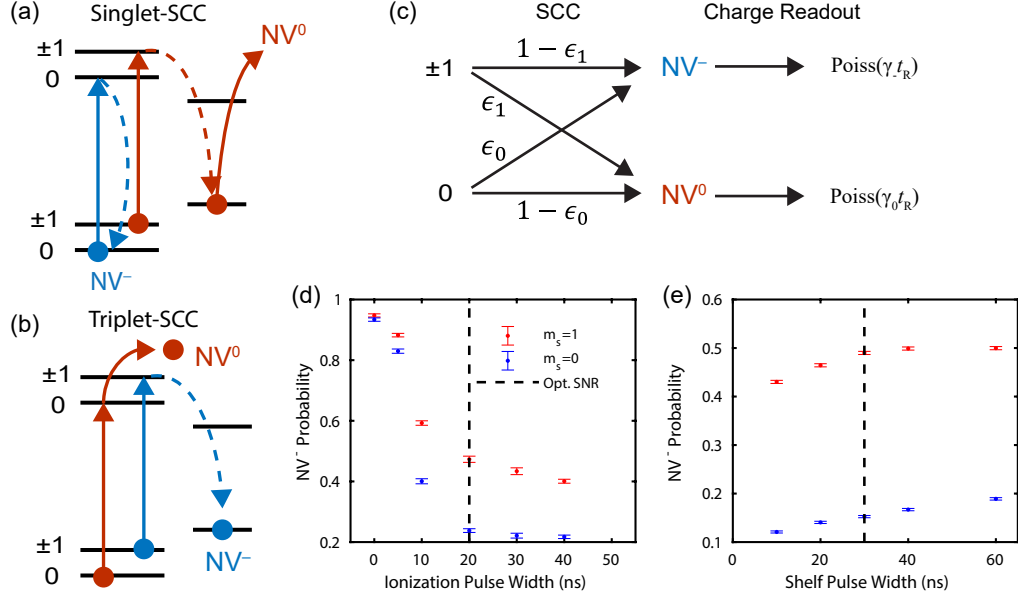


Figure 7: Spin-to-Charge Conversion. (a,b) Schematics of the spin-dependent ionization pathways for Singlet-SCC (S-SCC) and Triplet-SCC (T-SCC), respectively. Solid lines represent laser induced transitions, while dashed lines represent decay transitions. (c) The SCC readout process can be modeled by a binary asymmetric channel followed by a Poisson channel. (d) T-SCC Ionization pulse width optimization without a shelf. (e) T-SCC shelf width ionization optimization with a 20 ns shelf.

Figure 5(b) shows a typical example of room-temperature Rabi nutations for a single NV center in bulk diamond, with the data plotted in terms of both the average number of photons detected per shot and the corresponding normalized PL. The spin contrast is  $C=30\%$ , and the confocal setup collects  $\alpha_0=0.015$  photons on average from the  $|0\rangle$  spin state, using an  $NA=0.9$  air objective to image an NV center  $\approx 4\mu\text{m}$  beneath a planar diamond surface with a saturated count rate of  $50\text{ kCts s}^{-1}$  under CW 532 nm illumination. Using Eqn. 3.2, the corresponding single-shot SNR is 0.03, and Eqn. 3.16 implies that more than  $10^5$  repeats are required to achieve  $\langle\text{SNR}\rangle = 10$ . Each point in Figure 5(c) consists of  $4 \times 10^5$  repeats. In many applications, such averaging places severe limitations on performance and efficiency. This experimental setting provides a useful benchmark when considering the performance of other advanced readout techniques.

### 3.4. Spin-to-Charge Conversion

Whereas incomplete PL contrast and spin repolarization limit the fidelity of traditional spin measurements, the NV center’s charge state can be measured optically with high precision, even at room temperature (see § 2.2.3). Given a means for mapping spin projections onto charge populations, or spin-to-charge conversion (SCC), charge measurements provide an alternate means to boost the spin-readout fidelity. SCC mechanisms are widely used in other spin-qubit platforms including quantum dots [50] and silicon donors [122]. In this section, I will cover two related mechanisms for all-optical SCC that exploit the NV center’s ISC dynamics and discuss calibration strategies.

SCC can be achieved in two related ways, as shown in Figs. 7(a,b). Both techniques leverage the strong spin-selectivity of the ISC from the NV center’s  $^3E$  triplet excited state to the singlet manifold. Following a single excitation event, a spin initially in  $m_s = \pm 1$  crosses to the singlet state with  $\approx 50\%$  probability, whereas the  $m_s = 0$  state undergoes ISC only 5% of the time [60]. Therefore, both techniques begin with a shelving step, consisting of a short,  $< 20$  ns, visible pulse of light that excites the triplet manifold with high probability. After waiting for a time longer than the  $^3E$  excited-state lifetime (typically  $\approx 20$  ns), a large fraction of the initial  $m_s = \pm 1$  spin population is stored in the metastable singlet ground state. Next, an intense ionization pulse resonant with either the singlet absorption band [900-1042 nm, Fig. 7(a)] or the triplet absorption band [500-637 nm, Fig. 7(b)], is applied to ionize the singlet or triplet populations, respectively. Hereafter, the methods will be referred to as singlet-SCC and triplet-SCC, depending on which manifold is ionized.

The two methods each have advantages and disadvantages. Triplet-SCC relies on a highly efficient two-photon ionization process for the triplet using  $\approx 600$ -637 nm light [8, 150]. This can be the same color used for both the shelving step and subsequent charge readout [78], which simplifies experiments. However, the triplet-SCC efficiency is ultimately limited by the 50% ISC probability for  $m_s = \pm 1$  spin states, since any population that remains in the triplet after the shelving step is ionized. Shields et al. [150] essentially reached the

practical limit for this technique, demonstrating a single-shot  $\mathcal{F} = 67\%$ , corresponding to an SNR increased by a factor of 4.1 over traditional PL (the SNR ratio in this case is limited by the high collection efficiency in this experiment).

Singlet-SCC, on the other hand, leaves the triplet population unaffected, and the shelving procedure can be rapidly repeated, ideally to reach the maximum SCC efficiency given by the  $\approx 10:1$  spin-dependent ISC branching ratio. Drawbacks of this approach include the need for both visible and near-infrared optical beams, and the small optical cross section for the singlet optical transition [2], which necessitates a high-intensity near-infrared pulse to achieve 100% ionization efficiency. For a singlet ionization probability 25%, the singlet-SCC protocol achieved a maximum  $\mathcal{F} = 62\%$ , corresponding to an SNR increase by a factor of 5.8 over traditional PL [78]. The infrared pulses used by Hopper et al. [78] were derived from a supercontinuum laser, bandpass filtered to 900-1000 nm, with an average picosecond pulse energy of 2 nJ, this is discussed in more detail in Chapter 5. Since the ionization rate depends quadratically on pulse energy, increasing the pulse energy by an order of magnitude should lead to ionization probabilities exceeding 99%. Assuming 100% ionization can be achieved using higher optical pulse energies, the SNR is expected to exceed 0.8 ( $\mathcal{F} > 75\%$ ) and result in a factor-of 15 increase over traditional PL readout.

Both readout techniques are explained by the same model. The two spin projections are mapped probabilistically onto two different charge states which produce a Poisson variable with different means [Fig. 7(c)]. This can be intuitively thought of as a spin-dependent weighted coin flip deciding which Poisson mean to sample from. The first stage, SCC, is achieved by selecting the desired protocol, either triplet or singlet, and then calibrating the pulse durations for the experimental setup. An example of this for Triplet-SCC can be seen in Figures 7(d,e), where the ionization duration and shelving pulse width are swept over various ranges and the resulting  $NV^-$  population is recorded for the two spin states. A good starting point is to first calibrate the optimum ionization pulse width and power with no shelving pulse, followed by optimization of the shelving pulse width and power. If

the transient PL response due to the spin states has been previously recorded, the optimal shelving pulse coincides with the maximum instantaneous PL contrast observed in that data set. Otherwise, a shelving pulse duration and power sweep can also be run, with a fixed ionization power, to properly calibrate the conversion process.

The second stage, charge readout, determines the result of the SCC process. However, there is flexibility in how accurate the readout is performed as longer measurements lead to more accuracy in the charge state determination. Chapters 6 and 7 discuss in detail how the trade-off between charge readout duration and corresponding accuracy influence the total spin readout performance.

## CHAPTER 4 : Experimental Methods

In the course of this thesis, significant effort was devoted to creating robust methods for fabricating photonic and electronic structures on small diamond substrates as well improving data acquisition methods for the elimination of systematic noise. This chapter details these methods and is organized as follows: Section 4.1 discusses an *in-situ* alignment procedure of photonic structures to pre-selected NV centers; Section 4.2 details a procedure for fabricating lithographic wires on small diamonds for improved spin control; Section 4.3 presents an overview of multi-color confocal microscopy for NV center experiments; and Section 4.4 discusses experimental design considerations for time-domain measurements of NV center spin and charge dynamics.

### 4.1. Alignment of NV Centers to Photonic Devices

The NV's optical addressability in a solid-state host material provides both technological opportunities and formidable engineering challenges. Due to the high refractive index of diamond ( $n \approx 2.4$ ), total internal reflection at diamond-air interfaces severely limits the collection efficiency; even assuming an air objective with NA=0.95, a maximum fraction of only 4% of emitted photons can be extracted through a planar (100)-oriented surface [135]. Since the spin-readout noise is dominated by the Poisson statistics associated with counting photons, collection efficiency improvements that increase  $\alpha_0$  boost the single-shot SNR according to  $\sqrt{\alpha_0}$  (Eqn. 3.4) and reduce the averaging requirements according to  $N \propto 1/\alpha_0$ .

Advances in nanofabrication and photonic design have produced several top-down fabrication solutions to circumventing the diamond-air refractive index mismatch. The solid immersion lens (SIL), consisting of a hemisphere etched around an NV center [Fig. 8], overcomes total internal reflection such that only Fresnel reflection contributes to losses [69, 86, 115], and the latter can be further reduced using antireflective coatings. When used together with proper orientation of the diamond crystal, a SIL can increase the saturation

count rate to over  $1 \text{ MCts s}^{-1}$  [86, 138], resulting in an overall SNR improvement of a factor of 5 as compared to an NV in a (100)-oriented planar sample. Recently, I was involved in the development of a metalens constructed from nanopillars etched on the diamond surface which was used to image an NV center [82]. In contrast to the SIL, the metalens design collimates the emitted light, removing the need for a free-space objective and making it a promising approach towards coupling NV centers directly with optical fiber. Critical to these diffractive photonic structures is their alignment on the diamond surface to a pre-selected NV with favorable qualities. This section describes a procedure for registering the location of an NV center prior to SIL fabrication and discusses how this could be extended to a metalens.

The alignment procedure is shown schematically in Fig. 8. A 500 nm layer of PMMA A8 resist (MicroChem Nano PMMA) is spin coated onto the diamond surface. The resist is not baked to ensure the volatile solvent remains. The sample is then mounted in a confocal microscope on a rotation compensating mount (Thorlabs KM100T), which allows for precise tilt correction of the sample relative to the optical axis. The diamond surface is ensured perpendicular to the optical axis by moving the fast steering mirror (Optics in Motion OIM101) over  $80 \mu\text{m}$  and checking the relative height difference by observing the focal position of the green laser in a camera. The rotation compensating mount is used to offset any tilt in the  $x$  or  $y$  axis. A tilt angle that is within  $\pm 0.1^\circ$  of the optical axis is achievable with this method. After tilt correction, NV centers of a desired depth below the diamond surface are identified, typically  $3 \mu\text{m}$ , by imaging through the PMMA layer, which is transparent in the visible spectrum. The NV center depth is determined by finding the relative distance of the NV center from the surface of the diamond using PL as an indicator. Following the identification of a candidate NV center, the microscope is centered on the NV center, the beam is then focused on the PMMA layer, laser power is increased to  $\sim 100 \text{ mW}$  of 532 nm, and then five holes are burnt into the PMMA, 4 corners of an  $8 \mu\text{m}$  box surrounding the center of the NV center, and one directly above, by dwelling at each point for 7 seconds to ensure a mark is made. This time can be adjusted higher or lower

based on the available green power; however, too long of a dwell time can lead to stage drift which affects the accuracy of the alignment.

After a suitable number of candidate NV centers are marked and aligned, a discharge layer of AuPd is sputtered on top of the PMMA. The sample is then loaded in a dual beam scanning electron microscope and focused ion beam (SEM/FIB, Strata D235, FEI), taking care to securely ground the AuPd discharge layer to prevent drift during fabrication due to charging. The PMMA burn marks are located in the SEM, and a SIL is fabricated directly through the PMMA layer in a method similar to Ref. [86]. Following the fabrication, the PMMA and AuPd layer is removed by sonication in Microposit Remover 1165 (MicroChem). The gallium-implanted diamond layer left by FIB milling is removed by etching 80 nm of diamond using an Ar/Cl ICP/RIE etch (Trion Phantom ICP, Pressure: 10 mT, ICP: 400 W, RIE: 300 W, Ar: 12 sccm, Cl<sub>2</sub>: 20 sccm) [105]. The gallium-implanted diamond removal is not strictly necessary, although it significantly cuts down background fluorescence due to the surface and should be utilized for shallow SILs. Finally, the sample is cleaned in Nano-strip (Cyantek) at 70 °C for 20 min, followed by a soft-O<sub>2</sub> plasma clean for 15 minutes (Anatech SCE-108 Barrel Asher, RF power = 30 W) to remove any graphite layer and oxygen terminate the surface. Alignment is verified by imaging in the confocal set up. In our experiments, 5 out of 6 trials resulted in a successful alignment to the pre-determined NV center. The collection efficiency is improved by a factor of 6 and the excitation efficiency by a factor of 10 from saturation curve measurements.

This technique could be applied to the metalens design [82], although there are some complications. The metalens is typically designed for NVs greater than 10 μm in depth, thus obtaining an accurate measurement of the pre-selected NV depth is critical. Care must be taken to account for the different indices of refraction, which affect optical depth measurements [56], as well as spherical aberrations from the objective itself. However, these are manageable hurdles to overcome using standard microscopy techniques. Since the metalens is fabricated through electron beam lithography, an additional step between

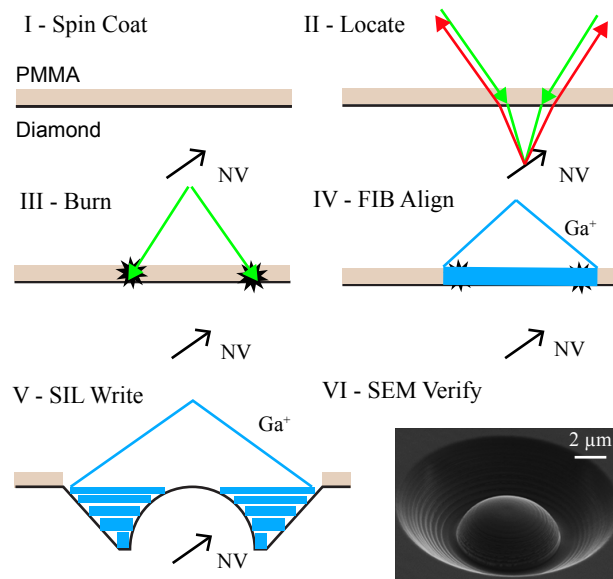


Figure 8: SIL Fabrication Process (I) Spin coat diamond with 500 nm of PMMA A8 to act as an *in situ* alignment medium. (II) Image NV centres to find suitable candidates ( $\sim 3 \mu\text{m}$  below surface) (III) Burn  $8 \mu\text{m}$  square marks centered on the NV ( $\sim 100 \text{ mW}$  of 532 nm) for 7 seconds to visibly indicate the NV location. (IV) Locate the markers in the FIB SEM, raster off the PMMA in the vicinity to be etched. (V) Etch the SIL using concentric circles of increasing depth. (VI) Verify the etch in the SEM and subsequently in the confocal microscope.

the PMMA burning and lithography alignment will have to be implemented. This may be possible by converting the PMMA burns to marks or metal deposited on the diamond surface with the FIB, which could in turn be used to align the electron beam apparatus.

## 4.2. Photolithography on Small Diamond Substrates

Fabricating lithographic wires within a few microns of NV centers allows for fast driving of the ground state spin and high-fidelity control pulses as discussed in § 2.3.2. Lithographic wires enabled Rabi driving rates as high as 500 MHz, surpassing the rotating-wave approximation regime and exploring new spin dynamics [54]. In addition to novel physics, fast control is necessary to reduce both hyperfine-induced and dephasing gate errors for many-pulse dynamical decoupling sequences [100, 160]. However, high-purity diamond substrates are orders of magnitude smaller than typical wafers used in nanofabrication facilities and developing fabrication processes for these diamonds proves to be challenging. Using a traditional photolithographic process, small chips produce large edge-beads and non-uniform resist coating, which limits the fidelity of the photolithographic process. Spray coating the resist can eliminate the edge bead, but leads to poor lift-off of the deposited metal layer. This section presents a fabrication process developed during my thesis which combines rapid mask prototyping with a bi-layer spray-coated resist process for metal lift off on diamond.

### 4.2.1. Required Equipment

The required tools and their purpose are as follows; An in-house mask writer (Heidelberg, DWL66+) to rapidly produce one-off masks; A resist spinner for laying down lift-off resist; A resist spray coater (Suss MicroTec, AS8 AltaSpray) which eliminates edgebeads and non-uniform resist; Lab-grade hot plate for baking resist and crystal bond; A mask aligner (Karl Suss, MA6 Mask Aligner) to visually align the custom mask to the diamond; A Metal evaporator (Kurt Lesker PVD75 E-beam/Thermal Evaporator) to deposit the required metal layers; and a heated water bath for liftoff.

#### 4.2.2. Fabrication Procedure

The general fabrication flow is depicted in Figure 9. Prior to the start of fabrication, the intended wire pattern should be converted to an appropriate file format (GDSII) and prepared for use on the Heidelberg mask writer (BEAMER). The pattern grid should be chosen to reflect which write head will be used. For SILs, typical dimensions are larger than 10  $\mu\text{m}$ , and thus the 10 mm write head offers suitable resolution (500 nm grid size). The pattern is converted to a photomask using the prescribed procedure maintained by the Singh center.

Once the mask is created, the diamond fabrication can begin. After cleaning the diamond with Nanostrip and an Acetoe-Isopropanol clean, the diamond should be mounted as close to the center of a 4" silicon wafer using Crystal bond (SPI Supplies, Crystalbond 509) [Fig. 10(a)]. Additional care should be made to ensure that the diamond is oriented properly to the flat edge of the wafer, which will ease alignment in the exposure step. To do this, the silicon wafer along with a small piece of Crystalbond is heated to  $> 120^\circ\text{C}$  to allow the Crystalbond to wet. Once wet, the diamond substrate is placed on the Crystalbond, with care being taken to ensure the diamond face is flat relative to the handle wafer. The bond is secure after a few minutes at room temperature.

Following the bonding, liftoff resist (LOR, MicroChem, LOR3A) is spun at 6000 rpm for 1 second, followed by 3500 rpm for 60 seconds. This should produce a nonuniform 300 nm thick LOR layer allowing for the eventual metal layer to liftoff cleanly. The LOR is then baked at  $150^\circ\text{C}$  to enhance the undercut rate, care is taken to not to disturb the diamond as the Crystalbond has re-wetted. After allowing the wafer to cool, 10  $\mu\text{m}$  of S1805 resist (MicroChem, S1805) is spray coated using the SussMicroTec AS8 AltaSpray. This amounts to four "passess" in the tool, which creates uniform resist coating. The resist is then allowed to rest for 10 minutes in a hood prior to exposure.

The handle wafer is then loaded into the mask aligner in top-side alignment mode.

This allows the diamond substrate to be viewed through the transparent regions of the mask, allowing for alignment to within a few microns of the intended SIL [Fig. 10(b)]. Once aligned, the resist is exposed with a dose of  $300 \mu\text{J}/\text{cm}^2$ . The resist is then developed in MF-321 for 40 seconds, followed by a 1 minute water bath. Following confirmation of the exposure and development in an optical microscope, the metal layer is deposited using a combined electron-beam and thermal evaporation tool. To ensure adhesion, a 10 nm Titanium layer is deposited at  $2 \text{ \AA s}^{-1}$  before depositing a 150 nm Gold layer at the same deposition rate. Following metal deposition, the handle wafer is submerged in 1165 (Dow, Microposit Remover 1165) in a  $60^\circ\text{C}$  water bath and shaken to lift off the resist. To help guarantee a successful lift-off, a pipette is used to gently circulate 1165 directly over the diamond. The lift-off also dissolves the Crystalbond and the diamond is removed from the handle wafer. Following this, a standard clean in Acetone then Isopropanol (both for 5 minutes) followed by forced Nitrogen drying is performed to clean the diamond surface of any remaining resist. The final device can be seen in Figures 10(c,d). The alignment-by-eye produces enough alignment tolerance ( $\sim 3 \mu\text{m}$ ) for the intended application, as the optical access to the SIL is preserved.

### 4.3. Multi-Color Imaging and Control of NV Centers

This thesis is centered on controlling and measuring three different properties of NV centers: the charge, orbital, and spin degrees of freedom. The frequency scales associated with these different degrees of freedom span from GHz to THz and appropriate sources of electromagnetic radiation are required. Furthermore, NV centers are randomly dispersed throughout a diamond and their optical identification is limited by the diffraction limit; a problem ideally suited for confocal microscopy. This section describes the design of a multi-excitation-color confocal microscope that has been used in this thesis and allows for the control and measurement of many of the NV's useful degrees of freedom.

Figure 11 depicts a schematic of the confocal microscope developed throughout the course of this thesis. The four excitation beams, described in Table 2, are co-aligned on

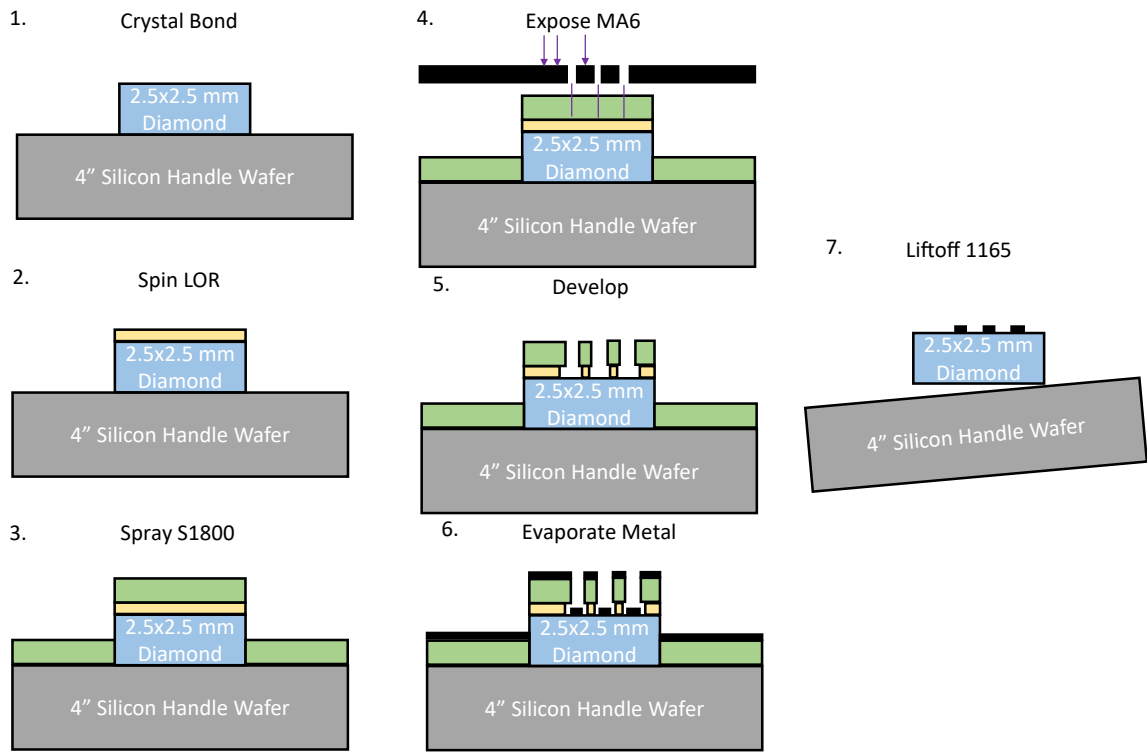


Figure 9: Photolithography and Liftoff on Diamond Substrates. (1) The diamond substrate is crystal bonded to the silicon handle wafer. (2) Liftoff Resist (LOR) is spun onto the diamond. (3) S1800 resist is spray coated to a thickness of 8-10  $\mu\text{m}$ . (4) The resist is exposed in a mask aligner, using the negative space to align to the SIL. (5) The resist is developed in MF-319 for 90 seconds. (6) Evaporate 10 nm of titanium and 150 nm of gold. (7) Lift off resist and crystal bond in 1165 Remover at 60  $^{\circ}\text{C}$ .

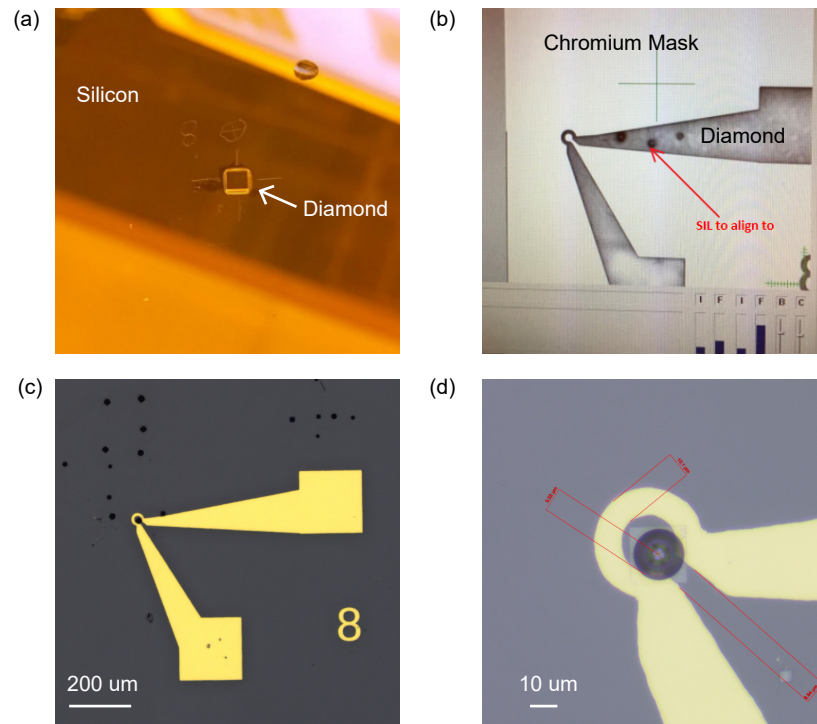


Figure 10: Fabrication of Lithographic Wires on Diamond. (a) Photograph of the diamond crystal bonded to the silicon handle wafer. Scratches on the wafer indicate the wafer center and orientation of the diamond substrate. (b) Photograph of the MA6 Mask Aligner alignment camera image depicting how the negative space on the mask is used to align the SIL to the pattern on the mask. (c) Optical micrograph (10x) of the completed device on the diamond substrate. (d) Magnified optical micrograph (50x) of the wire loop around the SIL, demonstrating that the alignment preserves optical access to the SIL.

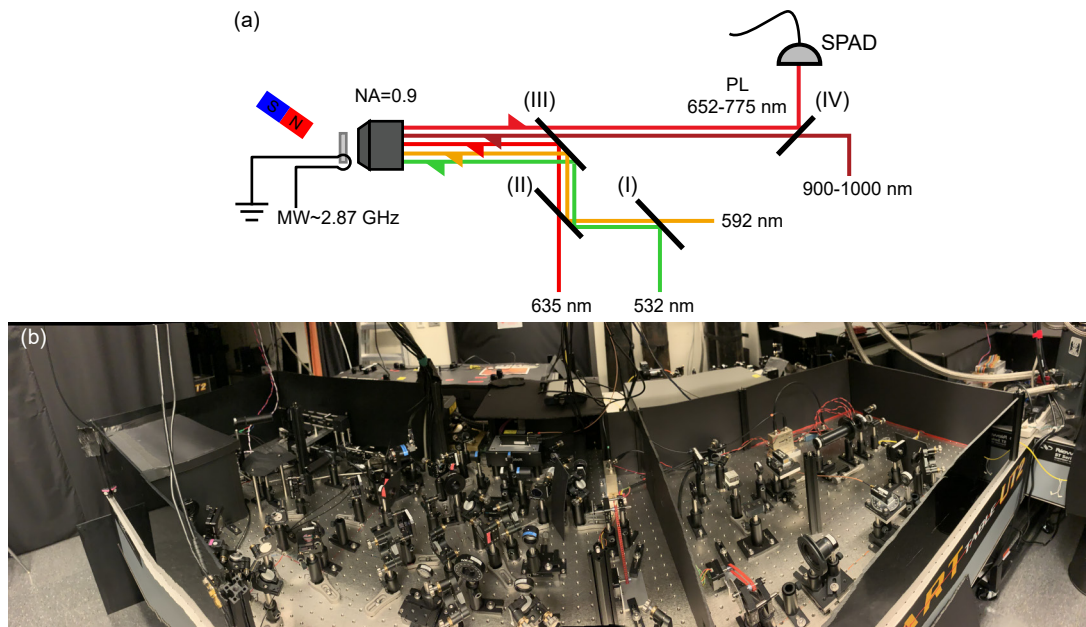


Figure 11: Multi-Color Confocal Microscopy of NV centers. (a) Four different lasers can independently illuminate the NV center while maintaining a  $N^-$  selective collection band. The visible wavelengths are combined using two dichroics (I and II) while a third dichroic (III) is used to split the visible excitation band from the red-shifted phonon sideband (PSB) fluorescence of  $NV^-$ . A dichroic in the collection path (IV) is used to separate the collected PSB fluorescence from any near infrared excitation. All lasers and the radiofrequency (RF) source can be amplitude-modulated via the timing electronics for time-domain control with tens of nanoseconds of precision. A single-photon avalanche diode (SPAD) converts the PSB fluorescence to electrical signals. See the text for manufacturers and part numbers. (b) Photograph of the microscope.

their respective dichroics, described in Table 3, reflected off a fast steering mirror (Optics in Motion, OIM101), and imaged onto the back of an NA=0.9 objective (Olympus, MPLANFLN 100x) using a  $4f$  lens configuration. The collected PL path has 635 nm longpass (Semrock, BLP01-P01-635R) and 775 nm shortpass (Semrock, FF01-775/SP-25) filters to prevent excitation light from reaching the detector. Collected and filtered PL light is focused onto a 1 m-long, 50  $\mu\text{m}$ -diameter-core multi-mode optical fiber, (Thorlabs, MF42L01) with a 150 mm achromatic lens (Thorlabs, AC254-150-B) that has an anti-reflection coating for 650-1100 nm. The multi-mode fiber acts as the pinhole and the objective, however the confocal condition is relaxed in this setting due to the relatively low background of high-purity diamond samples. The multi-mode fiber is attached to a fiber-coupled single-photon avalanche diode (SPAD, Laser Components, Count-20C-FC) with high efficiency (70% @ 670 nm) and low dark counts (20 Cts  $\text{s}^{-1}$ ). An amplitude-modulated (MiniCircuits, ZASWA-2-50DR) signal generator (Stanford Research Systems, SG384) is sent through a high-power, wide-band amplifier (MiniCircuits, ZHL-16W-43-S+) and acts as the radiofrequency source for spin control. The phase of the carrier signal is modulated at the signal generator with 10 MHz bandwidth. The output of the amplifier is then sent to the sample, which could be a lithographically defined wire or a bond wire strung across a sample.

A few considerations should be made when designing a comparable optical system. The first is that minimizing the number of dichroics in the collection path helps increase the collection efficiency and reduces the laser-power-loss. This is especially true for the near infrared laser, as only certain dichroics extend their transparency window out to 1000 nm. Another key aspect to consider is the stability of the setup. Small temperature fluctuations and mechanical disturbances to the optical table can disturb the five unique optical paths that are co-aligned on the fast steering mirror and objective. To alleviate some (but not all) of these issues, one should take care to minimize the independent path-length of all of the lasers.

The electronic components of the microscope is comprised of the photon counting and

Wavelength	Mode	Modulation	Part No.	Physical Use
532 nm	CW	Digital AOM	Laser Quantum, Gem 532	NV <sup>-</sup> charge and spin initialization, spin readout
592 nm	CW	Digital AOM	MPB Communications, VFL-592	Charge Readout, SCC shelf and ionization
635 nm	CW	Analog Diode Current	Cobolt, MLD-06-01 638	Charge readout and SCC ionization
900-1000 nm	Pulsed, 10 ps	Triggered Supercontinuum	Fianium, White-Lase SC-400	Near infrared charge control and SCC ionization

Table 2: Electromagnetic sources used throughout this thesis.

Number	Cut-on	Mfgr. / Part No.
I	568 nm	Semrock, FF568-Di01-25D
II	594 nm	Semrock, Di02-R594-25x36
III	662 nm	Semrock, FF662-FDi01-25D
IV	800 nm	Edmund Optics, 69-872

Table 3: Dichroic beam splitters depicted in Figure 11.

timing modules. The photon counting consists of a data acquisition device (DAQ, National Instruments, DAQ6323) or a field programmable gate array (FPGA, Xilinx, Artix-7) which count the rising edges produced by the SPAD. The output of the SPAD can also be routed through multiple fast switches (MiniCircuits, ZYSWA-2-50DR) which allows for the routing of the signal to up to four independent counters. The timing electronics consist of an arbitrary waveform generator (AWG, Tektronix, AWG520 Digital Out Option 03) which controls one 10-bit analog channel, 4 digital markers, and 10 digital channels. Each channel is synchronized with a sample clock of  $1\text{ GS s}^{-1}$ . The data is prepared point-wise (each channel has a defined value for every clock cycle), and can be played out continuously repeating the data, only playing after a trigger, or implement basic triggered logic using the event table.

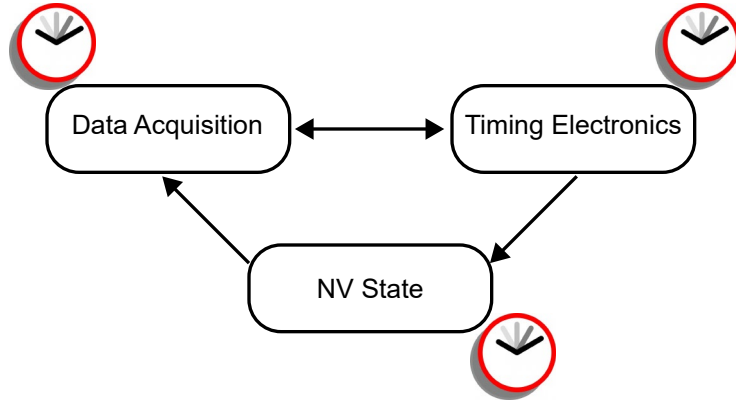


Figure 12: Clock Sources for Data Acquisition. Schematic of typical NV center experiments and available clock sources. The data acquisition and timing electronics clocks are fixed frequency, or synchronous, whereas the clock based on the NV state is variable due to the stochastic nature of the state.

#### 4.4. Data Acquisition

Almost all of the experiments performed on NV centers require time-domain control of the optical, charge, and spin properties. Common experiments involve changing the widths of optical or RF pulses and changing timing delays between these pulses. A master clock is usually designated to signify the completion of a measurement and trigger data collection. A schematic of the various subsystems of typical experiments that can act as the master clock can be seen in Figure 12. The subsystems of data acquisition (National Instruments, DAQ6323), timing electronics (Tektronix, AWG520), and NV state (diamond device and real-time logic) all play critical roles in the experiment but have different clocking behavior and must be integrated. In addition, care must be taken to avoid low frequency noise sources such as stage drift, laser power fluctuations, and collection optics drift. These noise sources result in long-time scale correlated noise in measurements, potentially contributing to systematic errors in the observed measurement. This section will discuss strategies for selecting the master clock and integrating the other systems together with an eye towards reducing systematic noise and increasing data collection speed.

#### *4.4.1. Serial vs. Interleaved Trial Ordering*

Since NV center experiments need to be repeated tens to hundreds of thousands of times to overcome shot noise, the ordering of when these repeats are played out can significantly affect the influence of low frequency noise. For example, consider a measurement that requires 50,000 repeats, each taking 500  $\mu\text{s}$ , of 10 different timing variables, referred to as trials, in order to achieve the desired SNR. The total acquisition time for this is 250 seconds and is thus susceptible to mechanical drift and laser power fluctuations. The first, and simplest, acquisition strategy is to use the timing electronics system as the master clock with the data acquisition simply recording the total number of photon counts in a desired time bin, and each trial is recorded for 25 seconds. The average signal of the first trial could be as large as 10-15% different than the signal from the 10<sup>th</sup> trial due to the aforementioned laser power and alignment drift, introducing an artifact in the data set. A first-attempt at correcting this is to shorten the trial acquisitions and take multiple “sweeps”, randomizing when each trial was acquired. However, this only removes systematic noise and is still susceptible to the random noise present.

A better strategy is to interleave the averaging. This is performed by transitioning the master clock to the data acquisition. The clock signal triggers the timing electronics to output the first trial, and the data acquisition records the result (typically whether a photon was detected or not). The following clock signal triggers the timing electronics to output the second trial, and the data is recorded once again. After the 10<sup>th</sup> trial, the timing electronics loops back to the first trial and begins again, repeating this entire process 50,000 times. At the end of this acquisition, any time-correlated noise affecting the measurement has been evenly distributed across all of the data, eliminating most artifacts from noise in the observed data.

#### 4.4.2. *Fixed-Frequency vs. Chirped Data Acquisition*

The clock period generated by the data acquisition system usually must be fixed, leading to a single frequency of data recording. This is due to the specific data acquisition system (DAQ) used in this thesis (DAQ6323), which can only run the counter subsystem (for counting photon detections) when the clock rate is well defined. To ensure that each trial is played out to its full extent, the clock period is set by the longest trial, and all shorter trials have dead time in which they are waiting until the next trigger. When each trial has comparable durations, there is minimal dead time and synchronous acquisition is suitable. However, certain NV spin and charge measurements can have variable delays spanning over three orders of magnitude between  $\mu\text{s}$  to  $\text{ms}$ . In addition, these long delay measurements are also the most susceptible to low frequency noise, so maintaining the ability to interleave the trials is critical.

A solution to reducing the overhead is to run the data acquisition in a triggered mode, in which it samples some number of digital bits at each measurement, and use the timing electronics as the master clock which will vary the period of the data recording signal for each trial, resulting in a chirped frequency of data recording. One more component must be added to the experiment, namely a real-time logic device which is capable of converting the number of detected photons and the corresponding trial number into digital signals, these digital signals are sampled by the DAQ and allow for the data stream to be re-assembled in post-processing. This can be implemented with a field-programmable gate-array (FPGA). This strategy, while requiring significant hand-shaking between three differently clocked electronics, provides the most noise resilient and fastest data acquisition for a host of experiments. In addition, this chirped frequency data acquisition can allow for a stochastically varying data recording frequency, which is necessary to utilize the NV state as a clock source. The clock is then governed by when the setup determined the NV to be in a chosen state prior to beginning a measurement. Both of these chirped data acquisition techniques were pivotal to the experiments discussed in Chapter 7.

## CHAPTER 5 : Singlet Based Spin-to-Charge Conversion

This chapter, along with supplemental material, was published previously in *Physical Review B* [78]. Reprinted article with permission from D. A. Hopper et al. “Near-infrared-assisted charge control and spin readout of the nitrogen-vacancy center in diamond” *Physical Review B* 94, 241201(R) 2016. Copyright 2016 by the American Physical Society. The experiments and analysis of this chapter were completed with the help of Dr. Richard Grote and Dr. Annemarie Exarhos.

### 5.1. Introduction

The diamond nitrogen-vacancy (NV) center is a versatile solid-state qubit [10] and nanoscale sensor [94, 111], exhibiting long spin coherence times at room temperature and all-optical mechanisms for qubit initialization and readout. Unfortunately, these convenient mechanisms are imperfect. The NV’s intrinsic optical dynamics limit the charge and spin initialization purity well below unity [8, 137, 171, 172] and only provide a low-fidelity spin-state readout [91, 111, 161]. These drawbacks impose substantial averaging requirements that diminish the full potential of the NV center as a qubit and quantum sensor [41].

Initialization and readout of NV spins are traditionally achieved through optical excitation and photoluminescence (PL) detection, respectively. Optical excitation, however, causes unavoidable cycling from the desired negative charge state ( $NV^-$ ) into the neutral state ( $NV^0$ ) with a different spin and orbital configuration. Charge-state transitions result from optical excitation of an electron from  $NV^-$  to the conduction band (ionization) and a hole from  $NV^0$  to the valence band (recombination), which compete to produce a maximum steady-state  $NV^-$  population of  $\sim 75\%$  using an optimized single excitation wavelength of 532 nm [8].

Traditional PL-based spin readout results from a spin-dependent inter-system crossing (ISC) between the triplet and singlet manifolds of  $NV^-$  [44, 137, 167]. In typical

experiments, PL contrast only exists for the first  $\sim 200$  ns of excitation, during which time  $\sim 0.01$  PL photons are collected, on average. Therefore  $\sim 10^4$  repeats are required to obtain adequate signal-to-noise ratio (SNR). This averaging requirement precludes important applications including projective [132] and partial [18] measurements of proximal nuclear spins, as well as verification of entanglement between remote NVs [16], all of which rely on a single-shot electron readout protocol that, at present, is only available at cryogenic temperatures [137].

Here, we demonstrate dramatic improvements in both charge initialization and spin readout fidelity by using multicolor illumination to manipulate the NV's orbital, spin, and charge-state dynamics. Our experiments uncover complex multiphoton absorption effects driven by visible and near-infrared excitation, resolving conflicting reports of both enhancement and quenching of  $NV^-$  PL under simultaneous illumination with 532 nm visible and 1064 nm light [59, 90, 103, 123]. We use this knowledge to demonstrate a new protocol for efficient spin-to-charge conversion *via* selective ionization of the  $NV^-$  singlet that yields a 6-fold increase in the signal-to-noise ratio (SNR) for single-shot spin measurements and a pathway towards single-shot electron spin readout at room temperature.

Recent attempts to overcome the charge initialization problem include electrical gating [47] and doping [46], but the former yields deterministic initialization only in  $NV^0$  and the latter, while effective in stabilizing  $NV^-$ , also introduces impurities that reduce the spin coherence time. Several schemes have been proposed to address the readout problem. Protocols using quantum logic with nuclear spin ancillae [91, 156] have achieved a 7-fold improvement in SNR over traditional PL measurements [111], at the expense of demanding technical and material requirements. An alternative approach was explored by Shields *et al.* [150], who demonstrated spin-to-charge conversion (SCC) through spin-dependent ionization of the  $NV^-$  triplet manifold using a visible pulse of light. Together with high-fidelity readout of the NV charge state [172] and extremely high photon collection efficiency, SCC yielded a 4-fold improvement in the single-shot SNR and reduced the spin readout noise

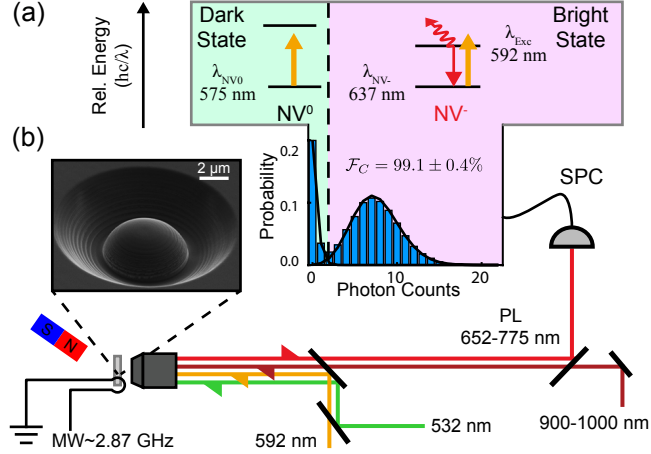


Figure 13: Deterministic Charge State Readout of the NV Center. (a) Illumination at 592 nm selectively excites the  $NV^-$  charge state (ZPL at 637 nm) and not  $NV^0$  (ZPL at 575 nm). A typical photon distribution for a 3 ms readout duration is inset below (5000 cycles). (b) Diagram of the confocal microscope and electron micrograph of the solid immersion lens milled by a focused ion beam from the diamond surface. (ZPL: Zero-phonon line, MW: Microwave, SPC: Single Photon Counter).

to  $\sim 3\times$  the standard quantum limit (SQL). Nonetheless, a room-temperature protocol for single-shot electron-spin readout with  $SNR > 1$  is still lacking.

## 5.2. Results

Figure 13 illustrates the experimental setup and the concept of high-fidelity charge readout. The technique exploits the blue-shifted absorption spectrum of  $NV^0$  compared to  $NV^-$ , allowing for charge-dependent PL during 592 nm excitation. Precise tuning of the illumination power ( $\sim 100$  nW) and readout time produces a strong PL contrast ( $SNR \approx 3$ ) that allows for single-shot discrimination of the two charge states by introducing a photon-detection threshold condition (dashed black line in Fig. 13a). For low illumination power, the single-shot charge measurement is also non-destructive, which facilitates deterministic monitoring of the charge dynamics and the direct measurement of ionization and recombination rates from individual charge-transition events [8]. The photon-detection histogram shown in the inset of Fig. 13a corresponds to a single-shot fidelity  $\mathcal{F}_c = 99.1 \pm 0.4\%$  and a non-destructivity exceeding 96% [78].

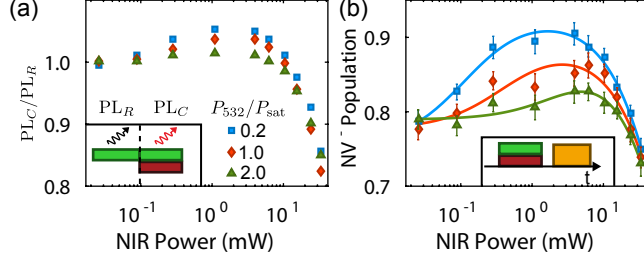


Figure 14: Multi-Color Modulation of Steady-State PL and Charge. (a) PL due to coincident excitation at 532 nm and 900-1000 nm ( $PL_C$ ), normalized by the reference PL level under 532 nm excitation alone ( $PL_R$ ). The NIR excitation is modulated with a square wave at 5 kHz (inset). Experimental uncertainties are smaller than the symbols. (b) Steady-state population of  $NV^-$  (points) for the corresponding power combinations in (a), fit using a model described in the text (curves).

Individual NVs are addressed using a home-built scanning confocal microscope with three excitation sources (Fig. 13b). Continuous-wave 532 nm and 592 nm lasers are gated with acousto-optic modulators, and a 900-1000 nm band-pass-filtered supercontinuum source (hereafter termed NIR) produces picosecond pulses with a 40 MHz repetition rate that can be gated in time. A 6- $\mu\text{m}$ -diameter solid immersion lens is fabricated around a preselected NV to increase the collection and excitation efficiency using an *in-situ* alignment technique and focused-ion-beam milling. Collected PL is filtered to select for  $NV^-$  in the 650-775 nm band and detected with a single-photon avalanche diode. In this configuration, we record  $\sim 0.04$  PL photons per 200 ns shot [78]. A  $\sim 20$  G magnetic field applied along the NV's symmetry axis splits the  $NV^-$  ground-state  $m_s = \pm 1$  spin sublevels, and a 20  $\mu\text{m}$ -diameter gold wire placed across the surface of the diamond is driven by pulsed microwaves to control the ground-state spin.

Figure 14 presents measurements of the steady-state PL and corresponding charge distribution under coincident excitation with 532 nm and NIR light. Both sets of measurements exhibit non-monotonic variations as a function of NIR power,  $P_{\text{NIR}}$ , connecting conflicting observations of PL quenching and enhancement in different regimes [59, 90, 123]. The direct correlation between the relative changes in PL (Fig. 14a) and the underlying charge distributions probed using single-shot readout (Fig. 14b) confirm the hypothesized role of

charge-state modulation in these effects. Overall, the non-monotonic response and dependence on green power ( $P_{532}$ ) hint at multiple processes that depend on the relative visible and NIR intensities. Below, we explore the role of NIR light in modulating the NV's charge dynamics in these different regimes.

Notably, the PL enhancement observed with modest green and NIR powers in Fig. 14a is accompanied by an increase in the steady-state  $NV^-$  population ( $p_{\text{minus}}$ ) to a maximum value of  $91 \pm 0.6\%$ , corresponding to an 18% improvement over the observed population under 532 nm illumination of 77%. This is, to our knowledge, the highest-purity all-optical initialization of  $NV^-$  yet reported. Furthermore, we anticipate that the spin purity should be maintained under this protocol since the spin-polarization rate exceeds the charge-switching rate in this regime by over two orders of magnitude [29].

Figure 15a uses a linear horizontal scale to present the same data as Fig. 14b (lowest green power) together with an analogous measurement combining 592 nm and NIR excitation. We observe an initial enhancement followed by suppression of  $p_{\text{minus}}$  in both cases, which implies this behavior is independent of the vastly different initial conditions produced by 532 nm and 592 nm light alone [8]. In contrast, the charge distributions observed in a similar experiment using only NIR light (red triangles in Fig. 15a) exhibit completely different dynamics, underscoring the crucial role of coupled, nonlinear optical processes.

To elucidate the underlying mechanisms, we use high-fidelity, non-destructive charge-state readout to directly measure the NV's ionization and recombination rates. After non-destructively determining the charge state, we apply an optical pulse with duration and intensity chosen to induce  $\ll 1$  charge transition, and then measure the resulting state. Following many such measurements, the rates are calculated from the corresponding transition probabilities divided by the illumination duration.

Figure 15b shows the ionization and recombination rates as a function of  $P_{\text{NIR}}$  in the regime of  $NV^-$  enhancement ( $P_{532}$  is slightly lower than in Fig. 15a to reduce the charge-

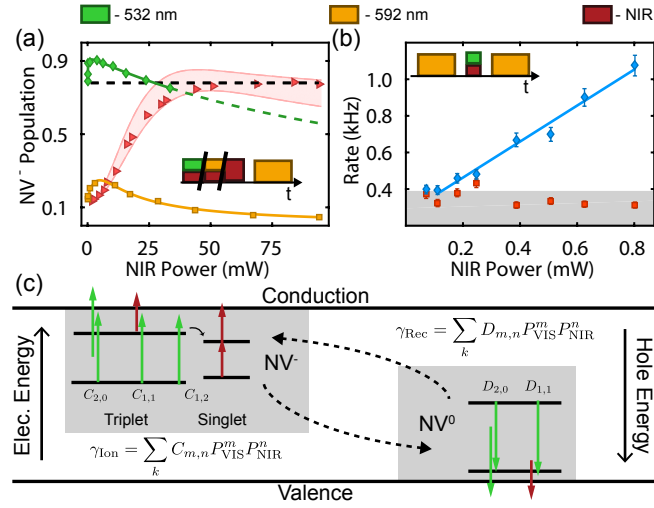


Figure 15: Charge Dynamics Driven by Multiphoton Absorption. (a) NV<sup>-</sup> population versus  $P_{\text{NIR}}$ , for fixed visible excitation at 532 nm ( $9 \mu\text{W} \simeq 0.2 P_{\text{sat}}$ ,  $\blacklozenge$ ), 592 nm ( $20 \mu\text{W} \simeq 0.1 P_{\text{sat}}$ ,  $\blacksquare$ ), and for NIR light only ( $\blacktriangleright$ ). Curves are fits described in the text. The shaded region indicates the 95% confidence interval for a simulation of the NIR data using separately measured rates [78]. (b) Recombination ( $\blacklozenge$ ) and ionization ( $\blacksquare$ ) rates versus  $P_{\text{NIR}}$  for  $P_{532} = 5.4 \mu\text{W} \simeq 0.13 P_{\text{sat}}$ . The shaded region indicates the noise floor. (c) NV energy diagram indicating allowed optical transitions and corresponding coefficients in the rate model. Insets in (a-b) depict the experimental pulse sequences for each measurement. Except where indicated by error bars, symbol sizes exceed the experimental uncertainty.

switching rates due to green light alone, but the steady-state maximum  $p_{\text{minus}} = 91\%$  is unchanged). As expected, the rate for recombination is much larger than for ionization; in fact, the ionization rate is below the noise floor imposed by the 4% destructivity of the charge verification step.

The recombination rate’s linear dependence on  $P_{\text{NIR}}$  implies that the mechanism driving  $\text{NV}^-$  enhancement involves a single NIR photon. The most likely candidate is a sequential absorption process in which a 532 nm photon promotes a hole to the excited state of  $\text{NV}^0$ , followed by the absorption of single NIR photon to promote the hole into the valence band, thus converting the center to  $\text{NV}^-$ . Based on the location of the NV’s levels within the bandgap [8], an analogous ionization process is also allowed, but it is apparently  $\sim 7$  times less likely to occur [78]. This asymmetry could result from a combination of the  $\sim 50\%$  longer optical lifetime of  $\text{NV}^0$  [106] and different cross sections for NIR absorption by the  $\text{NV}^-$  and  $\text{NV}^0$  excited states. We have also measured the ionization and recombination rates in the presence of NIR light alone [78]. They scale with  $P_{\text{NIR}}^3$  and  $P_{\text{NIR}}^2$ , respectively, but are several orders of magnitude smaller than the corresponding rates in the presence of visible light.

To capture the effects of these competing nonlinear processes, we employ a master-equation model for the charge-state dynamics, schematically depicted in Fig. 15c. It includes the allowed orbital and charge transitions considering six levels that comprise the  $\text{NV}^-$  triplet and singlet manifolds, and the  $\text{NV}^0$  ground and excited states. Each ionization or recombination process is assigned a coefficient,  $C_{m,n}$  or  $D_{m,n}$ , respectively, where  $m$  and  $n$  are the respective number of visible and NIR photons required for that process. For example, the ionization rate for the process corresponding to  $C_{m,n}$  is given by  $C_{m,n} P_{\text{VIS}}^m P_{\text{NIR}}^n$ . The total ionization or recombination rate is the sum of all the individual rates.

We apply this model to fit the steady-state charge distributions in Fig. 15a, using four parameters that quantify the relative weights between the ionization/recombination coefficients (see Appendix E for more details). Differences between the experiments using

532 nm and 592 nm light are naturally explained by large differences in the cross section for  $NV^0$  excitation that affect  $D_{1,1}$  and  $D_{2,0}$ . The charge distributions observed under NIR-only illumination in Fig. 15a do not, in fact, represent the steady-state population, due to the relative weakness of NIR-only nonlinear absorption. Nonetheless, we can quantitatively reproduce those data by adapting our model to account for the slow underlying rates (<kHz) and a partially destructive charge-state readout [78].

Whereas the  $NV^-$  enhancement observed at low powers in Fig. 15a is driven by the asymmetry in  $D_{1,1}/C_{1,1}$ , the suppression at increasing powers results from the higher-order term  $C_{1,2}$ . This process corresponds to ionization of  $NV^-$  *via* absorption of one visible and two NIR photons. A candidate mechanism is NIR-induced ionization from the metastable singlet ground state. The singlet manifold is populated through the ISC by visible excitation, and exhibits a zero phonon line at 1042 nm accompanied by a broad phonon-assisted-absorption sideband overlapping our NIR excitation source [2, 96].

To confirm the singlet’s role in quenching  $NV^-$  at high  $P_{\text{NIR}}$ , we use the generalized measurement sequence depicted in Fig. 16a to probe the time-domain ionization dynamics. Since we are interested in  $NV^-$  as a starting state, we use a non-destructive charge-verification step to provide a high-purity, post-selected  $p_{\text{minus}} = 96.8 \pm 0.4\%$ . The effects of an arbitrary sequence of visible, NIR, and microwave pulses on the NV’s charge are then measured using a high-fidelity readout step. In Fig. 16b, we initialize the ground-state spin in either the  $m_s = -1$  or  $m_s = 0$  sublevel before applying a varying-duration 532 nm shelving pulse followed by a 400 ns, 95 mW train of NIR pulses. The resulting spin-dependent contrast in the final  $NV^-$  population is the hallmark of SCC, and the preferential ionization of  $m_s = -1$  over  $m_s = 0$  suggests that the singlet population is being ionized. To confirm this hypothesis, we fix the shelving pulse duration at  $\tau_s = 200$  ns to produce a maximum charge contrast, initialize into  $m_s = -1$ , and vary the delay,  $\tau_d$ , to the 400 ns NIR pulse train (Fig. 16c). The resulting  $p_{\text{minus}}$  exhibits exponential decay with a timescale commensurate with the metastable singlet’s lifetime ( $\tau_{\text{Fit}} = 182 \pm 10$  ns) [2, 137].

The transient population of the  $NV^-$  singlet manifold is highly spin dependent. Therefore, singlet-selective ionization provides a promising means for SCC. The maximum SCC contrast observed in Fig. 16(b) ( $\sim 7\%$  for  $\tau_s = 200$  ns) is limited in our current setup by the available NIR pulse energy (2 nJ), which ionizes the singlet with per-pulse probability  $\sim 6\%$ . The full NIR pulse train ionizes the singlet with 32% probability [78]. Despite this incomplete ionization, we can enhance the SCC efficiency substantially by repeating the shelve-ionize pulse sequence  $N$  times (Fig. 16d). Crucial to this multi-SCC method is the choice of a shelving pulse that excites the triplet manifold once on average, which we found to occur when  $\tau_s = 30$  ns with a power near saturation. The spin contrast increases rapidly with  $N$  to  $\sim 25\%$  and eventually saturates due to a combination of effects including incomplete ionization, accidental ionization of the triplet, the small ISC probability for  $m_s = 0$ , and imperfect spin initialization. Fits to the data in Fig. 16d reflect an extended six-level master-equation model that accounts for all these factors (see Appendix F).

### 5.3. Discussion

To quantify the performance of multi-SCC spin readout, we consider the single-shot SNR corresponding to a measurement of the spin contrast, i.e., the difference between a spin prepared in  $m_s = 0$  and  $\pm 1$  (Fig. 16e). The noise includes contributions from both imperfect SCC efficiency and shot noise in the charge-state readout [78]. Our demonstrated protocol exhibits a single-shot SNR = 0.32, corresponding to a spin-readout noise  $4.6\times$  the SQL and constituting a 6-fold improvement over traditional PL readout, even for our SIL-enhanced device [78]. Given NIR pulses that ionize the singlet with 100% probability, we predict a further  $\sim 2.6$ -fold improvement to SNR = 0.83, corresponding to a single-shot readout fidelity exceeding 75% and spin-projection noise  $1.9\times$  the SQL. The singlet-selective ionization can be optimized by adjusting the wavelength, pulse width, and repetition rate of the NIR pulse train to compensate the singlet's small optical cross section and short excited-state lifetime ( $\sim 1$  ns) [2], and with the use of cavities to boost the optical interaction. These values all include the detrimental effect of imperfect spin initialization (we infer  $\sim 85\%$  spin purity).

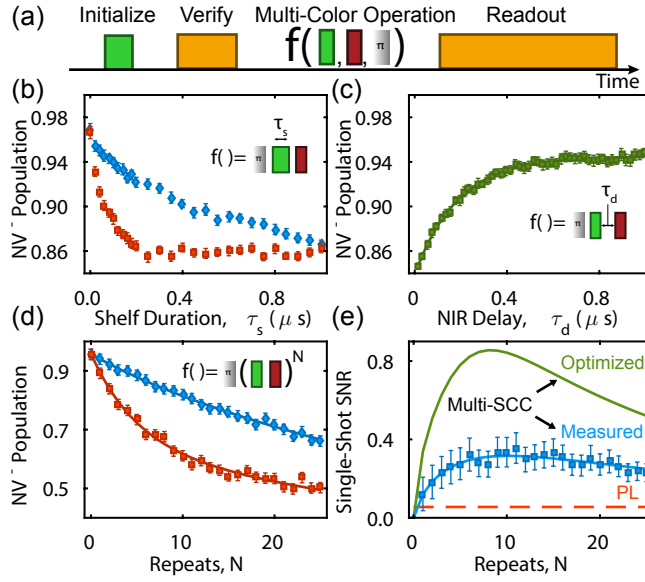


Figure 16: Spin-to-Charge Conversion *via* Singlet Ionization. (a) Generalized pulse diagram for probing time-domain charge dynamics. (b) Resulting charge state as a function of 532 nm shelf duration followed by a 400 ns NIR pulse for spins prepared in  $m_s = 0$  ( $\diamond$ ) and  $m_s = -1$  ( $\blacksquare$ ). (c) Resulting charge state as a function of the delay between a 200 ns, 532 nm shelving pulse and a 400 ns NIR pulse, for a spin prepared in  $m_s = -1$ . (d) Final charge state as a function of SCC repeats for different initial spin states prepared as in (b). (e) Spin-readout SNR comparison of traditional PL (red), measured multi-SCC (blue), and the optimized multi-SCC protocol assuming 100% singlet ionization (green).

With improved spin purity, multi-SCC should approach a maximum SNR $\sim$ 1.9, limited by the intrinsic  $\sim$ 10:1 spin-dependent ISC branching ratio[60]. This ideal case corresponds to an upper bound of the single-shot spin readout fidelity of 90%.

#### 5.4. Conclusion

In conclusion, we use previously unexplored multi-photon absorption mechanisms to improve both initialization and readout of diamond NV spins. Deliberate tuning of coincident 532 nm and NIR intensities boosts the steady-state NV<sup>-</sup> population to  $91.0 \pm 0.6\%$ . Carefully timed optical pulse sequences generate efficient spin-to-charge conversion and a universal spin-readout enhancement over the standard approach. Crucially, these all-optical techniques are applicable to both single-NV and ensemble experiments where high-contrast charge measurements have recently been demonstrated [40, 88]. Furthermore, these enhancements can lead to significant advances for many research avenues including magnetometry [111] and operations involving nuclear spins [100, 160], where signal averaging is a critical bottleneck. Future experiments exploring the SCC dynamics and performance in ensembles as well as nanodiamonds will further motivate the adoption of these enhanced spin readout techniques for diverse applications. Ultimately, as the SCC efficiency approaches the ideal limit of single-shot electron spin readout, it will enable room-temperature applications of protocols that were previously relegated to cryogenic (<10 K) temperatures, including projective and partial measurements of nuclear spins [18, 132] and verification of multi-spin entanglement [16].

## CHAPTER 6 : Spin-to-Charge Conversion in Nanodiamonds

This chapter, along with supplemental material, was published previously in *ACS Nano* [79]. Reproduced with permission from D. A. Hopper et al. “Amplified Sensitivity of Nitrogen-Vacancy Spins in Nanodiamonds Using All-Optical Charge Readout” *ACS Nano* 12, 5, 4678-4686 2018. Copyright 2018 American Chemical Society. The experiments and analysis of this chapter were completed with the help of Dr. Richard Grote and Samuel Parks.

### 6.1. Introduction

Nitrogen-vacancy (NV) centers embedded in nanodiamonds combine the advantages of an optically-addressable, room-temperature spin qubit [10] with the nanoscale dimensions and flexible surface chemistry of diamond nanoparticles [121, 146]. Recent proof of concept demonstrations of their quantum sensing capabilities include magnetic [104] and thermal [101] imaging in living cells; detection of electrochemical potentials [63, 94, 131], paramagnetic molecules [157, 163], and pH levels [136] in solution; and investigations of ferromagnetism on the nanoscale [3, 129, 143, 164]. All of these sensing modalities demand strong interactions between NV qubits and a target environment outside the diamond, for which nanoparticles are ideal. However, high impurity levels and uncontrolled surface states in nanodiamonds [28, 36] degrade the NV’s spin and charge stability compared to the situation in bulk diamond [158], leading to signal averaging issues and limited sensitivity for nanodiamonds due to poor optical contrast for charge [94] and spin [20] readout by photoluminescence (PL) techniques.

In conventional PL-based spin readout, an intense 532 nm probe produces slightly more PL photons for the NV’s  $m_s = 0$  ground-state spin sublevel as compared to  $m_s = \pm 1$  for the first  $\approx 300$  ns of illumination. However, recently established spin-to-charge conversion (SCC) protocols offer a more flexible approach [78, 150]. SCC utilizes the intersystem crossing dynamics of the  $NV^-$  excited state to protect one spin state from an intense

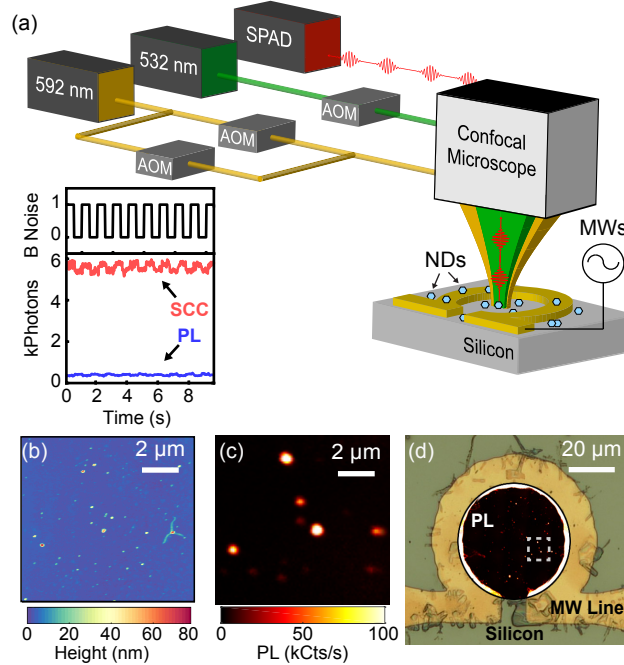


Figure 17: Charge and Spin Control of Individual Nanodiamonds (a) Experimental set-up consisting of a two-color home-built confocal microscope imaging nanodiamonds dispersed on a microwave antenna device fabricated on silicon (SPAD, single-photon avalanche diode; AOM, acousto-optic modulator; NDs, nanodiamonds; MWs, microwaves). Inset: Experimental demonstration of a  $T_1$  spin relaxometry measurement using PL (blue) and SCC (red) depicting the SNR amplification for a nanodiamond agglomerate. Atomic force microscope measurements (b) and PL images (c) of the region boxed in (d) indicate the presence of individual nanodiamonds.

ionization pulse, leading to a spin-dependent charge distribution. A subsequent charge-selective optical pulse detects the resulting distribution, with the potential for dynamical tuning of power and duration for optimum efficiency [35].

Here, we present all-optical protocols for high-contrast charge readout and SCC of NV ensembles in nanodiamonds as a means for boosting the signal-to-noise ratio (SNR) for charge and spin measurements as compared to conventional PL techniques, as seen in Fig. 17(a). An investigation of the optically induced charge dynamics suggests that NVs in nanodiamonds milled from type Ib high-pressure, high-temperature (HPHT) diamond are prone to multiple non-radiative ionization (negative to neutral) and recombination (neutral to negative) pathways that are not observed in bulk, type IIa diamond. We attribute

these dynamics to tunneling transitions involving nearby impurity sites. Despite these complications, we confirm on a sample of 38 individual nanodiamonds and several larger nanodiamond ensembles that our proposed high-contrast charge readout and SCC protocols, which differ from those demonstrated in high-purity bulk diamond [78, 150], can be efficiently utilized for quantum sensing protocols.

For single NVs in bulk, type IIa diamond, strong charge-dependent optical contrasts facilitate high-fidelity, single-shot measurements of the NV's charge state [8, 78, 172]. These measurements rely on the large energy difference in the zero phonon lines of the neutral charge state ( $NV^0$ , 2.156 eV) and the negative charge state ( $NV^-$ , 1.945 eV) as well as the fact that the ionization and recombination mechanisms are two-photon processes [171]. Recently, charge readout has been extended to ensembles of NVs in type Ib bulk diamond [40, 88], which is typically used to produce nanodiamonds with NV centers [28, 36]. Charge dynamics in bulk type Ib diamond are complicated by impurity-related charge transfer mechanisms [88, 113], and the situation in nanodiamonds is even less well understood. A few studies have aimed to maximize the  $NV^-$  population under continuous illumination [17, 74, 141] or to measure charge-dependent stimuli using nanodiamonds [94, 131]. Improved charge readout techniques could vastly improve the sensitivity of such measurements.

High-contrast charge readout is a prerequisite of SCC protocols for enhanced spin readout [78, 150]. Related approaches are widely used for other qubit platforms, including self-assembled and lithographic quantum dots [50, 75] and donor atoms in silicon [122]. Here we consider all-optical readout, although electrical charge measurements are also possible when NVs are incorporated in a junction structure [23, 65, 81]. For all-optical SCC, the charge readout produces larger SNR for longer readout times. Thus, applications with long measurement cycles, such as  $T_1$  sensing schemes, stand the most to gain from spin SNR improvements. NV  $T_1$  relaxometry has enabled gadolinium-based biological sensing [130, 136, 146], direct imaging of nanoscale magnetism [129, 147, 164], as well as microwave-free nanoscale electron spin resonance [70] due to the ground state spin's sensitivity to fast

fluctuating magnetic fields [157, 163]. Since the  $T_1$  times of NVs in nanodiamonds can take values ranging from 3  $\mu\text{s}$  to 4 ms [163], measurement acquisition times can vary over three orders of magnitude depending on the NV under study. A striking example of this signal averaging bottleneck is the recent demonstration of scanning  $T_1$  relaxometry imaging [164], which demands 1 s dwell time per 25 nm-wide pixel, resulting in 2.5  $\mu\text{m}$  wide scans taking 150 minutes to acquire.

## 6.2. Results

Fluorescent nanodiamonds milled from HPHT Ib diamond (Adámas Nanotechnologies) were drop cast onto silicon substrates patterned with titanium gold wires for microwave control [Fig. 17(a)]. While the high-refractive-index substrate preferentially absorbs the NV's PL [76], the effect of reduced collection efficiency contributes a uniform reduction in absolute SNR to all measurement techniques considered here, without affecting relative comparisons. The concentration of the nanodiamond solution was chosen to limit particle aggregation such that isolated nanodiamonds could be resolved in a confocal microscope using 532 nm (2.33 eV) excitation and PL collection. The presence of single and few nanodiamonds was confirmed by comparing atomic force microscope (AFM) scans [Fig. 17(b)] with 2D confocal PL scans [Fig. 17(c)]. The AFM scans in Fig. 17(b) exhibit a height distribution spanning  $39 \pm 19$  nm, in agreement with the vendor's specification. According to the vendor, each nanodiamond contains 10-15 NVs, although the variation in PL brightness across nanodiamonds suggests a broader distribution. More details on the nanodiamond variability are available in the Supporting Information [79]. In addition to the 532 nm pump laser, a continuous-wave 592 nm (2.09 eV) laser is split into two arms for independent power and timing control and subsequently recombined with the excitation path [Fig. 17(a)] for use as a pump or probe for charge state control and measurement. Collected PL was spectrally filtered between 650 nm and 775 nm to suppress emission originating from the  $\text{NV}^0$  charge state and directed to a single-photon avalanche diode. The collected PL signal,  $S(\tau)$ , defined as the time-dependent photon detection rate as a function of the probe duration,  $\tau$ , is

proportional to the population of NV centers in the negative charge state. Further details on the sample preparation and measurement setup can be found in the methods section.

To study the optically induced charge dynamics of the NV ensembles in nanodiamonds, we preferentially populate either the  $\text{NV}^-$  or  $\text{NV}^0$  charge states using 50- $\mu\text{s}$ -duration pulses from 532 nm or 592 nm pump beams, respectively [8], and read out the resulting  $\text{NV}^-$  population with a low-power 592 nm probe beam. Figure 18 summarizes the results of these measurements, in which different initial conditions and probe powers serve to map out the dynamical response due to different ionization and recombination mechanisms [Fig. 18(a)]. The timing sequence is depicted in Fig. 18(b), and the time-correlated PL response due to four different 592 nm probe intensities following pumping by either 532 nm and 592 nm light are shown in Figs. 18(c) and 18(d), respectively. These representative data exhibit multi-timescale and occasional non-monotonic behavior that is observed to varying degrees across a diverse set of 38 nanodiamonds, reported here without any postselection; further data is available in the Supporting Information [79].

We fit all of the data to an empirical multi-exponential function of the form:

$$S_\lambda(\tau) = C_0^{(\lambda)} + \sum_{k=1}^n C_k^{(\lambda)} \exp[-\gamma_k \tau], \quad (6.1)$$

where  $\lambda \in \{532, 592\}$  signifies initialization by green or orange pump beams and  $n$  is the number of exponential terms. The Akaike Information Criterion is used to determine the value of  $n$  required to best represent the observed data [154]. We find that all of the measurements for 38 nanodiamonds can be fit as either single ( $n = 1$ ), bi- ( $n = 2$ ), or tri-exponential ( $n = 3$ ) functions with the coefficient labels ordered such that  $\gamma_1 > \gamma_2 > \gamma_3$ . The solid lines in Figs. 18(c, d) are examples of fits using a tri-exponential model. The distribution of optimized exponential number ( $n$ ) for a total of 152 time-correlated probe responses for both 532 nm and 592 nm pump conditions are shown in Figs. 18(e, f), respectively. In a majority of cases, the tri-exponential model most accurately recreates the data. The relative increase of bi-exponential cases with a 592 nm pump is presumably due to a larger portion of the

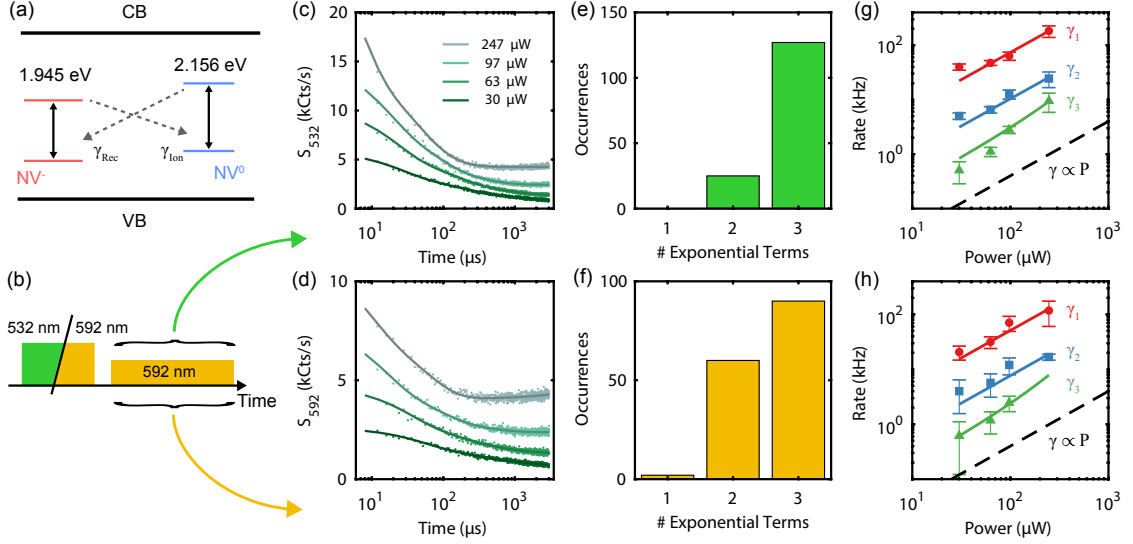


Figure 18: Optical Charge Dynamics (a) Electronic level diagram depicting the  $NV^-$  and  $NV^0$  zero phonon line energies along with charge conversion processes (dotted arrows). (CB, conduction band; VB, valence band) (b) Experimental timing diagram. Charge pump beams are  $50 \mu\text{s}$  in duration. Panels (c)-(h) show examples of the time-correlated PL response (c,d; points) along with tri-exponential fits (c,d; lines), distributions of the optimal number of exponential terms (e,f), and the probe-power dependence of the rates  $\gamma_1$ ,  $\gamma_2$ , and  $\gamma_3$  of the tri -exponential fits in c and d where the top (g) and bottom (h) panel corresponds to initialization with 532 nm or 592 nm illumination, respectively. The dashed line in (g, h) signifies the expected shape of a linear power scaling.

NVs already close to the steady state following initialization with the same wavelength, which simplifies the dynamics. Nevertheless, the fact that dynamical behavior is observed at all following 592 nm initialization is indicative of power-dependent ionization and recombination processes and charge relaxation in the dark, likely due to the lower thermodynamic stability of  $NV^0$  compared to  $NV^-$  [55]. The empirical multi-exponential model could stem from two physical scenarios. The first is that the NV charge dynamics can depend on the free carrier concentration, which is determined by the substitutional nitrogen and other impurity states and can exhibit complex temporal variations under optical pumping[88]. The other scenario is that different local environments for NVs within the ensemble could lead to distinct exponential responses. The present data cannot distinguish these scenarios, but future studies on single NVs in nanodiamonds, potentially with variations in impurity content, can establish which of these physical situations is more likely.

A closer look at the fit results provides insight into the ionization and recombination mechanisms of the NV ensembles. Figures 18(g) and 18(h) display the best-fit rates as a function of laser power for the data in Figs. 18(c) and 18(d), respectively. Since the 592 nm probe intensities are maintained below 6% of the saturation power (4.3 mW), we expect the rates to exhibit a polynomial power dependence whose order depends on the number of photons involved in each ionization or recombination process [171]. The solid lines in Figs. 18(g, h) represent fits to a second-order polynomial [8]. In contrast to the case for single NVs in bulk, type IIa diamond, where ionization and recombination requires at least two photons with a wavelength of 592 nm [8, 78, 171], we observe a non-negligible linear component in the power scaling for all rates and initial conditions. The linear term points to the existence of a single-photon ionization or recombination mechanism. Similar behavior has been observed for NV ensembles in bulk, type-Ib diamond [113], where it is believed to result from tunneling of an electron or hole from the NV excited state to a nearby substitutional nitrogen trap [177]. By computing the excitation rate from a saturation curve, we estimate that  $\approx 3\%$  of all cycling events result in a non-radiative tunneling event.

Despite the complicated dynamics, pumping with 532 nm or 592 nm illumination still produces large differences in the charge populations that can be read out optically. Fig. 19(a) depicts how the different charge distributions manifest as a signal contrast within the time-correlated PL of a representative nanodiamond. Along with the photon counting data, we plot the corresponding single-shot charge measurement SNR as a function of readout duration, which is defined by

$$\text{SNR}(\tau) = \frac{\alpha_{532}(\tau) - \alpha_{592}(\tau)}{\sqrt{\alpha_{532}(\tau) + \alpha_{592}(\tau)}}, \quad (6.2)$$

where  $\alpha_\lambda(\tau) = \int_0^\tau S_\lambda(\tau') d\tau'$  is the total number of photons detected after probe duration  $\tau$  following initialization with wavelength  $\lambda$ . Here we assume the noise is dominated by photon shot noise. The SNR initially increases with  $t$  as more photons are detected but eventually reaches a maximum before decreasing as the contrast vanishes and shot noise

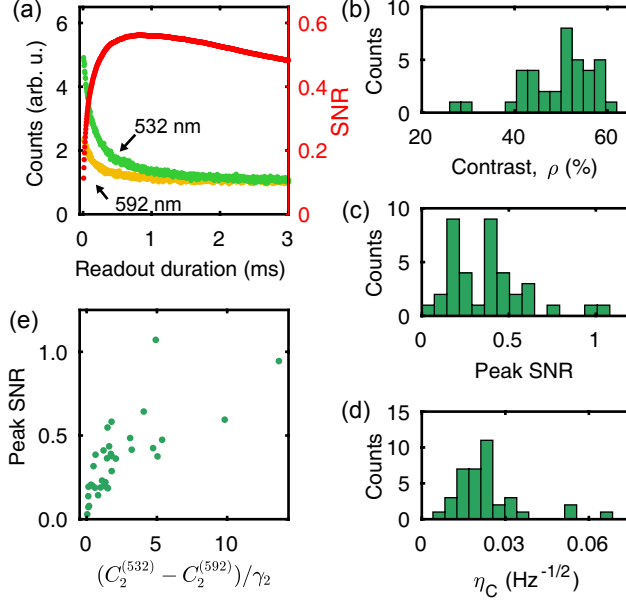


Figure 19: High-Contrast Optical Charge Readout (a) Time-correlated PL traces for 532 nm and 592 nm initial conditions together with the single-shot SNR as a function of readout time. Panels (b)-(d) show distributions of the maximum contrast (b), peak SNR (c), and time-averaged SNR (d) for the 38 nanodiamonds studied. (e) Peak SNR as a function of the charge-dynamics figure of merit discussed in the text.

takes over.

To investigate the universality of this charge readout mechanism, in Figs. 19(b-d) we plot the statistical distributions of various performance metrics calculated from the set of measurements on 38 nanodiamonds summarized in Fig. 18. For each nanodiamond, we calculate the initial optical contrast at the lowest probe power,

$$\rho = \left(1 - \frac{S_{592}(0)}{S_{532}(0)}\right) \times 100\%, \quad (6.3)$$

which reflects the difference in initial charge population. The distribution of  $\rho$ , seen in Fig. 19(b), exhibits a narrow peak around the mean contrast of  $50 \pm 7\%$ . Notably, all of the observed values are lower than the ideal contrast of  $\rho_{\text{bulk}} = 84\%$  expected for NVs in bulk, type-IIa diamond [8]. We attribute this difference to the finite duration of our measurements and the more complicated local environment of NVs in nanodiamonds. Nonetheless, every

nanodiamond we studied exhibits a strong optical charge contrast. Figure 19(c) shows the distribution of peak single-shot SNR values, optimized for readout power and duration. Here we find a much wider distribution with a mean  $\text{SNR} = 0.38 \pm 0.22$ . This large spread of values is not surprising given the widely varying nanodiamond brightness due to different NV ensemble sizes, together with variations in the charge dynamics during readout due to different local environments. Interestingly, the peak SNR distribution is potentially bimodal, however we suspect this to be a statistical anomaly based on the limited sample size and the lack of corresponding bimodal signatures in the related distributions for contrast [Fig. 19(b)] and sensitivity [Fig. 19(d)].

Finally, for each nanodiamond we also calculate the time-averaged charge readout sensitivity,

$$\eta_C = \frac{\sqrt{\tau_R}}{\text{SNR}(\tau_R)}. \quad (6.4)$$

Here we assume that the readout time,  $\tau_R$ , and the probe power are optimized to provide the maximum single-shot SNR. The charge sensitivity has units of  $\text{Hz}^{-1/2}$ , and, assuming shot noise dominates the measurement uncertainty, dividing  $\eta_C$  by the square root of the total integration time,  $T$ , yields the minimum resolvable signal variation,  $\delta = \eta_C/\sqrt{T}$ . The distribution of charge sensitivities is displayed in Fig. 19(d). Twenty of the nanodiamonds surveyed exhibit  $\eta < 0.02$ , meaning that we can resolve 2% signal variations after one second of integration. Despite the wide qualitative variation of optically induced charge dynamics, all nanodiamonds observed in this study showed contrasts between 26% and 61% and charge sensitivity better than  $0.07 \text{ Hz}^{-1/2}$ .

The qualitative variations of charge dynamics and distribution of charge readout performance metrics are not independent of each other. For example, a better charge measurement intuitively requires both a larger contrast to increase the signal amplitude and slower decay rates to allow for more detected photons. To test this hypothesis, we searched for correlations between metrics such as peak SNR, contrast, and sensitivity and particular parameters of our empirical models; further details are available in the Supporting Infor-

mation [79]. Interestingly, the parameters most predictive of peak SNR are the amplitude difference,  $C_2^{(532)} - C_2^{(592)}$ , and rate,  $\gamma_2$ , of the second exponential term in Eqn. 6.1. Figure 19(e) displays the strong correlation between the peak SNR and a combined figure of merit,  $(C_2^{(532)} - C_2^{(592)})/\gamma_2$ . This analysis confirms our physical intuition and also offers an effective means of screening nanodiamonds for optimal performance as charge sensors.

The availability of a high-contrast charge measurement for nanodiamonds is crucial to achieve performance advantages using SCC readout protocols. Figures 20(a) and 20(b) compare the mechanisms for spin readout using traditional PL and SCC, respectively. PL readout results from optically cycling the triplet manifold of  $NV^-$ , typically using a 532 nm pump, which causes the  $m_s = 0$  spin projection to produce more photons (bright state) as compared to the  $m_s = \pm 1$  projection which is shelved *via* the intersystem crossing into the metastable singlet (dark state). The essence of SCC is a timed optical pulse sequence that transfers the initial spin populations into either the triplet manifold (for  $m_s = 0$ ) or the singlet manifold (for  $m_s = \pm 1$ ) and then quickly ionizes the population selectively from one manifold or the other [78, 150]. Following this SCC procedure, a low-intensity, charge-selective probe pulse (592 nm in this work) detects the  $NV^-$  population. Thus, the optical charge readout signal is correlated to the NV's initial spin state.

To verify the SCC mechanism in nanodiamonds, we performed pulsed electron spin resonance (ESR) measurements on a nanodiamond at zero magnetic field. The measurement timing diagrams for PL and SCC readout techniques are sketched in Figs. 20(c) and 20(d), respectively. Both measurement sequences begin with a 5  $\mu$ s, 532 nm pump pulse to initialize the ensemble primarily into  $NV^-$  and  $m_s = 0$ . A weak, variable-frequency microwave pulse with a duration exceeding the inhomogeneous dephasing time ( $\tau_{MW} = 200$  ns) is then applied to probe the ground state spin transition. In the case of PL readout, a second 532 nm pulse is applied and photons are detected for the first 300 ns. For SCC, two pulses of 30 mW 592 nm light (a 15 ns shelving pulse followed 25 ns later by a 50 ns ionization pulse) are applied to perform the conversion process outlined in Fig. 20(b). Due to the

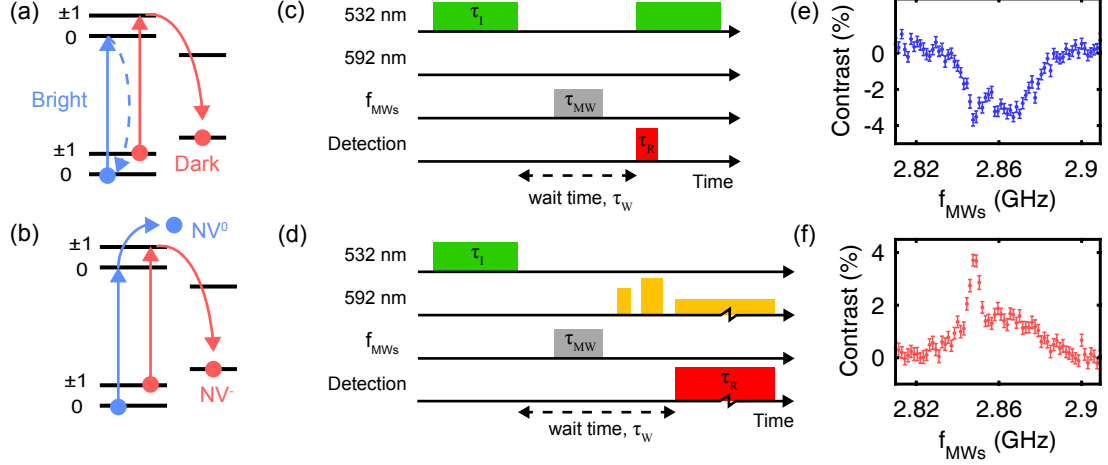


Figure 20: Spin-to-Charge Conversion in Nanodiamonds (a,b) Diagrams of PL spin readout and the SCC process, respectively for  $NV^-$ . Solid lines represent pumped transitions, dotted lines represent radiative transitions. (c,d) Measurement timing diagrams for performing pulsed ESR using PL or SCC readout, respectively.  $f_{MWs}$  corresponds to the variable frequency of the microwave pulse, and the break in the readout pulse of (d) indicates a large span of time.  $\tau_I$ : initialization time,  $\tau_{MW}$ : microwave pulse time,  $\tau_R$ : readout duration. (e,f) Measured ESR spectra for a single nanodiamond using PL and SCC protocols, respectively.

finite rise time of the AOM used to generate these pulses, the power of the shelving pulse is lower than that of the ionization pulse. The same SCC pulse parameters were used for all nanodiamonds in this work. Finally, a  $430 \mu W$ ,  $40 \mu s$  probe pulse is applied with photon detection during the entire duration. Both SCC pulses are derived from one arm of the 592 nm laser path shown in Fig. 17(a) whereas the lower-power probe pulse is generated in the second arm. The results are presented in Figs. 20(e) and 20(f) for PL and SCC readout, respectively. Both spin measurement techniques show the typical response characterizing an NV ensemble with strong inhomogeneous broadening, confirming that SCC does indeed measure the spin state. The qualitative difference in curve shapes suggests that different NVs, spectrally distinguished by their local strain, exhibit different charge readout and SCC contrasts. This suggests that variations in the charge dynamics exist even within a single nanodiamond.

In order to quantify the potential improvement offered by SCC, we studied its spin readout performance in comparison to traditional PL. We calibrated the optimal measurement

parameters for PL readout, and found that, in contrast to the situation in bulk diamond where optical excitation close to saturation is preferred, the optimal 532 nm readout pulse was tuned to a factor of 4 below the saturation power for a duration of 300 ns; additional data is available in the Supporting Information [79]. This observation agrees with other recent measurements of reduced spin SNR for NVs in nanodiamonds on sapphire substrates [20]. The non-NV PL contributes background levels  $< 1\%$  of the signal at the optimum spin readout power, so this cannot explain the anomalous SNR decrease. We believe the more complicated ionization and recombination mechanisms are the primary cause of this SNR decrease, since the probabilities of non-radiative charge transitions from the  $\text{NV}^-$  excited state are comparable to those for the intersystem crossing [60].

Figure 21(a) shows the resulting single-shot spin SNR for a single nanodiamond as a function of the probe pulse intensity ( $P_R$ ) and duration ( $\tau_R$ ). This particular nanodiamond has favorable charge and spin properties, with a peak charge-detection  $\text{SNR} = 0.36$  and spin  $T_1 = 780 \pm 230 \mu\text{s}$ .  $T_1$  measurement data is available in the Supporting Information [79]. We observe that SCC out-performs PL readout whenever  $\tau_R > 10 \mu\text{s}$ , with a factor of 3.8 improvement in SNR for  $\tau_R \approx 1 \text{ ms}$ . As in the case of charge readout, for time-averaged measurements this presents an optimization tradeoff between the single-shot SNR and measurement duration. Therefore, in analogy to eqn. (6.4), we calculate the time-averaged spin-readout sensitivity,

$$\eta_{\text{SCC}}(\tau_W) = \max_{\tau_R, P_R} \left( \frac{\sqrt{\tau_I + \tau_W + \tau_R}}{\text{SNR}(\tau_R, P_R)} \right), \quad (6.5)$$

where  $\text{SNR}(\tau_R, P_R)$  is the single-shot spin SNR at a given readout duration,  $\tau_R$ , and power,  $P_R$ . Here we must include the total duration of the measurement sequence, composed of the constant initialization time,  $\tau_I$ , and the variable waiting time (or, more generally, the spin-operation time),  $\tau_W$ , in addition to  $\tau_R$ . The waiting time will depend on the desired sensing scheme. An example for a pulsed ESR implementation is depicted in Figure 20(c,d). Fig. 21(b) depicts how the quantity  $\left( \frac{\sqrt{\tau_I + \tau_W + \tau_R}}{\text{SNR}(\tau_R, P_R)} \right)^{-1}$  varies over the two dimensional mea-

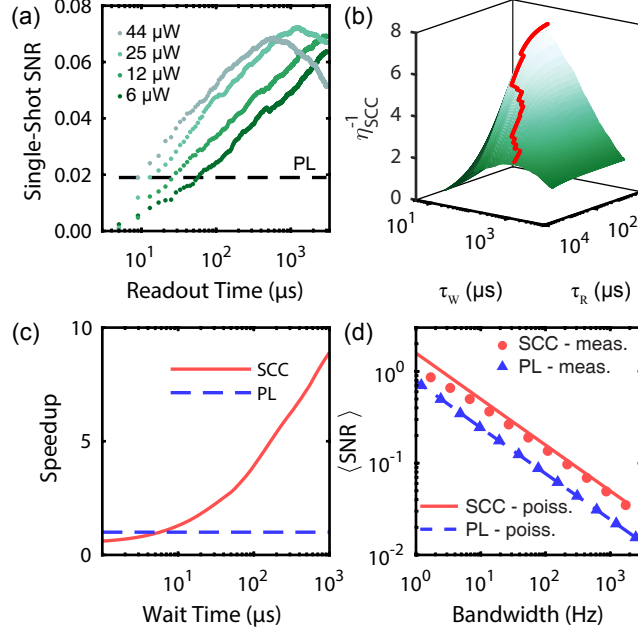


Figure 21: Performance of the SCC Protocol (a) Calibration of the SCC spin SNR (points). The measured PL SNR = 0.019 is indicated by a dashed line. (b) Inverse of the SCC sensitivity figure of merit (see text) as a function of wait time and readout duration, calculated from the data in (a). The red solid line indicates the optimum sensitivity found by optimizing the readout duration for a given wait time, while the surface depicts how the sensitivity varies across both parameters. (c) Predicted speedup factor as a function of measurement wait time. (d)  $T_1$  relaxometry measurement comparing the time-averaged SNR as a function of bandwidth for PL (blue triangles) and SCC (red circles) readout. The solid (dashed) lines indicate the predicted SNR calculated in a shot noise approximation for SCC (PL). Error bars are smaller than the data markers.

surement parameter space consisting of  $\tau_W$  and  $\tau_R$ , once  $P_R$  has already been optimized. The red line tracing the ridge of the surface provides a visual indicator of the optimal sensitivity for a given wait time, in which the readout duration has been optimized.

Using this analysis, we can make a direct comparison between the performance of SCC and traditional PL protocols. The PL readout sensitivity,  $\eta_{PL}(\tau_W)$ , is calculated in a similar manner to eqn. (6.5), except we assume the readout power and duration remain fixed at their single-shot optimal values. Then we calculate the speedup factor, *i.e.*, the ratio of

acquisition times required to achieve a common time-averaged SNR,

$$F(\tau_W) = \left( \frac{\eta_{\text{PL}}(\tau_W)}{\eta_{\text{SCC}}(\tau_W)} \right)^2. \quad (6.6)$$

The results of this analysis for the nanodiamond investigated are plotted in Fig. 21(c). The break-even wait time, when  $F = 1$ , occurs when  $\tau_W = 6 \mu\text{s}$ , and by  $\tau_W = 100 \mu\text{s}$  the speedup has reached a factor of 5. Physically, this increase stems from the kHz dynamics governing charge readout, which allows for long acquisition times and thus a large number of detected photons in each shot. In principle,  $F$  will increase with  $\tau_W$  to a saturated value determined by the squared ratio of the single-shot SNRs ( $\lim_{\tau_W \rightarrow \infty} (F) \approx 14$  in this case). In practice, however, the range of useful values for  $\tau_W$  is limited by the sensing protocol of interest and ultimately by the spin lifetime.

To demonstrate performance improvements in a practical setting, we performed  $T_1$  spin relaxometry measurements in which a fixed wait time of  $\tau_W = T_1/2 = 390 \mu\text{s}$  was used to sense magnetic disturbances in the local environment [163]. The target signal consisted of low-power microwaves driven through the lithographic wire at 2.87 GHz to simulate the presence of fast fluctuating magnetic fields around the nanodiamond. The presence of the microwaves reduces  $T_1$  by more than an order of magnitude. Using the optimized SCC settings of  $P_R = 44 \mu\text{W}$  and  $\tau_R = 173 \mu\text{s}$ , we performed differential relaxometry measurements, comparing the signal with the microwaves on and off, for a range of total measurement bandwidths,  $(1/T)$ , where  $T$  is the total measurement time. At each bandwidth, the time-averaged signal-to-noise ratio,  $\langle \text{SNR} \rangle = \Delta N / \sigma_N$ , was calculated from the mean differential photon-counting signal,  $\Delta N$ , and the corresponding standard deviation,  $\sigma_N$ , for each technique. This procedure was repeated 11 times to obtain statistics on the measured  $\langle \text{SNR} \rangle$ . The results are plotted in Fig. 21(d) along with the predicted variation of  $\langle \text{SNR} \rangle$  assuming only Poissonian noise contributions. We observe an improvement from the SCC protocol by a factor  $2.26 \pm 0.14$  corresponding to a speedup of  $F = 5.11 \pm 0.63$ , nearly independent of bandwidth. Interestingly, while the measurements agree closely with the shot-noise pre-

diction for the PL protocol, the model including only Poissonian noise overestimates  $\langle \text{SNR} \rangle$  for the SCC protocol by 8%. We attribute this slight difference in SNR to elevated noise that results from the SCC measurement being described by a joint-probability distribution comprised of binomial and Poissonian random variables [78, 150]. The resulting noise in the counted photons exceeds that of just the Poissonian case. Since neither the number of NVs nor the SCC efficiency are known, the exact parameters cannot be extracted from the measurement. Nonetheless, this yields only a minor correction to the SNR, due to the inherent averaging over an ensemble of NVs. Larger NV ensembles will reduce the contribution of this binomial noise as  $\sqrt{N}$ , where  $N$  is the number of NVs in the ensemble. The slight decrease of  $\langle \text{SNR} \rangle_{\text{SCC}}$  for bandwidths  $< 10$  Hz is due to elevated power fluctuations of the 592 nm laser for time scales  $> 100$  ms that manifest in increased noise over long integrations. Data characterizing the noise in the detected PL is available in the Supporting Information [79].

Similar measurements to those previously described on large nanodiamond agglomerates containing several hundred NVs attest to the universality of the SCC protocol. The Supporting Information includes SCC calibration curves like Fig. 21 for such agglomerates, and Fig. 17(a) depicts the amplification effect corresponding to a factor of 2.2 SNR improvement (factor of 5 speedup) for an agglomerate containing  $\approx 100$  NVs and for  $\tau_{\text{W}} = 75$   $\mu\text{s}$ . Future studies into the potential relationship between  $T_1$  and SCC performance could provide more insights into the effect of the NV's local environment on these two quantities.

### 6.3. Discussion

The techniques described in this paper can be used to improve various schemes for nanoscale sensing, which are typically limited by the poor spin and charge environment of NVs in nanodiamonds. The optical charge readout technique can readily be applied to measuring variations in the electrochemical potential surrounding nanodiamonds, produced for example by using an electro-chemical cell [94] or functional groups on the nanodiamond surface [131]. One potential future application of electrochemical sensing is the detection of neuron

action potentials, which have  $\approx 100$  mV amplitudes and millisecond durations. Comparing the time-averaged SNR measured by Karaveli *et al.* [94] using 532 nm PL to our high-contrast charge measurements, we predict a factor of 5 improvement in charge sensitivity, corresponding to a factor of 25 speedup and the ability to detect millivolt-scale variations in electrochemical potential on millisecond timescales. This can offer a microwave-free alternative to emerging techniques for action-potential sensing using NV ensembles in bulk diamond [13] and the potential to extend these imaging modalities to *in-vivo* studies. The availability of high-contrast charge readout with tunable duration suggests a promising avenue of research in developing optical pulse sequences for measuring chemical potentials and changes in the dark charge dynamics.

The simplified two-wavelength protocol reduces the experimental complexity required to implement SCC for spin-readout enhancements. In addition, the applicability to nanodiamonds offer a means to further improve nanodiamond magnetic sensing protocols, particularly for  $T_1$  relaxometry where the spin-evolution time is long. For example, the factor of 5 speedup for  $T_1$  sensing exhibited in Fig. 21(d) would reduce the total acquisition time of the 2D relaxometry images demonstrated by Tetienne *et al.* [164] from 150 minutes to 30 minutes. These throughput improvements allow for the ability to measure more samples and also reduce the experimental complexity required to keep the imaging optics and sample stationary for such long periods of time. Motivated by recent advances in using SCC to improve magnetometry with single NVs in planar bulk diamond [87], our results also motivate the investigation of other diamond NV platforms, such as bulk ensembles, shallow implanted NVs, and NVs coupled to waveguides or other photonic structures, all of which could achieve spin readout enhancements through the use of the time-averaged SCC protocol presented here. For example, higher-purity nanodiamonds with spin coherence times approaching bulk diamond [97, 166] stand to gain spin-readout enhancements from SCC for phase-coherent sensing protocols and measurements of electron-nuclear coupling [98, 99], where longer spin operation times are required. The lower nitrogen content in these nanodiamonds will also improve the charge readout SNR closer to bulk high-purity

diamond levels. The promising improvement of  $T_2$  times of NVs in nanodiamonds as well as for shallow, implanted NVs [51] suggests that these platforms will invariably encounter signal averaging issues as well, at which point SCC can offer major improvements. The demonstration of improved sensing performance for type Ib nanodiamonds provides conclusive evidence that SCC can be utilized in diamond hosts with elevated impurity levels and for NVs near surfaces. In particular, nano-NMR experiments [7, 110, 111] with near-surface NVs can improve spin readout performance using the all-optical techniques presented here.

#### 6.4. Conclusion

We have developed all-optical protocols to amplify the charge and spin readout signals of NV ensembles in nanodiamonds with immediate applicability for improving quantum sensing applications. A preliminary study of the optically induced charge dynamics suggests that the local environment of each NV within a given nanodiamond modulates the dynamics. Additional ionization and recombination mechanism that are not present for single NVs in high-purity diamond are consistent with the idea of tunneling between the NV excited state and nearby charge traps, although the intriguing dark dynamics warrants further investigation. Despite these drastically different charge dynamics, a sample of 38 nanodiamonds demonstrates the universality of the proposed high-contrast charge readout for these particles. We further demonstrate a simplified two-color SCC protocol for nanodiamonds that provides spin readout enhancements in the context of a  $T_1$  relaxometry measurement, resulting in a factor of 5 reduction in measurement acquisition time. These results provide a straightforward method for improving state-of-the-art quantum sensors beyond the limits already achieved using conventional PL spin readout. The improved sensing of electrochemical potentials motivates the development of nanodiamond charge sensors for measuring action potentials and local chemical potentials *in-vivo*, and the clear benefit of SCC even for impurity-rich, type IB nanodiamonds motivates the extension of these techniques to other near-surface NV sensing platforms.

## 6.5. Methods

### 6.5.1. Sample Preparation

Nanodiamonds were purchased from Adamas Nanotechnologies, item No. ND-15NV-40nm, and were reported to have a mean diameter of 40 nm with approximately 10-15 NVs per ND. To produce single and few nanodiamonds through drop casting, the ND slurry of concentration  $1 \text{ mg mL}^{-1}$  was diluted by 4 orders of magnitude followed by horn sonication to break up agglomerates. The diluted solution was immediately drop cast onto  $\text{O}_2$ -plasma-cleaned silicon substrates and allowed to dry in atmosphere. The presence of isolated single and few nanodiamonds was confirmed by correlating atomic force microscope (AFM) measurements (MFP-3D atomic-force scanning probe, Asylum) and photoluminescence (PL) maps, as can be seen in Fig. 17(c, d). For the studies involving agglomerates of nanodiamonds, the original concentration ( $1 \text{ mg mL}^{-1}$ ) was dropcast directly onto a cleaned silicon substrate. The estimated number of NVs in the agglomerate was calculated by comparing saturation count rates of single nanodiamonds and the agglomerates.

### 6.5.2. Confocal Microscope Details

Nanodiamonds are imaged with a home-built confocal microscope with two excitation sources. Continuous-wave 532 nm (Gem 532, Laser Quantum) and 592 nm (VFL-592, MPB Communications, Inc.) lasers are gated with acousto-optic modulators (AOMs, 1250c, Isomet) with rise times of 30 ns. The 592 nm laser is split with a beamsplitter (BS025, Thorlabs) into two arms to provide independent power control (NDC-50C-4, Thorlabs and 5215, Newport) and temporal gating. The beams are recombined with another beamsplitter (BS028, Thorlabs). The 532 nm beam line is double passed through the AOM, which improves the extinction ratio to  $>60 \text{ dB}$  and eliminates unwanted exposure to low power light which will cycle the defects' charge state between  $\text{NV}^-$  and  $\text{NV}^0$  and reduce  $T_1$  times. The 532 nm and 592 nm beams are combined with a dichroic filter, co-aligned on a fast steering mirror (FSM, OIM101, Optics in Motion) and imaged through a  $4f$  lens configura-

ration onto the back of an objective (Olympus MPlanFL N 100x, 0.9 NA). The collected photoluminescence is filtered to select for  $NV^-$  in the 650 nm - 775 nm band, and focused onto a 50  $\mu\text{m}$ -diameter-core multi-mode optical fiber (M42L01, Thorlabs) that is connected to a single photon avalanche diode (Count-20c-FC, Laser Components). Photon detection events are recorded with a data acquisition card (DAQ-6323, National Instruments), which also functions as the global experimental clock. An arbitrary waveform generator (AWG520, Tektronix) controls the microwave pulse timing, optical pulse timing, and photon count gating. Microwaves are either supplied by lithographically patterned titanium-gold wires, or a gold bond wire laid across the silicon substrate. The output of a signal generator (SG384, Stanford Research Systems) is modulated with a high-isolation switch (ZASWA-2-50DR+, MiniCircuits) and sent through a 16 W amplifier (ZHL-16W-43-S+, MiniCircuits), which provides the microwaves for ground state spin control.

## CHAPTER 7 : Real-Time Charge Initialization

The experiments and analysis of this chapter were completed in a close collaboration with Joseph Lauigan and Tzu-Yung Huang.

### 7.1. Introduction

The accelerating pace of quantum technology is evident in the advancement of quantum sensors [39] and the emergence of quantum networks [174]. Critical to these developments have been solid-state spin qubits based on semiconductor defects, due to their optical interface [11], compatibility with integrated technologies [149], and wide selection of host materials [9]. The most well-known example is the nitrogen-vacancy (NV) center in diamond [44, 80], which has enabled pivotal advances in quantum sensing [6, 7, 13, 21, 62, 110, 148] and quantum information processing [22, 77, 83].

One limitation to the performance of NV-center qubits is imperfect initialization into the oft-desired negative charge state ( $NV^-$ ). Optical pumping with 532 nm light produces a steady-state statistical charge distribution; typically the probability to prepare the  $NV^-$  state is around 75% [8, 171], although it can be much lower for defects close to surfaces [19]. This probabilistic steady-state initialization (SSI) hampers spin readout by decreasing contrast and increasing readout noise [80], and it limits the fidelity of quantum gate operations of coupled spin systems utilizing the NV center as an ancilla [124, 171]. Existing techniques to improve the charge initialization fidelity include doping electrically [47] or chemically [46], and multi-color optical pumping [78]. In addition, many experiments utilize post selection to filter out the noise [19, 78, 150, 170, 172, 173]. These techniques either impose strict constraints on materials and device design or require elongated experimental runtime. At cryogenic temperatures, deterministic initialization protocols based on real-time feedback have been essential for entanglement generation and quantum error correction using NV centers due to their long measurement times [16, 33, 83], however these techniques have not been adapted for quantum sensing applications where the duration of each measurement

cycle drastically affects the overall sensitivity.

Here, we use real-time feedback to control an NV center’s charge-state initialization fidelity at room temperature, and we demonstrate improved spin readout efficiency and sensitivity. A model for the stochastic initialization procedure allows for the selection of near-unity initialization fidelity into either charge state, or an arbitrary intermediate charge distribution. We measure the influence of charge fidelity on the spin readout signal-to-noise ratio (SNR) for two readout techniques, traditional photoluminescence (PL) and spin-to-charge conversion (SCC). Our comprehensive model allows for the optimization of initialization and readout parameters for quantum control experiments of arbitrary durations. The real-time initialization (RTI) protocol improves the spin readout efficiency and reduces the time required for experiments; in combination with SCC readout, we demonstrate a factor-of-20 speedup as compared to traditional methods.

## 7.2. Experimental Setup

A schematic of the experiment is shown in Fig. 22(a). The traditional portion of the setup consists of the lasers, microwave sources, diamond device, and photon-counting electronics. The sample is an electronic grade, type-IIa, synthetic diamond (Element Six) which has been irradiated with 2 MeV electrons ( $10^{14}$  cm<sup>-2</sup>) and annealed at 800°C for 1 hour in forming gas. A solid immersion lens aligned to a single NV center was fabricated using focused-ion-beam milling to increase the photon collection efficiency [78], resulting in a saturated count rate of 300 kCts s<sup>-1</sup>. Imaging and optical control is performed with a home-built room-temperature scanning confocal microscope with three excitation sources. A continuous-wave 532 nm laser (Gem 532, Laser Quantum), referred to as “green,” is gated by an acousto-optic modulator (AOM) in a double-pass configuration; it is used for optical pumping and traditional PL readout. An amplitude modulated 635 nm laser diode (MLD 06-01 638, Cobolt), referred to as “red,” is used for charge readout and SCC. A continuous-wave 592 nm laser (VFL-592, MPB Communications, Inc.), referred to as “orange,” is gated with an AOM and is used for SCC. A 115 G magnetic field is aligned

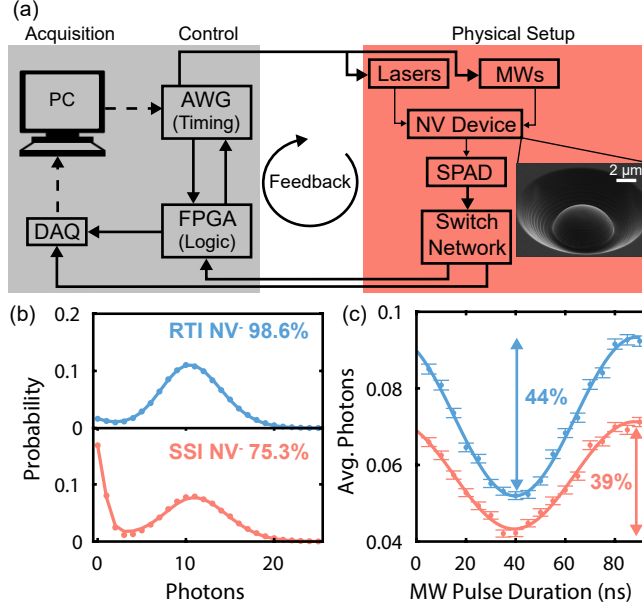


Figure 22: Real-Time Charge Initialization. (a) System overview for implementing real-time feedback on a nitrogen-vacancy (NV) center’s charge state. Inset: scanning electron micrograph of a solid immersion lens fabricated around a single NV center. (DAQ: data acquisition, AWG: arbitrary waveform generator, FPGA: field programmable gate array, MWs: microwaves, SPAD: single-photon avalanche diode). (b) Charge-readout distributions demonstrating the difference in charge state initialization fidelity for the real-time (RTI, top panel) and steady state (SSI, bottom panel) initialization protocols. (c) Rabi nutations of a single NV center following RTI (top, blue curve and data points) and SSI (bottom, salmon curve and data points) demonstrating the increased signal and spin contrast (signified by the arrows). Curves are fits to a sinusoidal oscillation.

along the NV axis to distinguish the  $m_s = \pm 1$  states. A lithographically-defined loop-antenna surrounding the solid immersion lens is driven by an amplified (ZHL-16W-43-S+, Mini-Circuits), amplitude modulated (ZASWA-2-50DR, Mini-Circuits), continuous-wave signal generator (SG384, Stanford Research Systems), which allows for ground-state spin control.

The NV center’s charge state is determined to a high accuracy by utilizing a wavelength that excites the  $NV^-$  zero phonon line of 637 nm but not the  $NV^0$  zero phonon line of 575 nm [172]. Example histograms of photon counts arising from 75,000 charge readouts are shown in Fig. 22(b) for both the steady-state  $NV^-$  population of  $75.3 \pm 0.4\%$  and a higher fidelity initial population of  $98.6 \pm 0.2\%$ . These populations were determined by

fitting to a statistical model describing the observed photon number histogram [150]. The SSI value of  $\sim 75\%$  agrees with previous measurements [8]. The benefit of this elevated initialization fidelity can be seen in the ground-state Rabi nutations in Fig. 22(c), where the higher purity charge state exhibits higher brightness and contrast.

We implement real-time control by linking our timing electronics, which consist of an arbitrary waveform generator (AWG, AWG520 Tektronix) and data acquisition (DAQ, National Instruments) system, with the fast digital logic of a field programmable gate array (FPGA, Virtex-7 Xilinx); refer to Figure 22(a) for the full system overview. In the initialization control loop, the AWG outputs a sequence consisting of a green pump and red charge probe in an repeating loop; when the FPGA detects that a preset photon detection threshold has been reached during the charge probe, it sends an event signal to advance the AWG out of its loop and continue with the other predefined measurements. The time it takes from detection of the final photon to the halting of the initialization procedure is  $\tau_{\text{delay}} = 550$  ns, which consists of the detector delay (30 ns), the AWG delay (500 ns), and the red laser delay (20 ns).

### 7.3. Results

We model the charge probe process using a photon distribution model accounting for transitions between  $\text{NV}^-$  and the neutral ( $\text{NV}^0$ ) charge state [35, 68, 150]. The model assumes that the charge dynamics of the NV center can be reduced to a two-state system with emission rates  $\gamma_-$  and  $\gamma_0$ , and charge transition rates for ionization (negative to neutral,  $\Gamma_{\text{Ion}}$ ) and recombination (neutral to negative,  $\Gamma_{\text{Rec}}$ ); see Fig. 23(a). We determine these rates as a function of power by measuring the photon distributions during a time bin that allows for about one ionization event to occur and fitting to the model. Since the charge readout powers used in this work are below the saturation regime, the emission rates scale linearly with laser power while the ionization and recombination rates scale quadratically with power [8, 171].

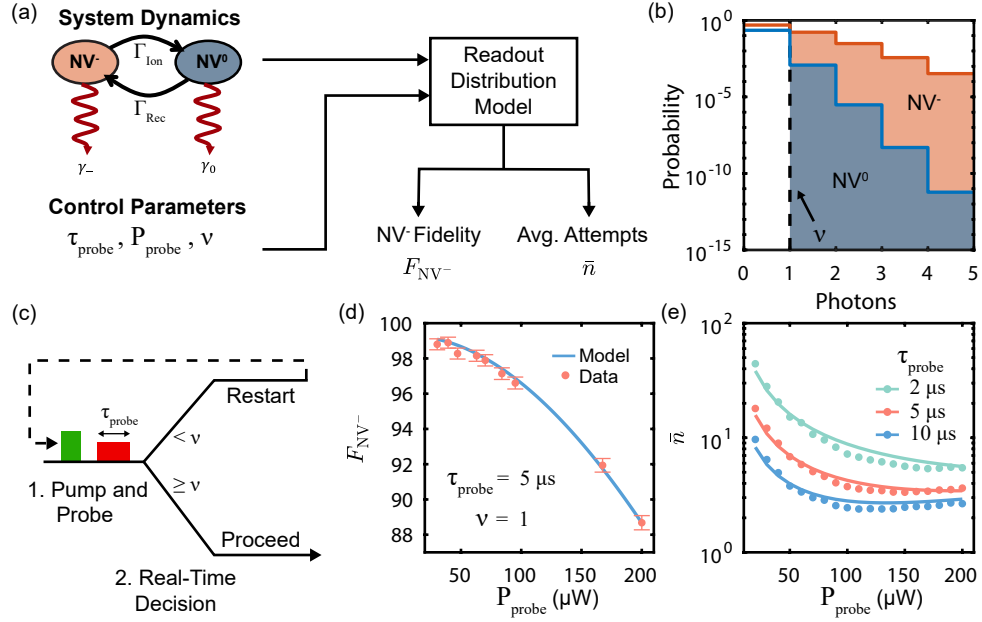


Figure 23: Modeling Real-Time Control. (a) Conceptual diagram of the model. The system dynamics model describes how the charge-dependent emission rates ( $\gamma_-$ ,  $\gamma_0$ ) and charge interconversion rates ( $\Gamma_{Ion}$ ,  $\Gamma_{Rec}$ ) depend on illumination power ( $P_{probe}$ ). Given a readout duration ( $\tau_{probe}$ ) and a threshold condition ( $\nu_{threshold}$ ), the readout distribution model determines the  $NV^-$  fidelity and the average number of attempts required to reach the threshold. (b) Modeled photon distributions for the two charge states with  $\tau_{probe} = 5 \mu s$  and  $P_{probe} = 100 \mu W$ . (c) Experimental timing diagram and decision tree for initializing the charge state. (d) Comparison between the modeled (line) and measured (markers)  $NV^-$  fidelity as a function of probe power. (e) Comparison between the modeled (lines) and measured (markers) average attempts to reach the threshold ( $\nu = 1$ ) as a function of powers and probe duration. Error bars in (e) are comparable to the marker size.

The control parameters governing the charge probe process are the laser power ( $P_{\text{probe}}$ ), maximum duration ( $\tau_{\text{probe}}$ ), and the photon threshold ( $\nu$ ) that defines the termination condition of the initialization loop [Fig. 23(a)]. Given these three parameters, the model provides the expected photon distributions for the negative or neutral charge state configurations,

$$p(n|s), \quad (7.1)$$

where  $n$  is the number of photons detected during  $\tau_{\text{probe}}$  and  $s = -$  or  $0$  signifies the initial charge state; see Fig. 23(b) for an example.

The distributions allow us to calculate two critical metrics for RTI: the  $\text{NV}^-$  charge fidelity ( $F_{\text{NV}^-}$ ) and the average attempts ( $\bar{n}$ ) required for successful initialization. The initialization fidelity is governed by two terms,

$$F_{\text{NV}^-} = (1 - \epsilon_{\text{T}})(1 - \epsilon_{\text{D}}), \quad (7.2)$$

where  $\epsilon_{\text{T}}$  is the threshold error and  $\epsilon_{\text{D}}$  is the delay error. The threshold error is the probability that  $\text{NV}^0$  leads to a threshold reaching event and is given by

$$\epsilon_{\text{T}} = \frac{\sum_{n \geq \nu} (1 - P_-) p(n|0)}{\sum_{n \geq \nu} [P_- p(n|-) + (1 - P_-) p(n|0)]}, \quad (7.3)$$

where  $P_-$  is the probability that the NV center was initially in  $\text{NV}^-$  prior to the charge probe. The delay error is the probability that an ionization event occurred during the electronic delay time and is given by

$$\epsilon_{\text{D}} = 1 - e^{-\tau_{\text{delay}} \Gamma_{\text{Ion}}}. \quad (7.4)$$

The average attempts to initialize is given by

$$\bar{n} = \left( \sum_{n \geq \nu} P_- p(n|-) + (1 - P_-) p(n|0) \right)^{-1}. \quad (7.5)$$

As an ensemble average,  $\bar{n}$  takes continuous values.

Figure 23(c) outlines the experimental decision tree in the real-time initialization procedure. A charge pump-and-probe sequence is repeatedly played out by the AWG until the FPGA detects a threshold reaching event. The green pump pulse is set to 500  $\mu\text{W}$  and 500 ns to quickly repump the charge without incurring significant overhead; we vary  $P_{\text{probe}}$  and  $\tau_{\text{probe}}$  to optimize the performance. In order to verify our model, we measure  $F_{\text{NV}^-}$  and  $\bar{n}$  as a function of  $P_{\text{probe}}$  as shown in Figs. 23(d) and (e). We extract  $F_{\text{NV}^-}$  by performing a subsequent charge measurement and fitting to the photon distribution model, and determine  $\bar{n}$  from the time it takes to record  $10^5$  threshold reaching events.

The measurements of  $F_{\text{NV}^-}$  are generally consistent with our model. We attribute the minor discrepancy between the measured values of  $\bar{n}$  and the model predictions to minor variations in the steady-state charge population imposed by the control sequence. The model assumes a fixed initial  $\text{NV}^-$  population of  $P_- = 75\%$ , however we observe that the initial population depends weakly on the probe duration and power used in a repeated experiment. We neglect this higher-order effect since it has the beneficial effect of decreasing  $\bar{n}$  for the control parameters we employ.

The relative contribution of the two error sources in the charge initialization fidelity depend on  $P_{\text{probe}}$ . At very low powers,  $\epsilon_{\text{T}}$  is dominant and  $F_{\text{NV}^-}$  is limited by the signal-to-background ratio of the charge readout process. For a threshold of 1 photon, the maximum achievable fidelity is  $98.6 \pm 0.2\%$  at low powers [Fig. 23(d)], however  $\bar{n}$  becomes large. At higher powers, corresponding to lower  $\bar{n}$ ,  $\epsilon_{\text{D}}$  is dominant due to the quadratic scaling of the ionization rate with power. Therefore, when designing an experiment utilizing RTI that is sensitive to timing overheads, it is crucial to minimize the control delay time in order to maintain high initial fidelity along with a small  $\bar{n}$ .

To verify that RTI preserves the ground state spin properties, we measured the coherence times for Ramsey ( $T_2^*$ ) and Hahn echo ( $T_2$ ) measurements, as well as the spin

relaxation time ( $T_1$ ). We observe a  $\sim 16\%$  increase in  $T_2^*$  when utilizing RTI, which could be due to ionization of nearby neutrally charged substitutional nitrogen donors ( $S = 1/2$ ) to the positive charge state ( $S = 0$ ) [45], but we detect no statistically significant difference in  $T_2$  or  $T_1$ .

We now consider the effect of the initial  $F_{\text{NV}^-}$  on the spin readout SNR. Generally, the observable for a spin measurement of an NV center follows the form

$$\langle S_i \rangle = \langle \tilde{S}_i \rangle F_{\text{NV}^-} + \langle \epsilon \rangle (1 - F_{\text{NV}^-}), \quad (7.6)$$

where  $\langle S_i \rangle$  is ensemble-averaged value of the observable  $S$  for the spin state  $i$ ,  $\langle \tilde{S}_i \rangle$  is the expectation value of the observable for spin state  $i$  given an initial  $\text{NV}^-$  state, and  $\langle \epsilon \rangle$  is an error in the observable which is due to the NV center residing in  $\text{NV}^0$  during the readout. The single-shot SNR for spin readout is then given by

$$\text{SNR} = \frac{|\langle S_0 \rangle - \langle S_1 \rangle|}{\sqrt{\sigma_0^2 + \sigma_1^2}}, \quad (7.7)$$

where  $\sigma_i$  is the standard deviation associated with  $\langle S_i \rangle$  [80].

To make quantitative comparisons between readout techniques, the physical observable and its accompanying statistical model must be incorporated into equation (7.7). For PL readout [Fig. 24(a)], the signal is the average number of detected photons during the first 250 ns of 532 nm illumination and thus obeys Poissonian statistics. For SCC readout [Fig. 24(b)], the signal is the probability of detecting  $\text{NV}^-$  following the conversion, and it obeys Binomial statistics.

Figure 24(c) details the measurement timing diagram that allows for the characterization of spin SNR as a function of  $F_{\text{NV}^-}$ . Following initialization with an arbitrary  $F_{\text{NV}^-}$ , the spin state is either left in the polarized  $m_s = 0$  state, or flipped to the  $m_s = -1$  state with a 40 ns microwave  $\pi$ -pulse. We estimate the value of  $\langle S_i \rangle$  from repeated measurements using both traditional and SCC readout techniques. We also measure the spin SNR for the

traditional SSI consisting of 2  $\mu\text{s}$  of 532 nm illumination. We separately optimize PL and SCC readout parameters to ensure a fair comparison between the techniques. The raw data are fit using equation (7.6), from which we empirically determine  $\langle \tilde{S}_i \rangle$  and  $\langle \epsilon \rangle$ . Figure 24(d) depicts the results of this measurement for both readout protocols, with the SNR calculated using equation (7.7) for both the data (symbols) and fits (curves).

Interestingly, the spin SNR following RTI for both SCC and PL readout, when controlling for  $\text{NV}^-$  fidelity, is  $\sim 7\%$  higher than for SSI. This is attributed to improved optical spin polarization in the real-time protocol, since the red laser induces negligible recombination; this is consistent with previous observations [29]. The initial spin purity, estimated from measurements of the excited-state lifetime, is approximately 91% and 94% for the steady state and real-time protocols, respectively.

By combining the RTI model with the spin SNR as a function of  $F_{\text{NV}^-}$ , we can optimize the signal acquisition for a given experiment. To achieve this, we define the readout efficiency,

$$\xi = \frac{\text{SNR}}{\sqrt{\tau_I + \tau_O + \tau_R}}, \quad (7.8)$$

where  $\tau_I$  is the initialization time,  $\tau_O$  is the spin operation time, and  $\tau_R$  is the spin readout time. This figure of merit is related to the sensitivity, and encompasses the single-shot SNR, the spin operation duration, and the associated initialization and readout overheads [80]. The total SNR after multiple measurement cycles with a total integration time,  $T$ , is simply given by  $\langle \text{SNR} \rangle = \xi \sqrt{T}$ . We assume the operation time is fixed by the desired sensing or computation protocol. We have previously considered the optimization of the readout duration, power, and threshold for SCC, and we include those procedures when necessary [79, 80].

Real-time control allows for additional design flexibility in an experiment, as longer time spent initializing results in a higher spin readout SNR yet fewer total averages. Equa-

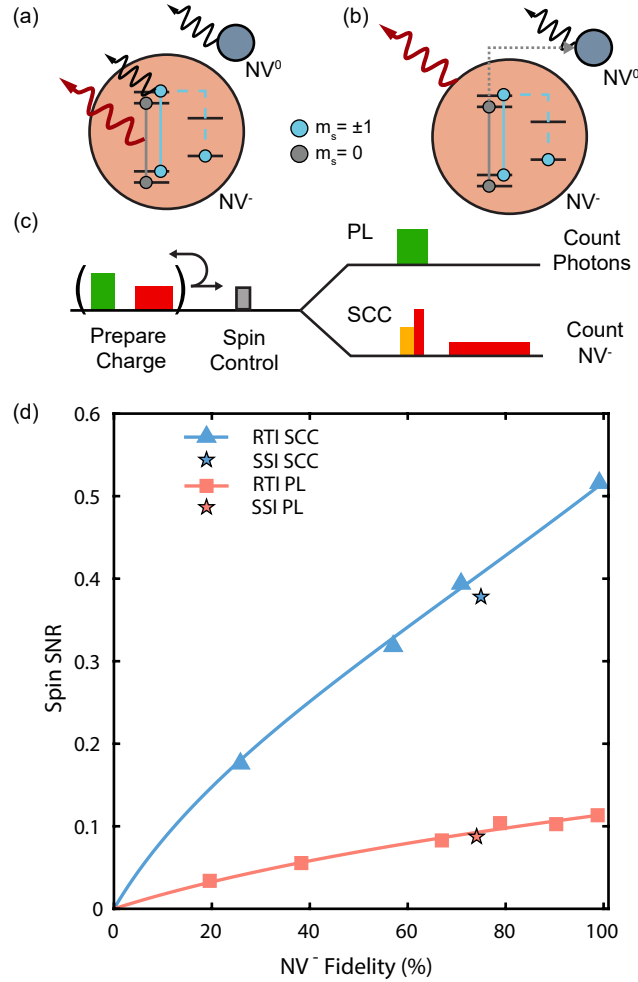


Figure 24: Charge Initialization Fidelity and Spin Readout (a,b) Conceptual diagram for traditional PL readout (a) and SCC (b). Red curves represent the desired signal and black curves contribute to background. (c) Timing diagram for measuring the spin signal-to-noise ratio (SNR) given different heralded charge fidelity. (d) Spin SNR as a function of NV<sup>-</sup> fidelity for different initialization and readout techniques. The solid lines represent a fit of equation Eq. 7.6 to the data, where the fit and data are converted to SNR using Eq. 7.7. Errorbars are comparable in size to the markers.

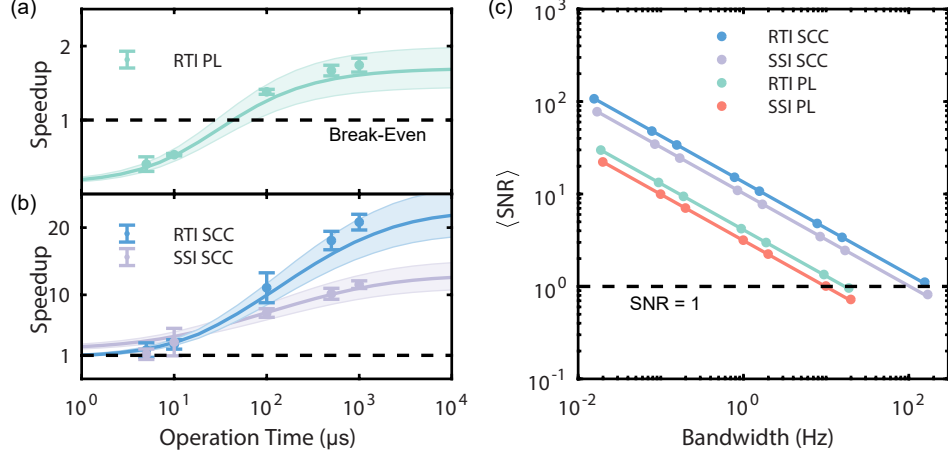


Figure 25: Readout Improvements Through Real-Time Initialization. Predicted (curves) and measured (data points) speedup for PL spin readout with RTI (a) and SCC readout using SSI and RTI (b). The dashed black line in panels (a) and (b) indicates the break-even condition in comparison to SSI and PL readout. The shaded regions represent  $1\sigma$  confidence intervals of the model, accounting for uncertainty in the measured single-shot SNR. (c) Total, time-averaged SNR as a function of integration bandwidth for each protocol. Lines are fits to the inverse square root of the bandwidth. Error bars in (c) are smaller than the markers.

tion (7.8) quantitatively captures the trade-off between these two quantities. The initialization time is given by

$$\tau_I = (\tau_{\text{pump}} + \tau_{\text{overhead}} + \tau_{\text{probe}})\bar{n}, \quad (7.9)$$

where  $\tau_{\text{pump}} = 0.5 \mu\text{s}$  is the duration of the 532 nm charge reset pump and  $\tau_{\text{overhead}} = 1.5 \mu\text{s}$  is the overhead in the initialization sequence comprised of the green AOM delay, singlet decay time, and  $\tau_{\text{delay}}$ . Note that  $\tau_I$  is an average quantity since equation (7.8) is assumed to be an ensemble average over many trials.

With a model describing the readout efficiency, we can numerically optimize equation (7.8) to determine the protocol parameters that maximize the readout efficiency for a given operation time. To assess the results in context of typical NV-center experiments, we compute and measure the baseline readout efficiency,  $\xi_{\text{baseline}}$ , corresponding to steady state initialization and traditional PL readout for different operation times. We then define

the speedup as the reduction in integration time required to achieve a fixed SNR when comparing a new technique to the baseline,

$$\text{Speedup} = \left( \frac{\xi}{\xi_{\text{baseline}}} \right)^2. \quad (7.10)$$

A speedup of unity defines the break-even time; the operation time at which it is equally efficient to use the enhanced technique over the baseline protocol.

Figure 25 presents the results of this optimization for four different scenarios: SSI with PL readout, RTI with PL readout, SSI with SCC readout, and RTI with SCC readout. The predicted and measured speedup curves for PL and SCC readout are shown in Figs. 25(a) and (b), respectively. For PL readout, we observe a break-even time for using the RTI of  $\sim 70 \mu\text{s}$ , and a maximum speedup of  $1.74 \pm 0.09$  for an operation time of 1 ms. Interestingly, we find that our full model always results in a choice of measurement parameters that make SCC more efficient than PL readout. RTI offers a further boost for operation times over  $30 \mu\text{s}$ , with a maximum observed speedup of  $20.8 \pm 1.2$  for  $\tau_O = 1 \text{ ms}$ . The measurements agree with the model prediction when accounting for the uncertainty in calibrating the single-shot SNR.

Figure 25(c) shows the total SNR as a function of integration bandwidths for each of the four techniques. Here, we have fixed the operation time to be  $500 \mu\text{s}$ . In each case, the total SNR scales with the inverse square root of bandwidth as expected. Of note is the integration bandwidth for which each technique achieves  $\langle \text{SNR} \rangle = 1$ , which represents the maximum frequency of environmental dynamics that can be resolved above the noise. The RTI protocol coupled with SCC readout offers the best performance for this operation time. In addition, Fig. 25(c) confirms that the optical pulse sequences required for RTI and SCC do not introduce any appreciable noise in the bandwidth we consider.

## 7.4. Discussion

NV-center quantum sensors stand to gain significant sensitivity improvements from using RTI protocols of the charge state. The largest speedup is realized for long operation times that approach 1 ms, which coincide with the typical requirements for spin relaxometry [6, 130] as well as dynamical decoupling sequences [100, 160]. The single NV center studied here exhibits a Hahn-echo  $T_2 = 800 \mu\text{s}$ . Explicitly accounting for the RTI and SCC overhead, our observed  $\xi$  corresponds to an estimated ac magnetic sensitivity of  $1.3 \text{ nT}/\text{Hz}^{1/2}$ . Other readout techniques used in quantum sensors, such as the nuclear-assisted method [7, 67], would also see similar signal-acquisition improvements due to RTI.

In many situations, the gains are likely to be even larger than we have demonstrated, since NV centers located in nanodiamonds or close to surfaces typically exhibit lower steady-state charge populations than those in bulk diamond [19, 79]. Using our model and assuming a 25%  $\text{NV}^-$  steady-state population, RTI would enable a factor-of-6 speedup for PL readout and a factor-of-75 speedup for SCC readout with an operation time of  $500 \mu\text{s}$ . In addition, these speedups persist across various photon collection efficiencies. As the collection efficiency is reduced, the break-even time for both PL and SCC readout increases slightly due to a reduced initialization efficiency, however the SNR improvement from SCC readout becomes larger, leading to the largest speedups at the lowest collection efficiencies. For high-collection-efficiency devices with saturated count rates approaching  $1 \text{ MCts s}^{-1}$ , the break-even time for PL readout is reduced to  $18 \mu\text{s}$ .

While we have focused on applications that require strict consideration of the overhead from initialization and readout, the techniques are directly applicable to situations in which initialization fidelity is prioritized over total measurement time. For example, the initialization error can be reduced by a further factor of 2 by increasing the threshold to 2 photons, and the delay error can be reduced by decreasing  $P_{\text{probe}}$ , which leads to  $F_{\text{NV}^-} = 99.4 \pm 0.1\%$  with  $\tau_I = 7 \text{ ms}$ . Such control over the charge state could facilitate precise measurements of the local electrostatic environment [19, 119], aid in the quantification of photon collection

efficiency for photonic devices [82], and improve the single-shot SNR for infrequent SCC measurements [87]. In addition, the fidelity associated with initializing, controlling, and measuring coupled nuclear spins [22, 33, 124] is intricately tied to the NV center's charge and spin purity and thus could be improved with RTI.

## 7.5. Conclusion

In conclusion, we demonstrated an efficient method for initializing the charge state of an NV center in real-time and assessed how this can be used to improve the efficiency of spin readout. Real-time control could be applied to other aspects of the NV center, such as projective initialization of nuclear spins [107] and increasing the spin state initialization fidelity through time-gating. In addition, this advanced control can be applied to other emerging solid-state spin defects, especially those which may have a high fidelity readout mechanism but a less-than-ideal spin or charge pumping transition.

## CHAPTER 8 : Conclusion and Future Directions

Without the ability to prepare and investigate a quantum system, the benefits of quantum coherence to sensing, communication, and computation are moot. In this thesis, I worked to improve the preparation and measurement capabilities of the diamond NV center, the prototypical solid-state defect qubit which can be used for quantum sensing at room temperature. This was largely achieved through the optical control and measurement of the defect's nonequilibrium orbital and charge dynamics. Central to this effort was the improved understanding of NV center charge dynamics under multi-color illumination and the formalization of quantitative spin-readout metrics. This thesis includes material adapted from manuscripts published in *Physical Review B* [78] and *ACS Nano* [79], a review article published in *Micromachines* [80], and work currently under review.

Improving spin readout performance is directly applicable to sensing applications. A significant push towards engineering dynamic surface functional groups on nanodiamonds that can extend and retract MRI contrast agents is underway [95]. These schemes attempt to correlate biochemical events in cells with the  $T_1$  of NV centers within the nanodiamonds, a prime candidate experiment for SCC readout. However, the largest performance improvements are for single NV centers within bulk crystals. Shallow implanted NV centers, which are often used for sensing [4, 129], can suffer from reduced spin coherence properties and initial charge fidelity. Materials science developments are quickly reducing the detrimental spin effects [51, 145, 155] yet the poor charge fidelity remains [19]. Deterministically initializing the charge state in shallow NV-center-based sensors will lead to improved sensitivity and throughput, especially when operating in scanning modes where two-dimensional magnetic images are desired.

Real-time control of the charge state of a single NV center at room temperature motivates the search for other properties that can be improved through classical feedback. One likely candidate is the spin initialization fidelity. Following pulsed excitation, the fluores-

cence decay exhibits a bi-exponential response, where the two time-scales correspond to the excited state spin lifetimes of 7 ns and 12 ns for  $|m_s| = 1$  and 0, respectively. Thus, the time of arrival of a photon following a pulse of excitation light contains some information about the spin state; more delayed photons signify a higher likelihood the defect is in the  $m_s = 0$  state. By heralding the start of an experiment on the detection of a photon in a time window  $> 7$  ns after the excitation pulse, the spin purity can be further enhanced above the 80-90% level quoted in the literature. While this process will be rare, it can be repeated rapidly to achieve a high purity spin state within tens to hundreds of microseconds. This improved spin initialization fidelity will benefit the development of nuclear registers, where the traditional swap-based initialization is limited by the electron spin purity [124, 160].

In a similar vein, higher layers of control can be implemented and explored. A common issue with  $^{13}\text{C}$  nuclear registers coupled to NV centers is the limited memory lifetime due to the NV center's  $T_1$  of  $\approx 5$  ms. A strategy to avoid this is to continuously pump the NV center with 532 nm illumination [116]. However, the NV center still resides in  $\text{NV}^0 \sim 25\%$  of the time, which has a very short  $T_1$  [172] and limits the memory lifetime. With real-time control of the charge state, the NV center could periodically be reset into the  $m_s = 0$  projection of  $\text{NV}^-$ , drastically reducing charge transitions during a storage attempt. This could further increase the nuclear memory lifetime towards the ensemble limit of a few hours at room temperature [162]. Nuclear registers in diamond at room temperature require initialization, as the thermal bath equally mixes the spin projections. Typically, an electron-state swap provides this initialization [22, 124, 138, 160]. However, quantum nondemolition (QND) measurements of nuclear spins [116, 124] are possible, and dynamical decoupling schemes have been demonstrated to also be QND, enabling single-shot readout of weakly coupled nuclear spins [107]. Real-time control is readily applicable to implement initialize-by-measurement through a QND readout, and coupled with the improved readout performance of SCC could help illuminate optimal dynamical decoupling schemes for QND and control of weakly coupled nuclear registers.

The field of experimental quantum information science is at a unique inflection point. Private industry is devoting significant resources and building large teams devoted to the development of quantum computation and quantum technology in general. At the same time, advanced experimental hardware capabilities are becoming more accessible to small research groups as electronic and photonic industries reduce barriers to entry and embrace the open-source movement. This thesis in particular, uses many advances in laser science, photon detection, and the ease of use of embedded computing. While the field may be entering the early stages of engineering and development, there remains a vast amount of quantum device physics to be explored. I'm excited to see the field progress from a scientific and engineering standpoint. In particular, the rapidly expanding toolbox provided by industry can help the scientific community answer, and hopefully illuminate new, fundamental questions in quantum information science and the respective physical platforms.

## APPENDIX A: Charge Dynamics Calibration

To calibrate the red charge dynamics, we fit measured photon distributions to the model previously described for different red powers. The readout duration is chosen such that  $t_R > \Gamma_{\text{Ion}}^{-1}$ , allowing for the effects of ionization to be observed. The readout duration does not need to be longer than the recombination rate, as it is given by

$$\Gamma_{\text{rec}} = \frac{P_-}{1 - P_-} \Gamma_{\text{ion}}. \quad (\text{A.1})$$

Due to the small recombination rate under red illumination, the steady state  $\text{NV}^-$  population is  $P_- = 1.15 \pm 0.07\%$ . This complicates measuring the charge dynamics as it is difficult to observe  $\text{NV}^-$  fluorescence during continuous red illumination. To overcome this, we implement a pump-probe scheme to determine the red charge dynamics. A  $10 \mu\text{s}$  green charge pump is followed by a variable power and duration red charge probe during which the number of photons are counted. This increases the average initial  $\text{NV}^-$  population to  $\approx 75\%$ . The results of the charge dynamics calibration are presented in SFigure 26. We fit all of the rates to their unsaturated form [8] due to the maximum power being well below saturation. The power-dependencies for the rates are as follows

$$\gamma_- = C_- P \quad (\text{A.2})$$

$$\gamma_0 = C_0 P + D \quad (\text{A.3})$$

$$\Gamma_{\text{Ion}} = C_{\text{Ion}} P^2 \quad (\text{A.4})$$

$$\Gamma_{\text{Rec}} = C_{\text{Rec}} P^2, \quad (\text{A.5})$$

where  $C_s$  is the rate scaling term for the  $s$  process and  $D$  is the dark count rate. The fit parameters are presented in Table 4. The agreement of the data with the fit model further supports the use of the unsaturated rate dependencies.

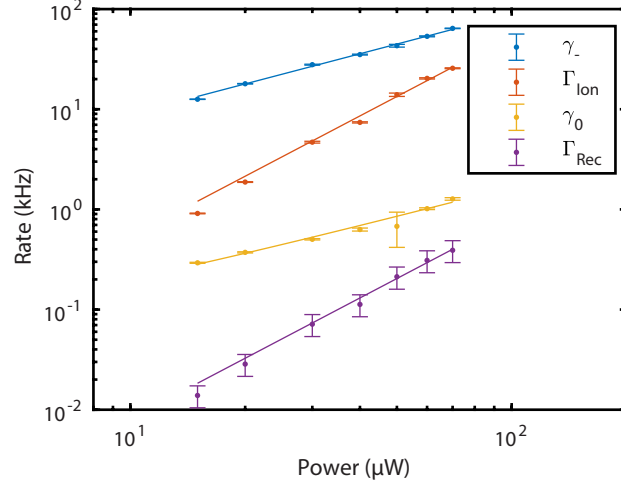


Figure 26: Red Charge Dynamics Calibration. The four measured rates and their associated power-dependence fits are presented.

Parameter	Value
$C_-$	$0.895 \pm 0.027 \text{ kHz } \mu\text{W}^{-1}$
$C_0$	$0.0163 \pm 0.0023 \text{ kHz } \mu\text{W}^{-1}$
$D$	$0.039 \pm 0.067 \text{ kHz}$
$C_{\text{Ion}}$	$5.36 \pm 0.27 \text{ Hz } \mu\text{W}^{-2}$
$C_{\text{Rec}}$	$0.082 \pm 0.0041 \text{ Hz } \mu\text{W}^{-2}$

Table 4: Fit results for the charge dynamics calibration.

## APPENDIX B: Measuring Spin Properties of a Single NV

The ground state spin properties were measured for both the steady state and real-time initialization protocols. First, we performed a Ramsey measurement on the NV center spin for both initialization techniques and measured the resulting spin population with traditional PL readout. The  $\pi/2$  pulses were detuned from resonance by 5 MHz to simplify the free evolution dynamics with the coupled  $^{14}\text{N}$  nuclear spin. The data were fit to the model

$$S = C + A * e^{-(\tau/T_2^*)^2} \sum_{k=-1}^1 \cos(2\pi(\delta - kA_{||}) + \phi), \quad (\text{B.1})$$

where  $C$  is the dephased signal,  $A$  is the amplitude of the signal,  $\tau$  is the evolution time,  $T_2^*$  is the inhomogenous dephasing timescale in  $\mu\text{s}$ ,  $\delta$  is the detuning from resonance in MHz,  $A_{||}$  is the parallel hyperfine coupling due to  $^{14}\text{N}$  in MHz, and  $\phi$  is a phase offset in radians. The data and fit results are depicted in SFig. 27(a, b) for the steady state and real-time initialization protocols, respectively. We find a steady state  $T_2^{*,SS} = 1.92 \pm 0.08\mu\text{s}$  and a real-time  $T_2^{*,RT} = 2.24 \pm 0.10\mu\text{s}$ , which corresponds to a 16% increase in spin dephasing time scale with the real-time initialization.

We then performed a Hahn-echo measurement for both of the initialization techniques. We initially identified the revivals due to the  $^{13}\text{C}$  spin bath and then measured the amplitudes of these revivals. The final  $\pi/2$  was applied around the  $+X$  and  $-X$  axes to allow for a differential signal, which can be seen in SFig. 27(c,d) for the steady state and real-time protocols, respectively. The resulting data are fit to the model

$$S = C + Ae^{-(\tau/T_2)^n}, \quad (\text{B.2})$$

where  $C$  is the offset,  $A$  is the amplitude,  $T_2$  is the echo coherence, and  $n$  is a freely varying parameter for the stretched exponential [150]. The steady state initialization results in a coherence time of  $T_2^{SS} = 830 \pm 28 \mu\text{s}$  and  $n = 2.98 \pm 0.42$ . The real time initialization results in a coherence time of  $T_2^{RT} = 852 \pm 81 \mu\text{s}$  and  $n = 2.85 \pm 1.03$ .

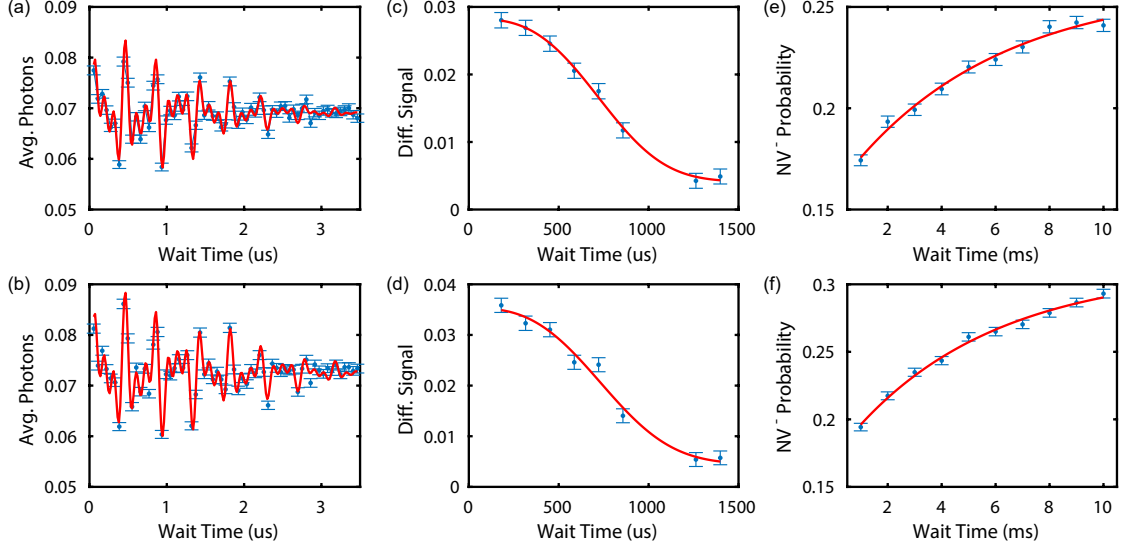


Figure 27: Measurements of Spin Properties. Measurements of  $T_2^*$  (a, b),  $T_2$  (c, d), and  $T_1$  (e, f) for the steady state and real-time initialization protocols, respectively.

We also measured the spin relaxation time for both initialization techniques. To do this, we first initialize into the  $m_s = 0$  projection and then record the SCC signal for various wait times. The data is presented in SFigure 27(e, f) for the steady state and real-time initialization protocols, respectively. The data in both cases is fit to a single exponential, which results in a spin relaxation time of  $T_1^{SS} = 5.6 \pm 1.2\text{ms}$  and  $T_1^{RT} = 5.3 \pm 0.9\text{ms}$  for the steady state and real-time protocols, respectively. Thus, there is no measurable difference between the two techniques.

## APPENDIX C: Estimating Spin Polarization with Pulsed Excitation

The ground state spin polarization of the NV center can be estimated by observing the relative amplitudes of the bi-exponential decay of a pulsed lifetime measurement [53, 138, 150]. By performing a fit to the lifetime response for both the optically polarized state, as well as after a calibrated  $\pi$ -pulse, one can estimate the initial  $m_s = 0$  population, assuming there is negligible radiative spin-mixing in the triplet manifold. However, to accurately fit the lifetime response, one must take into account the other spin projection ( $m_s = -1$  in our case), as well as pulse errors that manifest from the  $^{14}\text{N}$  hyperfine coupling. We now write down the three spin projection populations before

$$\begin{pmatrix} p_{-1}^b \\ p_{+1}^b \\ p_0^b \end{pmatrix} = \begin{pmatrix} \frac{1-p_0}{2} \\ \frac{1-p_0}{2} \\ p_0 \end{pmatrix}, \quad (\text{C.1})$$

and after the inversion pulse

$$\begin{pmatrix} p_{-1}^a \\ p_{+1}^a \\ p_0^a \end{pmatrix} = \begin{pmatrix} \frac{1-p_0}{2} \\ \frac{1-p_0}{2} \times (1 - F_\pi) + p_0 \times F_\pi \\ p_0 \times (1 - F_\pi) + \frac{1-p_0}{2} \times F_\pi \end{pmatrix}, \quad (\text{C.2})$$

where  $F_\pi$  is the fidelity of the  $\pi$ -pulse, which for this measurement with a Rabi driving frequency of  $\sim 5$  MHz is approximated to be 88%. The transient fluorescence response is then given by

$$f(t) = A_i (p_0^i e^{-\gamma_0 t} + (p_{+1}^i + p_{-1}^i) e^{-\gamma_1 t}) + C, \quad (\text{C.3})$$

where  $A_i$  is an overall amplitude,  $i = a, b$  represents whether this was after or before the inversion pulse, and  $\gamma_i$  is the excited state decay rate for the magnitude of the spin projection  $i$ , and  $C$  is a background term.

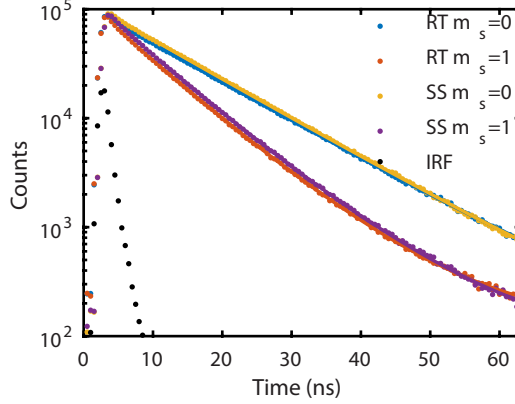


Figure 28: Lifetime Measurement of Spin Polarization. Transient response to a  $< 2.5$  ns red pulse for both the  $m_s = 0, 1$  spin states and the real-time (RT) and steady state (SS) initialization protocols. The measured instrument response function (IRF) is also displayed.

To perform the lifetime measurement, we initialize the NV center (either with the real-time or steady state protocol) and then measure the transient fluorescence response following a short excitation pulse with the red laser. The red laser can produce a pulse that is  $\sim 2$  ns in duration. The instrument response function (IRF) for this can be seen in Fig. 28. The data for both spin states and initialization protocols is presented in Fig. 28. We simultaneously fit Equation C.3, convolved with the IRF, to the before and after inversion pulse data sets. This helps reduce covariance between the excited state decay rates and the relative amplitudes and has been utilized in the literature [53]. We determine the excited state lifetimes to be  $\gamma_0^{-1} = 12.50 \pm 0.02$  ns, and  $\gamma_1^{-1} = 7.48 \pm 0.02$  ns. The spin polarization in  $m_s = 0$  ( $p_0$ ) is found to be  $91.5 \pm 0.7\%$  and  $94.4 \pm 0.7\%$  for the steady state and real-time initialization techniques, respectively.

It should be noted that since our excitation pulse is of similar magnitude to the fastest decay rate ( $\gamma_1^{-1} = 7.5$  ns), the spin polarization measured for the steady state technique may be slightly lower in actuality than measured, as the optical pumping process has begun during the non-instantaneous rise and fall time. Nonetheless, we still measure a difference in the spin polarizations for the two techniques, which agrees with the independent observation of the SNR differences mentioned in the main text.

## APPENDIX D: Spin Readout Noise Calculations

Following Eqn. (3.11), in order to calculate the spin-readout noise,  $\sigma_R$ , we must identify the signal's dependence on angle,  $\frac{\partial \langle S \rangle}{\partial \theta}$  and the standard deviation,  $\sigma_S$ . The standard deviation differs from the common form for Poisson or Binomial random variables due to the signal consisting of the *sum* of two random variables with different weights, and therefore we use the general expression for the variance,

$$\sigma_S^2 = \langle S^2 \rangle - \langle S \rangle^2. \quad (\text{D.1})$$

In this appendix, we derive expressions for  $\sigma_R$  corresponding to photon summation and thresholding signals.

### D.1. Photon Summation

For photon summation, the signal [Eqn. (3.10)] directly reflects the number of detected photons:

$$\langle S \rangle = \cos^2\left(\frac{\theta}{2}\right) \alpha_0 + \sin^2\left(\frac{\theta}{2}\right) \alpha_1. \quad (\text{D.2})$$

From this expression we can directly derive the signal variation,

$$\frac{\partial \langle S \rangle}{\partial \theta} = \frac{1}{2} \sin(\theta) (\alpha_0 - \alpha_1), \quad (\text{D.3})$$

and the expectation value of the signal squared,

$$\langle S^2 \rangle = \cos^2\left(\frac{\theta}{2}\right) (\alpha_0^2 + \alpha_0) + \sin^2\left(\frac{\theta}{2}\right) (\alpha_1^2 + \alpha_1). \quad (\text{D.4})$$

The latter expression uses the fact that the expected value of  $X^2$  from a Poisson distribution  $P(X; \lambda)$  with mean-value  $\lambda$  is  $\langle X^2 \rangle = \lambda^2 + \lambda$ . By combining Eqns. D.1, D.2, D.3, D.4 with

Eqn. 3.24 we arrive at the following general expression for the spin-readout noise:

$$\sigma_R^{\text{Photon}} = \frac{\sqrt{\frac{1}{4} \sin^2(\theta)(\alpha_0 - \alpha_1)^2 + \cos^2\left(\frac{\theta}{2}\right) \alpha_0 + \sin^2\left(\frac{\theta}{2}\right) \alpha_1}}{\frac{1}{2} \sin(\theta)(\alpha_0 - \alpha_1)}. \quad (\text{D.5})$$

Assuming an equally weighted superposition state ( $\theta = \pi/2$ ), Eqn. (D.5) reduces to the form reported in Eqn. (3.22) of the main text.

## D.2. Thresholding

In the case of thresholding, the signal results from the binary values of the measurement, where we assume that  $S = 1$  corresponds to the identification of the zero spin state [Eqn. (3.6)], and therefore

$$\langle S \rangle = \cos^2\left(\frac{\theta}{2}\right) p_{0|0} + \sin^2\left(\frac{\theta}{2}\right) p_{0|1}. \quad (\text{D.6})$$

As before, we use this expression to calculate the signal variation,

$$\frac{\partial \langle S \rangle}{\partial \theta} = \frac{1}{2} \sin(\theta)(p_{0|0} - p_{0|1}), \quad (\text{D.7})$$

and the mean of the signal squared,

$$\langle S^2 \rangle = \cos^2\left(\frac{\theta}{2}\right) p_{0|0} + \sin^2\left(\frac{\theta}{2}\right) p_{0|1}. \quad (\text{D.8})$$

These expressions yield the following general form for the spin-readout noise associated with thresholding,

$$\sigma_R^{\text{T}} = \frac{\sqrt{(\cos^2\left(\frac{\theta}{2}\right) p_{0|0} - \sin^2\left(\frac{\theta}{2}\right) p_{0|1})^2 + p_{0|0} (\cos^2\left(\frac{\theta}{2}\right) - 2 \cos^4\left(\frac{\theta}{2}\right)) + p_{0|1} (\sin^2\left(\frac{\theta}{2}\right) - \sin^4\left(\frac{\theta}{2}\right))}}{\frac{1}{2} \sin(\theta)(p_{0|0} - p_{0|1})}, \quad (\text{D.9})$$

Assuming an equally weighted superposition state ( $\theta = \pi/2$ ), Eqn. (D.9) reduces to the form reported in Eqn. (3.23) of the main text.

## APPENDIX E: Steady-State Charge Under Multi-Color Illumination

To model the steady-state charge distributions measured as a function of visible and NIR power in Figs. 14(b) and 15(a) of the main text, we compress the six-level system depicted in Fig. 3(e) of the main text into a two-level phenomenological model that accounts for the important nonlinear absorption terms that drive ionization/recombination in the presence of visible+NIR illumination. The terms we include involve at least one visible photon, as shown in Fig. 29, where  $G$  and  $R$  refer to the 532 nm and NIR power, respectively, and the coefficients  $\{C_{m,n}, D_{m,n}\}$  are defined in the main text. We do not include the multiphoton NIR-only transitions indicated in Fig. 15(e) since their rates (Fig. 15(d)) are much slower than for the corresponding visible+NIR processes at the same NIR power. This agrees with the many-orders-of-magnitude smaller cross-section's of virtual two photon absorption of both charge states compared to single-photon processes [85].

With these approximations, the master equation governing the charge-state evolution becomes

$$\begin{aligned} \frac{d}{dt} \begin{pmatrix} p_- \\ p_0 \end{pmatrix} &= \begin{pmatrix} -\gamma_{\text{Ion}} & \gamma_{\text{Rec}} \\ \gamma_{\text{Ion}} & -\gamma_{\text{Rec}} \end{pmatrix} \begin{pmatrix} p_- \\ p_0 \end{pmatrix} \\ &= \begin{pmatrix} -C_{2,0}G^2 - C_{1,1}GR - C_{1,2}GR^2 & D_{2,0}G^2 + D_{1,1}GR \\ C_{2,0}G^2 + C_{1,1}GR + C_{1,2}GR^2 & -D_{2,0}G^2 - D_{1,1}GR \end{pmatrix} \begin{pmatrix} p_- \\ p_0 \end{pmatrix}. \end{aligned} \quad (\text{E.1})$$

We solve for the steady-state solution, along with the condition the population must be conserved, and obtain expressions for  $p_-$  and  $p_0$ . Below we show the analysis for  $p_-$ , since it is directly related to the fits in the main text. The solution can be written in the form

$$p_- = \gamma \frac{1 + \alpha R}{1 + \delta R + \beta R^2}, \quad (\text{E.2})$$

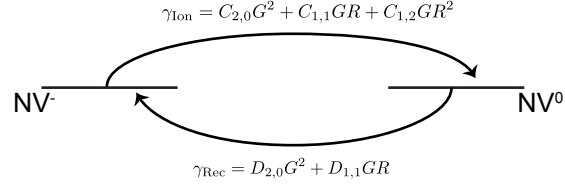


Figure 29: Schematic of the two-level rate-equation model used to fit the steady-state charge distributions in the main text. Rate coefficients correspond to the transitions presented in Fig. 15(e) of the main text.

where

$$\alpha = \frac{D_{1,1}}{D_{2,0}G}, \quad (\text{E.3a})$$

$$\beta = \frac{C_{1,2}}{(C_{2,0} + D_{2,0})G}, \quad (\text{E.3b})$$

$$\gamma = \frac{D_{2,0}}{D_{2,0} + C_{2,0}}, \quad (\text{E.3c})$$

$$\delta = \frac{C_{1,1} + D_{1,1}}{(C_{2,0} + D_{2,0})G}. \quad (\text{E.3d})$$

Note that  $\alpha$ ,  $\beta$ , and  $\delta$  scale with  $1/G$ . This is expected since they depend implicitly on the population of internal metastable states. In a full solution of the six-level model (not shown), the parameters  $\{C_{m,n}, D_{m,n}\}$  also depend non-trivially on  $R$  and  $G$  since they account for both the (constant) absorption cross section's of various processes and the (power-dependent) occupation probabilities of the levels in the model. Nonetheless, it is a reasonable approximation to treat them as constant parameters across the range of powers considered here, particularly as discussed above when multiphoton NIR-only transitions are not playing a major role.

To fit the data in Figs. 14(b) and 15(a) of the main text, the 4 parameters ( $\alpha, \beta, \gamma, \delta$ ) are allowed to vary independently. Note that even 592 nm light does not excite  $\text{NV}^0$  to lowest

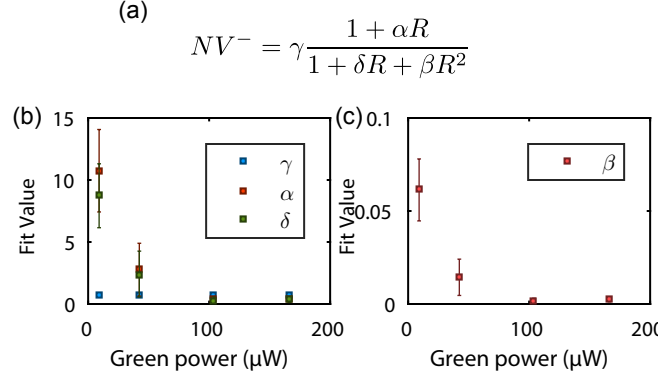


Figure 30: Results of the Phenomenological model fit (a) The actual fit equation we use, with simplified coefficients (b) the first three coefficients (c) The last coefficient, which is about two orders of magnitude smaller (signifying the weakness of the singlet ionization mechanism). Error bars are 65% confidence.

order, at room temperature there is non-zero absorption due to an anti-Stokes shift [8], so the recombination coefficients  $D_{2,0}$  and  $D_{1,1}$  are nonzero even for the fits to the 592 nm+NIR data in Fig. 3(a).

In Fig. 14 of the main text, we swept  $R$  for over four different settings of  $G$ , varying across above the PL saturation value of  $P_{\text{sat}} = 42 \mu\text{W}$ . We independently fit the results of four green power slices using this model (only three are shown in the main text for clarity but all are presented here). The best-fit parameters are plotted in Fig. 30. We observe the expected scaling with  $1/G$  in the best-fit parameters  $\alpha$ ,  $\beta$ , and  $\delta$ , justifying our approximation of fixing the remaining rate coefficients in the model.

Through this parameterization, we have reduced the number of free parameters in the model from five ( $C_{1,1}$ ,  $D_{1,1}$ ,  $C_{2,0}$ ,  $D_{2,0}$ , and  $C_{1,2}$ ) to four that uniquely control the model's dependence on  $R$ . From the fit results, we can back out the relative strengths of many of the underlying rate coefficients. For example, the best-fit value of  $\gamma$  corresponds to the steady-state value of  $p_-$  under visible illumination only. For 532 nm illumination, the observed value of  $p_- = 78\%$  therefore implies that  $R_{1,1}/C_{1,1} = 3.5$ .

Similarly, the ratio  $\alpha/\delta$  can be written in the form

$$\frac{\alpha}{\delta} = \frac{D_{1,1}}{(D_{1,1} + C_{1,1})} \frac{(D_{2,0} + C_{2,0})}{D_{2,0}} = \frac{D_{1,1}}{(D_{1,1} + C_{1,1})} \frac{1}{\gamma}. \quad (\text{E.4})$$

We can therefore calculate the relative strength of the NIR-assisted ionization/recombination transitions from the best-fit values of  $\alpha$ ,  $\gamma$ , and  $\delta$ . We find  $D_{1,1}/C_{1,1} = 6.69 \pm 0.04$ . The fact that this ratio is larger than for the analogous process for two 532 nm photons intuitively explains the initial enhancement of  $p_-$  as a function of  $R$ , as recombination becomes even more likely than ionization.

Finally, We can extract the relative strength of two-NIR-photon singlet ionization is compared to the competing process for excited state recombination in a similar manner:

$$\frac{\beta}{\alpha} = \frac{C_{1,2}}{C_{2,0} + D_{2,0}} \frac{D_{2,0}}{D_{1,1}} = \frac{C_{1,2}}{D_{1,1}} \gamma, \quad (\text{E.5})$$

from which we find  $C_{1,2}/D_{1,1} = 7.4 \pm 0.3 \times 10^{-3}$ . This much smaller strength is not surprising considering the small optical cross section of the singlet. Nonetheless, singlet ionization plays a dominant role in the charge-state dynamics at high NIR powers due to the quadratic scaling with  $R^2$ .

## APPENDIX F: Population Transfer Matrix Model for Spin-to-Charge Conversion

To quantify the performance of the multi-SCC process, we use a six level model taking into account the  $m_s = 0, -1$  spin sublevels of the  $NV^-$  triplet, the metastable single ground state, and a single  $NV^0$  state. We ignore the singlet excited state since its  $\sim 1$  ns lifetime is both much shorter than the metastable singlet ground state and much longer than the  $\sim 10$  ps duration of a NIR pulse. Similarly, we ignore the  $NV^0$  excited state since its dynamics are implicit in the values of the recombination coefficients.

A depiction of these levels is presented in Fig. 31. A single SCC step is broken into three distinct regions. The first corresponds to the excitation of the triplet ((I) in Fig. 31), which also allows for ionization. While the physical ionization process is sequential two-photon absorption through the triplet excited states (3 and 4), we are only interested in the resulting distribution of populations between the triplet and  $NV^0$  manifolds, so we combine the sequential absorption into a single step. The system is then allowed to relax either to the ground state or the singlet manifold through the ISC, which we define by the branching ratios  $k_{35}$  and  $k_{45}$  for the probability of  $m_s = 0$  and  $m_s = \pm 1$  respectively to decay into the singlet (Fig. 31(II)). As in step (I), we ignore the intermediate dynamics of the singlet excited state since it relaxes on a much faster timescale ( $\sim 1$  ns) than the metastable singlet ground-state lifetime ( $\sim 200$  ns).

In the ideal case, the system would only be excited once, however we cannot guarantee this due to long AOM turn-on times. Therefore the effective ISC transition rates we measure likely correspond to a few optical cycles. After the triplet excited state has fully decayed, we attempt to ionize the singlet with a train of NIR pulses, which we treat as a single step (Fig. 31(III)). Any population that is not ionized decays into the ground state, with the branching ratios  $k_{51}$  and  $k_{52}$ .

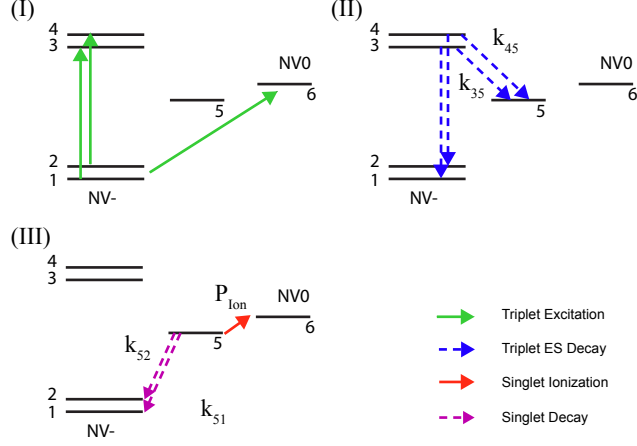


Figure 31: Outline of the 6-level population transfer matrix model for multi-SCC (I) excite the triplet ground state. (II) Allow the excited state to decay. (III) Attempt to ionize the singlet and decay to the ground state. The probability is conserved leaving any state.

To construct the master equation, we define a population vector

$$p = \begin{pmatrix} p1 \\ p2 \\ p3 \\ p4 \\ p5 \\ p6 \end{pmatrix}, \quad (\text{F.1})$$

and matrix representations for the steps I–III:

$$M_I = \begin{pmatrix} 0 & 0 & 0 & 0 & 0 & 0 \\ 0 & 0 & 0 & 0 & 0 & 0 \\ P_{exc} & 0 & 0 & 0 & 0 & 0 \\ 0 & P_{exc} & 0 & 0 & 0 & 0 \\ 0 & 0 & 0 & 0 & 0 & 0 \\ P_{ion} & P_{ion} & 0 & 0 & 0 & 1 \end{pmatrix}, \quad (\text{F.2})$$

$$M_{\text{II}} = \begin{pmatrix} 1 & 0 & 1 - k_{35} & 0 & 0 & 0 \\ 0 & 1 & 0 & 1 - k_{45} & 0 & 0 \\ 0 & 0 & 0 & 0 & 0 & 0 \\ 0 & 0 & 0 & 0 & 0 & 0 \\ 0 & 0 & k_{35} & k_{45} & 0 & 0 \\ 0 & 0 & 0 & 0 & 0 & 1 \end{pmatrix}, \quad (\text{F.3})$$

$$M_{\text{III}} = \begin{pmatrix} 1 & 0 & 0 & 0 & k_{51} & 0 \\ 0 & 1 & 0 & 0 & k_{52} & 0 \\ 0 & 0 & 0 & 0 & 0 & 0 \\ 0 & 0 & 0 & 0 & 0 & 0 \\ 0 & 0 & 0 & 0 & 0 & 0 \\ 0 & 0 & 0 & 0 & P_{\text{sing}} & 0 \end{pmatrix}. \quad (\text{F.4})$$

Note that the columns must sum to 1 to conserve probability, and that only the states 1, 2, and 6 are stable (and thus never decay). The expected populations after an arbitrary number of repeats,  $N$ , are therefore given by

$$p_{\text{final}} = (M_{\text{III}} \times M_{\text{II}} \times M_{\text{I}})^N p_0, \quad (\text{F.5})$$

and the first two elements of  $p_{\text{final}}$  constitute the resulting  $\text{NV}^-$  population.

We perform a joint fit of this model to both spin-initialization datasets from Fig. 4(c) in the main text, accounting also for incomplete spin and charge initialization in the definition of  $p_0$ . The charge-initialization is known directly from calibration measurements, while the spin-initialization remains a free parameter. Separate measurements of the green shelving pulse alone fix the ionization probability during excitation to  $P_{\text{ion}} = 0.5\%$ . This leaves six free parameters in the joint fit, whose best-fit values and uncertainties are listed in Table 5.

Table 5: Best-fit parameters corresponding to the multi-SCC measurements in Fig. 16(c) of the main text.

$NV^0$ init	$k_{35}$	$k_{45}$
$0.04 \pm 0.013$	$0.033 \pm 0.07$	$0.25 \pm 0.04$
$P_{\text{sing}}$	$k_{51}/k_{52}$	$m_s = 0$ init
$0.32 \pm 0.04$	$2.26 \pm 0.01$	$0.85 \pm 0.06$

## APPENDIX G: Real-Time Control Hardware

Critical to this experiment is the ability for our timing electronics (AWG520, Tektronix) to be able to exit an infinite loop asynchronously and move on to a different timing sequence conditioned on an external signal. The Xilinx Artix-7 FPGA is physically interfaced with a Digital ARTY development board and perform the real-time counting and logic necessary. This platform exposes the I/O headers to communicate with the digital logic and upload the board firmware. We define the digital logic in Verilog and use the Vivado IDE to build and communicate the instructions to the board. All of our counting, both for initialization and readout, is handled by the FPGA. Given the type of counting, the FPGA either triggers an event to break out of the initialization loop or forwards the number of counts and the trial number to the DAQ via 12 digital lines after a readout has finished. The core functionality of the real-time control can be explained by three modules: control, SPAD counter, and trial counter. The control module receives information via digital lines from the AWG that governs when the FPGA should be counting, what threshold to check against, resetting registers, and whether an event should be triggered (for initialization) or if the threshold should be ignored (for readout). The SPAD counter is a 6-bit counter that records the number of rising edges coming from the SPAD and handles resetting the number of counts for a given task. The trial counter is similar to the SPAD counter, but it counts rising edges originating from the AWG. The two counters are output as a 12-bit register that the DAQ samples following the end of an experiment. This dual-counter strategy allows us to run multiple trials of a given experiment in an interleaved fashion. An example Verilog file that was used in our experiment has been posted publicly on GitHub: <https://github.com/penn-qel/real-time-nv-charge-control>.

## BIBLIOGRAPHY

- [1] Abragam, A. 1965, *Principles of Nuclear Magnetism* (Oxford University Press)
- [2] Acosta, V. M., Jarmola, A., Bauch, E., & Budker, D. 2010, *Phys. Rev. B*, 82, 201202
- [3] Andrich, P., de las Casas, C. F., Liu, X., Bretscher, H. L., Berman, J. R., Heremans, F. J., Nealey, P. F., & Awschalom, D. D. 2017, *npj Quantum Inf.*, 3, 28
- [4] Appel, P., Neu, E., Ganzhorn, M., Barfuss, A., Batzer, M., Gratz, M., Tschpe, A., & Maletinsky, P. 2016, *Rev. Sci. Instrum.*, 87, 063703
- [5] Arcizet, O., Jacques, V., Siria, A., Poncharal, P., Vincent, P., & Seidelin, S. 2011, *Nat. Phys.*, 7, 879
- [6] Ariyaratne, A., Bluvstein, D., Myers, B. A., & Jayich, A. C. B. 2018, *Nat. Commun.*, 9, 2406
- [7] Aslam, N. et al. 2017, *Science*, 357, 67
- [8] Aslam, N., Waldherr, G., Neumann, P., Jelezko, F., & Wrachtrup, J. 2013, *New Jour. Phys.*, 15, 013064
- [9] Atatüre, M., Englund, D., Vamivakas, N., Lee, S.-Y., & Wrachtrup, J. 2018, *Nat. Rev. Mater.*, 3, 38
- [10] Awschalom, D. D., Bassett, L. C., Dzurak, A. S., Hu, E. L., & Petta, J. R. 2013, *Science*, 339, 1174
- [11] Awschalom, D. D., Hanson, R., Wrachtrup, J., & Zhou, B. B. 2018, *Nat. Photonics*, 12, 516
- [12] Bar-Gill, N., Pham, L. M., Jarmola, A., Budker, D., & Walsworth, R. L. 2013, *Nat. Commun.*, 4, 1743
- [13] Barry, J. F., Turner, M. J., Schloss, J. M., Glenn, D. R., Song, Y., Lukin, M. D., Park, H., & Walsworth, R. L. 2016, *Proc. Natl. Acad. Sci. U.S.A.*, 113, 14133
- [14] Batalov, A. et al. 2009, *Phys. Rev. Lett.*, 102, 195506
- [15] —. 2008, *Phys. Rev. Lett.*, 100, 077401
- [16] Bernien, H. et al. 2013, *Nature*, 497, 86
- [17] Berthel, M., Mollet, O., Dantelle, G., Gacoin, T., Huant, S., & Drezet, A. 2015, *Phys. Rev. B*, 91, 035308

- [18] Blok, M. S., Bonato, C., Markham, M. L., Twitchen, D. J., Dobrovitski, V. V., & Hanson, R. 2014, *Nat. Phys.*, 10, 189
- [19] Bluvstein, D., Zhang, Z., & Jayich, A. C. B. 2019, *Phys. Rev. Lett.*, 122, 76101
- [20] Bogdanov, S. et al. 2017, *Phys. Rev. B*, 96, 035146
- [21] Boss, J. M., Cujia, K. S., Zopes, J., & Degen, C. L. 2017, *Science*, 356, 837
- [22] Bradley, C. E. et al. 2019, *Phys. Rev. X*, 9, 031045
- [23] Brenneis, A. et al. 2015, *Nat. Nanotechnol.*, 10, 135
- [24] Brown, K. R., Kim, J., & Monroe, C. 2016, *npj Quantum Inf.*, 2, 16034
- [25] Buckley, B. B., Fuchs, G. D., Bassett, L. C., & Awschalom, D. D. 2010, *Science*, 330, 1212
- [26] Bundy, F. P., Hall, H. T., Strong, H. M., & Wentworf, R. H. 1955, *Nature*, 176, 51
- [27] Casola, F., van der Sar, T., & Yacoby, A. 2018, *Nat. Rev. Mater.*, 3, 17088
- [28] Chang, Y.-R. et al. 2008, *Nat. Nanotechnol.*, 3, 284
- [29] Chen, X.-D., Zhou, L.-M., Zou, C.-L., Li, C.-C., Dong, Y., Sun, F.-W., & Guo, G.-C. 2015, *Phys. Rev. B*, 92
- [30] Childress, L., Gurudev Dutt, M. V., Taylor, J. M., Zibrov, A. S., Jelezko, F., Wrachtrup, J., Hemmer, P. R., & Lukin, M. D. 2006, *Science*, 314, 281
- [31] Clark, C. D. & Norris, C. A. 1971, *J. Phys. Condens. Matter C*, 4, 2223
- [32] Clerk, A. A., Devoret, M. H., Girvin, S. M., Marquardt, F., & Schoelkopf, R. J. 2010, *Rev. Mod. Phys.*, 82, 1155
- [33] Cramer, J. et al. 2016, *Nat. Commun.*, 7, 11526
- [34] D’Anjou, B. & Coish, W. A. 2014, *Phys. Rev. A*, 89, 12313
- [35] D’Anjou, B., Kuret, L., Childress, L., & Coish, W. A. 2016, *Phys. Rev. X*, 6, 011017
- [36] Dantelle, G. et al. 2010, *J. Lumin.*, 130, 1655
- [37] Davies, G. & Hamer, M. F. 1976, *Proc. Royal Soc. Lond. A*, 348, 285
- [38] de Lange, G., Wang, Z. H., Ristè, D., Dobrovitski, V. V., & Hanson, R. 2010, *Science*, 330, 60
- [39] Degen, C. L., Reinhard, F., & Cappellaro, P. 2017, *Rev. Mod. Phys.*, 89, 35002

- [40] Dhomkar, S., Henshaw, J., Jayakumar, H., & Meriles, C. 2016, *Sci. Adv.*, 2, e1600911
- [41] DiVincenzo, D. P. 2000, *Fortsch. Phys.*, 48, 771
- [42] Doherty, M. W., Dolde, F., Fedder, H., Jelezko, F., Wrachtrup, J., Manson, N. B., & Hollenberg, L. C. L. 2012, *Phys. Rev. B*, 85, 205203
- [43] Doherty, M. W., Manson, N. B., Delaney, P., & Hollenberg, L. C. L. 2011, *New Jour. Phys.*, 13, 025019
- [44] Doherty, M. W., Manson, N. B., Delaney, P., Jelezko, F., Wrachtrup, J., & Hollenberg, L. C. L. 2013, *Phys. Rep.*, 528, 1
- [45] Doherty, M. W., Meriles, C. A., Alkauskas, A., Fedder, H., Sellars, M. J., & Manson, N. B. 2016, *Phys. Rev. X*, 6, 041035
- [46] Doi, Y. et al. 2016, *Phys. Rev. B*, 93, 81203
- [47] —. 2014, *Phys. Rev. X*, 4, 11057
- [48] du Preez, L. 1965, PhD thesis, University of Witwaters
- [49] Dutt, M. V. G. et al. 2007, *Science*, 316, 1312
- [50] Elzerman, J. M., Hanson, R., Willems van Beveren, L. H., Witkamp, B., Vandersypen, L. M. K., & Kouwenhoven, L. P. 2004, *Nature*, 430, 431
- [51] Fávoro de Oliveira, F. et al. 2017, *Nat. Commun.*, 8, 15409
- [52] Field, J. E. 2012, *Rep. Prog. Phys.*, 75, 126505
- [53] Fuchs, G., Dobrovitski, V., Toyli, D., Heremans, F., Weis, C., Schenkel, T., & Awschalom, D. 2010, *Nat. Phys.*, 6, 668
- [54] Fuchs, G. D., Dobrovitski, V. V., Toyli, D. M., Heremans, F. J., & Awschalom, D. D. 2009, *Science*, 326, 1520
- [55] Gaebel, T. et al. 2006, *Appl. Phys. B*, 82, 243
- [56] Galbraith, W. 1955, *J. Cell Sci.*, 3, 285
- [57] Gali, A. 2009, *Phys. Rev. B*, 79, 235210
- [58] Gambetta, J. M., Chow, J. M., & Steffen, M. 2017, *npj Quantum Inf.*, 3, 2
- [59] Geiselmann, M., Marty, R., de Abajo, F. J., & Quidant, R. 2013, *Nat. Phys.*, 9, 785
- [60] Goldman, M. L., Doherty, M. W., Sipahigil, A., Yao, N. Y., Bennett, S. D., Manson, N. B., Kubanek, A., & Lukin, M. D. 2015, *Phys. Rev. B*, 91, 165201

- [61] Goldman, M. L. et al. 2015, *Phys. Rev. Lett.*, 114, 145502
- [62] Gross, I. et al. 2017, *Nature*, 549, 252
- [63] Grotz, B. et al. 2012, *Nat. Commun.*, 3, 729
- [64] Gruber, A., Dräbenstedt, A., Tietz, C., Fleury, L., Wrachtrup, J., & von Borczyskowski, C. 1997, *Science*, 276, 2012
- [65] Gulka, M. et al. 2017, *Phys. Rev. Appl.*, 7, 044032
- [66] Gupta, A., Hacquebard, L., & Childress, L. 2016, *J. Opt. Soc. Am. B*, 33, B28
- [67] Häberle, T., Oeckinghaus, T., Schmid-Lorch, D., Pfender, M., de Oliveira, F. F., Momenzadeh, S. A., Finkler, A., & Wrachtrup, J. 2017, *Rev. Sci. Instrum.*, 88, 13702
- [68] Hacquebard, L. & Childress, L. 2018, *Phys. Rev. A*, 97, 63408
- [69] Hadden, J. P., Harrison, J. P., Stanley-Clarke, A. C., Marseglia, L., Ho, Y.-L. D., Patton, B. R., O'Brien, J. L., & Rarity, J. G. 2010, *Appl. Phys. Lett.*, 97, 241901
- [70] Hall, L. T., Kehayias, P., Simpson, D. A., Jarmola, A., Stacey, A., Budker, D., & Hollenberg, L. C. L. 2016, *Nat. Commun.*, 7, 10211
- [71] Han, K. Y., Kim, S. K., Eggeling, C., & Hell, S. W. 2010, *Nano Lett.*, 10, 3199
- [72] Hanson, R., Dobrovitski, V., Feiguin, A., Gywat, O., & Awschalom, D. 2008, *Science*, 320, 352
- [73] Harty, T., Allcock, D., Ballance, C., Guidoni, L., Janacek, H., Linke, N., Stacey, D., & Lucas, D. 2014, *Phys. Rev. Lett.*, 113, 220501
- [74] Havlik, J. et al. 2013, *Nanoscale*, 5, 3208
- [75] Heiss, D., Jovanov, V., Bichler, M., Abstreiter, G., & Finley, J. J. 2008, *Phys. Rev. B*, 77, 235442
- [76] Hellen, E. H. & Axelrod, D. 1987, *J. Opt. Soc. Am. B*, 4, 337
- [77] Hensen, B. et al. 2015, *Nature*, 526, 682
- [78] Hopper, D. A., Grote, R. R., Exarhos, A. L., & Bassett, L. C. 2016, *Phys. Rev. B*, 94, 241201
- [79] Hopper, D. A., Grote, R. R., Parks, S. M., & Bassett, L. C. 2018, *ACS Nano*, 12, 4678
- [80] Hopper, D. A., Shulevitz, H. J., & Bassett, L. C. 2018, *Micromachines*, 9, 437

- [81] Hrubesch, F. M., Braunbeck, G., Stutzmann, M., Reinhard, F., & Brandt, M. S. 2017, *Phys. Rev. Lett.*, 118, 037601
- [82] Huang, T.-Y. et al. 2019, *Nat. Commun.*, 10, 2392
- [83] Humphreys, P. C., Kalb, N., Morits, J. P. J., Schouten, R. N., Vermeulen, R. F. L., Twitchen, D. J., Markham, M., & Hanson, R. 2018, *Nature*, 558, 268
- [84] Huxter, V. M., Oliver, T. A. A., Budker, D., & Fleming, G. R. 2013, *Nat. Phys.*, 9, 744
- [85] Ivanov, I., Li, X., Dolan, P., & Gu, M. 2013, *Opt. Lett.*, 34, 1358
- [86] Jamali, M., Gerhardt, I., Rezai, M., Frenner, K., Fedder, H., & Wrachtrup, J. J. 2014, *Rev. Sci. Instrum.*, 85
- [87] Jaskula, J.-C., Shields, B. J., Bauch, E., Lukin, M. D., Trifonov, A. S., & Walsworth, R. L. 2019, *Phys. Rev. Appl.*, 11, 64003
- [88] Jayakumar, H. et al. 2016, *Nat. Commun.*, 7, 12660
- [89] Jelezko, F., Gaebel, T., Popa, I., Gruber, A., & Wrachtrup, J. 2004, *Phys. Rev. Lett.*, 92, 76401
- [90] Ji, P. & Dutt, M. V. G. 2016, *Phys. Rev. B*, 94, 24101
- [91] Jiang, L. et al. 2009, *Science*, 326, 267
- [92] Kalb, N., Humphreys, P. C., Slim, J. J., & Hanson, R. 2018, *Phys. Rev. A*, 97, 62330
- [93] Kamo, M., Sato, Y., Matsumoto, S., & Setaka, N. 1983, *J. Cryst. Growth*, 62, 642
- [94] Karaveli, S. et al. 2016, *Proc. Natl. Acad. Sci. U.S.A.*, 113, 3938
- [95] Kaufmann, S. et al. 2013, *Proc. Natl. Acad. Sci. U.S.A.*, 110, 10894
- [96] Kehayias, P. et al. 2013, *Phys. Rev. B*, 88, 165202
- [97] Knowles, H. S., Kara, D. M., & Atatüre, M. 2014, *Nat. Mater.*, 13, 21
- [98] —. 2016, *Phys. Rev. Lett.*, 117, 100802
- [99] —. 2017, *Phys. Rev. B*, 96, 115206
- [100] Kolkowitz, S., Unterreithmeier, Q. P., Bennett, S. D., & Lukin, M. D. 2012, *Phys. Rev. Lett.*, 109, 137601
- [101] Kucsko, G., Maurer, P. C., Yao, N. Y., Kubo, M., Noh, H. J., Lo, P. K., Park, H., & Lukin, M. D. 2013, *Nature*, 500, 54

- [102] Kurin, R. 2006, *The Hope Diamond* (Smithsonian Books)
- [103] Lai, N. D., Faklaris, O., Zheng, D., Jacques, V., Chang, H.-C., Roch, J.-F., & Treussart, F. 2013, *New Jour. Phys.*, 15, 33030
- [104] Le Sage, D. et al. 2013, *Nature*, 496, 486
- [105] Lee, C. L., Gu, E., Dawson, M. D., Friel, I., & Scarsbrook, G. A. 2008, *Diam. Relat. Mater.*, 17, 1292
- [106] Liaugaudas, G., Davies, G., Suhling, K., Khan, R. U. A., & Evans, D. J. F. 2012, *J. Phys. Condens. Matter*, 24, 435503
- [107] Liu, G.-Q. et al. 2017, *Phys. Rev. Lett.*, 118, 150504
- [108] Loubser, J. H. N. & van Wyk, J. A. 1977, *Diam. Res.*, 11
- [109] —. 1978, *Rep. Prog. Phys.*, 41, 1201
- [110] Lovchinsky, I. et al. 2017, *Science*, 355, 503
- [111] —. 2016, *Science*, 351, 836
- [112] Magesan, E., Gambetta, J. M., Córcoles, A., & Chow, J. M. 2015, *Phys. Rev. Lett.*, 114, 200501
- [113] Manson, N. & Harrison, J. 2005, *Diam. Relat. Mater.*, 14, 1705
- [114] Manson, N. B., Harrison, J. P., & Sellars, M. J. 2006, *Phys. Rev. B*, 74, 104303
- [115] Marseglia, L. et al. 2011, *Appl. Phys. Lett.*, 98, 14
- [116] Maurer, P. C. et al. 2012, *Science*, 336, 1283
- [117] Maze, J. R., Gali, A., Togan, E., Chu, Y., Trifonov, A., Kaxiras, E., & Lukin, M. D. 2011, *New Jour. Phys.*, 13, 025025
- [118] McDonough, R. N. & Whalen, A. D. 1995, *Detection of Signals in Noise* (Academic Press)
- [119] Mittiga, T. et al. 2018, *Phys. Rev. Lett.*, 121, 246402
- [120] Mizuochi, N. et al. 2009, *Phys. Rev. B*, 80, 5
- [121] Mochalin, V. N., Shenderova, O., Ho, D., & Gogotsi, Y. 2012, *Nat. Nanotechnol.*, 7, 11
- [122] Morello, A. et al. 2010, *Nature*, 467, 687

- [123] Neukirch, L. P., Gieseler, J., Quidant, R., Novotny, L., & Vamivakas, A. N. 2013, *Opt. Lett.*, 38, 2976
- [124] Neumann, P., Beck, J., Steiner, M., Rempp, F., Fedder, H., Hemmer, P. R., Wrachtrup, J., & Jelezko, F. 2010, *Science*, 329, 542
- [125] Neumann, P. et al. 2009, *New Jour. Phys.*, 11, 13017
- [126] —. 2009, *New Jour. Phys.*, 11, 013017
- [127] —. 2010, *Nat. Phys.*, 6, 249
- [128] Nielsen, M. A. & Chuang, I. 2000, *Quantum computation and quantum communication* (Cambridge University Press, Cambridge)
- [129] Pelliccione, M., Jenkins, A., Ovartchaiyapong, P., Reetz, C., Emmanuelidu, E., Ni, N., & Bleszynski Jayich, A. C. 2016, *Nat. Nanotechnol.*, 11, 700
- [130] Pelliccione, M., Myers, B. A., Pascal, L. M. A., Das, A., & Bleszynski Jayich, A. C. 2014, *Phys. Rev. Appl.*, 2, 054014
- [131] Petrakova, V., Rehor, I., Stursa, J., Ledvina, M., Nesladek, M., & Cigler, P. 2015, *Nanoscale*, 7, 12307
- [132] Pfaff, W., Taminiiau, T. H., Robledo, L., Bernien, H., Markham, M., Twitchen, D. J., & Hanson, R. 2013, *Nat. Phys.*, 9, 29
- [133] Pfender, M. et al. 2017, *Nano Lett.*, 17, 5931
- [134] —. 2019, *Nat. Commun.*, 10, 594
- [135] Plakhotnik, T., Moerner, W., Palm, V., & Wild, U. P. 1995, *Opt. Commun.*, 114, 83
- [136] Rendler, T., Neburkova, J., Zemek, O., Kotek, J., Zappe, A., Chu, Z., Cigler, P., & Wrachtrup, J. 2017, *Nat. Commun.*, 8, 14701
- [137] Robledo, L., Bernien, H., Van Der Sar, T., & Hanson, R. 2011, *New Jour. Phys.*, 13, 025013
- [138] Robledo, L., Childress, L., Bernien, H., Hensen, B., Alkemade, P. F. A., & Hanson, R. 2011, *Nature*, 477, 574
- [139] Rogers, L. J., McMurtrie, R. L., Sellars, M. J., & Manson, N. B. 2009, *New Jour. Phys.*, 11, 063007
- [140] Ronald, S. 2004, *The Sancy blood diamond: power, greed, and the cursed history of one of the world's most coveted gems* (John Wiley & Sons, Inc.)
- [141] Rondin, L. et al. 2010, *Phys. Rev. B*, 82, 115449

- [142] Rondin, L., Tetienne, J. P., Hingant, T., Roch, J. F., Maletinsky, P., & Jacques, V. 2014, *Rep. Prog. Phys.*, 77, 56503
- [143] Rondin, L., Tetienne, J. P., Rohart, S., Thiaville, A., Hingant, T., Spinicelli, P., Roch, J. F., & Jacques, V. 2013, *Nat. Commun.*, 4, 2279
- [144] Ryan, C. A., Hodges, J. S., & Cory, D. G. 2010, *Phys. Rev. Lett.*, 105, 200402
- [145] Sangtawesin, S. et al. 2019, *Phys. Rev. X*, 9, 031052
- [146] Schirhagl, R., Chang, K., Loretz, M., & Degen, C. L. 2014, *Annu. Rev. Phys. Chem.*, 65, 83
- [147] Schmid-Lorch, D., Haberle, T., Reinhard, F., Zappe, A., Slota, M., Bogani, L., Finkler, A., & Wrachtrup, J. 2015, *Nano Lett.*, 15, 4942
- [148] Schmitt, S. et al. 2017, *Science*, 356, 832
- [149] Schröder, T. et al. 2016, *J. Opt. Soc. Am. B*, 33, B65
- [150] Shields, B. J., Unterreithmeier, Q. P., de Leon, N. P., Park, H., & Lukin, M. D. 2015, *Phys. Rev. Lett.*, 114, 136402
- [151] Silverstone, J. W., Bonneau, D., O'Brien, J. L., & Thompson, M. G. 2016, *IEEE J. Sel. Top. Quantum Electron.*, 22, 390
- [152] Siyushev, P., Pinto, H., Vörös, M., Gali, A., Jelezko, F., & Wrachtrup, J. 2013, *Phys. Rev. Lett.*, 110, 167402
- [153] Smeltzer, B., McIntyre, J., & Childress, L. 2009, *Phys. Rev. A*, 80, 050302
- [154] Spiess, A.-N. & Neumeier, N. 2010, *BMC Pharmacol.*, 10, 6
- [155] Stacey, A. et al. 2019, *Adv. Mater. Interfaces*, 6, 1801449
- [156] Steiner, M., Neumann, P., Beck, J., Jelezko, F., & Wrachtrup, J. 2010, *Phys. Rev. B*, 81, 35205
- [157] Steinert, S. et al. 2013, *Nat. Commun.*, 4, 1607
- [158] Takahashi, S., Hanson, R., van Tol, J., Sherwin, M. S., & Awschalom, D. D. 2008, *Phys. Rev. Lett.*, 101, 047601
- [159] Tamarat, P. et al. 2008, *New Jour. Phys.*, 10, 45004
- [160] Taminiau, T. H., Wagenaar, J. J. T., van der Sar, T., Jelezko, F., Dobrovitski, V. V., & Hanson, R. 2012, *Phys. Rev. Lett.*, 109, 137602
- [161] Taylor, J. M. et al. 2008, *Nat. Phys.*, 4, 810

- [162] Terblanche, C. J., Reynhardt, E. C., & van Wyk, J. A. 2001, *Solid State Nucl. Magn. Reson.*, 20, 1
- [163] Tetienne, J.-P. et al. 2013, *Phys. Rev. B*, 87, 235436
- [164] Tetienne, J. P., Lombard, A., Simpson, D. A., Ritchie, C., Lu, J., Mulvaney, P., & Hollenberg, L. C. L. 2016, *Nano Lett.*, 16, 326
- [165] Thiering, G. & Gali, A. 2018, *Phys. Rev. B*, 98, 85207
- [166] Trusheim, M. E. et al. 2014, *Nano Letters*, 14, 32
- [167] van Oort, E., Manson, N. B., & Glasbeek, M. 1988, *J. Phys. Condens. Matter*, 21, 4385
- [168] Vandersypen, L. M. K. & Chuang, I. L. 2005, *Rev. Mod. Phys.*, 76, 1037
- [169] Vijay, R., Slichter, D. H., & Siddiqi, I. 2011, *Phys. Rev. Lett.*, 106, 110502
- [170] Waldherr, G. et al. 2012, *Nat. Nanotechnol.*, 7, 105
- [171] Waldherr, G., Beck, J., Steiner, M., Neumann, P., Gali, A., Frauenheim, T., Jelezko, F., & Wrachtrup, J. 2011, *Phys. Rev. Lett.*, 106, 157601
- [172] Waldherr, G., Neumann, P., Huelga, S. F., Jelezko, F., & Wrachtrup, J. 2011, *Phys. Rev. Lett.*, 107, 090401
- [173] Waldherr, G. et al. 2014, *Nature*, 506, 204
- [174] Wehner, S., Elkouss, D., & Hanson, R. 2018, *Science*, 362, eaam9288
- [175] Wort, C. J. & Balmer, R. S. 2008, *Mater. Today*, 11, 22
- [176] Zaitsev, A. M. 2001, *Optical Properties of Diamond* (Springer)
- [177] Zvyagin, A. V. & Manson, N. B. 2012, in *Ultrananocrystalline Diamond*, ed. O. A. Shenderova & D. Gruen (Oxford: William Andrew Publishing), 327–354